

October 2022

Accelerating Multiparametric MRI for Adaptive Radiotherapy

Shraddha Pandey
University of South Florida

Follow this and additional works at: <https://digitalcommons.usf.edu/etd>



Part of the [Electrical and Computer Engineering Commons](#), [Mathematics Commons](#), and the [Oncology Commons](#)

Scholar Commons Citation

Pandey, Shraddha, "Accelerating Multiparametric MRI for Adaptive Radiotherapy" (2022). *USF Tampa Graduate Theses and Dissertations*.
<https://digitalcommons.usf.edu/etd/9802>

This Dissertation is brought to you for free and open access by the USF Graduate Theses and Dissertations at Digital Commons @ University of South Florida. It has been accepted for inclusion in USF Tampa Graduate Theses and Dissertations by an authorized administrator of Digital Commons @ University of South Florida. For more information, please contact digitalcommons@usf.edu.

Accelerating Multiparametric MRI for Adaptive Radiotherapy

by

Shraddha Pandey

A dissertation submitted in partial fulfillment
of the requirements for the degree of
Doctor of Philosophy
Department of Electrical Engineering
College of Engineering
University of South Florida

Co-Major Professor: Wilfrido A. Moreno, Ph.D.
Co-Major Professor: Natarajan Raghunand, Ph.D.
Ashwin Parthasarathy, Ph.D.
Andres Tejada, Ph.D.
Christos Ferekides, Ph.D.
Eduardo Moros, Ph.D.

Date of Approval:
October 24, 2022

Keywords: Joint Total Variation, Intratumoral Habitats, Tissue Phenotyping, Image
Reconstruction, Radiation Dose Maps

Copyright © 2022, Shraddha Pandey

Dedication

To the memory of my mother

Acknowledgments

I am deeply thankful to my advisors Dr. Wilfrido A. Moreno and Dr. Natarajan Raghunand, for their supervision, ideas and motivation that kept me on track. I am grateful for their guidance and appreciate that they opened so many doors for me.

I want to thank Dr. Arthur David Snider for helping me derive those long mathematical equations and providing the intuition into them. I am very grateful for all your input and insights into those crucial details which helped me publish my first article.

I am grateful to Dr. Eduardo Moros, Dr. Kamran Ahmed, and Dr. Ali Bilgin from Arizona State University for their input and support during this collaboration. I would also like to recognize Dr. Olya Stringfield's and Dr. Mahmoud's efforts for processing the data and the enormous help I received from Dr. Gary Martinez. He introduced me to the concepts of MRI during my research's early stages.

I am very thankful to the Electrical Engineering Department, USF, and the Moffitt Cancer Center for providing the financial support and facilities that enabled me to complete the graduate program. I am very grateful for the effort spent by my dissertation committee members to help me reach my goal.

I want to thank Dr. Ravi Sankar, Dr. Prashanth Chetlur Adithya, and Dr. Sai Bhardwaj for guiding and helping me during the very early stages of my career; many thanks to my colleagues Dr. Harshan Ravi and Dr. Andres Lorza at Moffitt Cancer Center for those insightful conversations.

I am grateful to my parents, family and friends for their unwavering support and motivation. Last but not the least, I wish to thank my husband, Rahul, for his patience and moral support.

Table of Contents

List of Tables	iv
List of Figures	v
Abstract	vii
Chapter 1: Introduction	1
1.1 Image Guided Radiotherapy	1
1.2 MR Guided Radiotherapy	3
1.3 Challenges of MR Guided Radiotherapy	4
1.4 Contributions	6
1.5 Dissertation Organization	7
1.5.1 Chapter 2-Brief Introduction to the Concepts of MRI	7
1.5.2 Chapter 3-Accelerating the Reconstruction of mpMRI	8
1.5.3 Chapter 4-Radiation Therapy Treatment Planning	8
1.5.4 Chapter 5-Image to Image Translation	8
1.5.5 Chapter 6-Prediction of Radiation Dose Maps from mpMRI	8
1.5.6 Chapter 7-Conclusion and Future Work	9
Chapter 2: MRI	10
2.1 Introduction to MRI	10
2.2 MRI Reconstruction	13
2.3 Accelerating the MRI Reconstruction	15
2.4 Fat and Water Estimation	18
2.5 Multispectral Analysis of MRI	19
Chapter 3: Framework to Identify the Intratumoral Habitats from mpMRI	22
3.1 Materials and Methods	22
3.1.1 Mice and Cell Culture	22
3.1.2 Acquisition of Magnetic Resonance Imaging	22
3.2 Joint Reconstruction Framework for T1w Images and T1 Maps	23
3.2.1 Proposed Method	23
3.2.2 Optimization Framework	26
3.2.3 Extension Framework for T2w/T2*w Images and their Maps	29
3.3 Validation Framework	30
3.3.1 T1w and T2w MRI	30
3.3.2 T1 and T2 Maps	31
3.3.3 T2*w MRI	32

3.3.4	Comparison with FCSA-MT Algorithm	32
3.4	Results	33
3.5	Discussion	39
Chapter 4:	Radiation Therapy	42
4.1	Basics of Radiotherapy Treatment	42
4.2	Knowledge Based Methods of Treatment Planning	43
4.3	Neural Network-Based Radiotherapy Treatment Planning	44
Chapter 5:	Generative Adversarial Networks	46
5.1	Introduction to Deep Neural Networks	46
5.2	Basics of GAN	47
5.3	Pix2Pix GAN	48
Chapter 6:	Prediction of Optimal Radiation Therapy Dose Maps from the mpMRI	50
6.1	Relation between Radiation Dose Maps and mpMRI	50
6.2	Data Preprocessing	51
6.3	Preliminary Data Analysis	55
6.4	Model Architecture	56
6.4.1	Generator	56
6.4.2	Discriminator	58
6.5	Training and Implementation	58
6.6	Validation Framework	60
6.6.1	Forward Model	60
6.6.2	Inverse Model	60
6.7	Results	61
6.8	Discussions	67
Chapter 7:	Conclusions and Future Work	73
7.1	Conclusions	73
7.2	Future Work	74
References	76
Appendix A:	Copyright Permission to Use Published Content in Chapter 3	95
Appendix B:	Copyright Permission to Use Published Content in Chapter 6	96
Appendix C:	Copyright Permission to Use DWI Figure in Chapter 2	97
Appendix D:	Copyright Permission to Use Fatwater Figure in Chapter 2	98
Appendix E:	IRB Approval	99
Appendix F:	IACUC Approval	100
Appendix G:	Generator Model	101

Appendix H: Discriminator Model 104
About the Author End Page

List of Tables

Table 3.1	Quantitative Validation of Joint Reconstruction Algorithm	32
Table 3.2	Comparison of mpMRI Reconstruction Time	41
Table 6.1	Mean and Standard Deviation Estimated from Training Data	53
Table 6.2	Identified Global Low and High Threshold from Training Data	55

List of Figures

Figure 1.1	Block Diagram of Online Adaptive Radiotherapy Process for MRgRT	3
Figure 2.1	Block Diagram of MRI Acquisition and Reconstruction	11
Figure 2.2	Diffusion Weighted Imaging	14
Figure 2.3	Types of MRI Sequences	15
Figure 2.4	Water and Fat Peak Separated by ~ 3.5 ppm	20
Figure 2.5	Multispectral Analysis of mpMRI	21
Figure 3.1	Block Diagram of Joint Reconstruction Algorithm	24
Figure 3.2	Reconstruction Results for T1w Images	34
Figure 3.3	Reconstruction Results for T2w Images	35
Figure 3.4	Results of T1 and T2 Parameter Maps and Tissue Type Maps	37
Figure 3.5	Results of PDFF, PDwF and Relaxation Rates of Water and Fat	38
Figure 3.6	Comparison of Proposed Algorithm with FCSA-MT and GT	39
Figure 6.1	Histogram of Post-RT Acquisition Time Gap vs. Number of Subjects	51
Figure 6.2	Quantitative Validation of Forward Model	52
Figure 6.3	BCMB Data Preprocessing	53
Figure 6.4	Example Slice from BCMB Dataset	54
Figure 6.5	Scaling Factor Used for Generating the Training Images	55
Figure 6.6	Delta Changes of mpMRI vs. RT Dose Plots	56
Figure 6.7	Tumor Volume Change for Recurrent and Responding Lesions	57
Figure 6.8	Proposed Forward Model	57
Figure 6.9	Proposed Inverse Model	58

Figure 6.10 Iteration vs. Correlation Values for Training Data	59
Figure 6.11 Predicted Histograms within the Brain Mask for Training Subjects . .	62
Figure 6.12 Predicted Histograms within the Brain Mask for Test Subjects . . .	62
Figure 6.13 Results of the Forward Model	63
Figure 6.14 Predicted Histograms within the GTV for Test Subjects	63
Figure 6.15 Predicted Histograms within the GTV for Training Subjects	64
Figure 6.16 Tissue Type Maps Computed from Forward Model	65
Figure 6.17 Quantitative Validation of Forward Model for Six Test Subjects . . .	66
Figure 6.18 Quantitative Validation of Forward Model for 1-6 Training Subjects .	67
Figure 6.19 Quantitative Validation of Forward Model for 7-12 Training Subjects	68
Figure 6.20 Quantitative Validation of Forward Model for 13-18 Training Subjects	69
Figure 6.21 Simulated Predictions of Forward Model	70
Figure 6.22 Simulated Predicted Histograms from the Forward Model	70
Figure 6.23 Simulated Predictions of the Inverse Model	71
Figure 6.24 Simulated Predicted Histograms from the Inverse Model	72

Abstract

MR guided Radiotherapy (MRgRT) marks an important paradigm shift in the field of radiotherapy. Superior tissue contrast of MRI offers better visualization of the abnormal lesions, as a result precise radiation dose delivery is possible. In case of online treatment planning, MRgRT offers better control of intratumoral motion and quick adaptation to changes in the gross tumor volume. Nonetheless, the MRgRT process flow does suffer from some challenges that limit its clinical usability. The primary aspects of MRgRT workflow are MRI acquisition, tumor delineation, dose map prediction and administering treatment. It is estimated that the acquisition of MRI takes around 50% of the entire process. Further, delineating the tumor volumes and generating the dose map plans are labor-intensive and time-consuming yet necessary to prevent radio necrosis and associated toxicity. To this end, this dissertation focuses on the two important aspects of MRgRT. First, acceleration of reconstruction of multiparametric MRI (mpMRI). Second, prediction of precise dose maps from the pre-radiation therapy mpMRI sequences without the need of manual contouring.

A joint reconstruction algorithm to accelerate the reconstruction of a series of complex T1w images, T1 and proton density maps simultaneously from the undersampled k-space data is presented. The ambiguity introduced by undersampling is resolved using model-based constraints, and structural information from a reference fully sampled image as the joint total variation prior. The algorithm is extended with minor modifications to accelerate the reconstruction of complex T2w, T2*w images and their parameter maps. Validation of the reconstructed images and parameter maps was carried out by computing tissue-type maps, as well as the maps of the Proton Density Fat Fraction (PDFF), Proton Density Water Fraction (PDwF), fat relaxation rate (R_{2f}^*) and water relaxation rate (R_{2w}^*) from the reconstructed data by comparing them with Ground Truth (GT) equivalents. It is demonstrated that using

only 18% k-space data, it is possible to identify the tissue type maps like fluid, muscle, tumor and adipose with the same fidelity as that obtained using GT data. The mean T1 and T2 values in each tissue type were computed using only 18% k-space data, which were within 8%-10% of the GT values from fully sampled data. The PDFF and PDwF maps computed using 27% k-space data were within 3%-15% of GT values and showed good agreement with the expected values for the four tissue types. The next task focuses on directly predicting the optimum Radiation Therapy (RT) dose maps from the pre-RT mpMRI. It is now well established that the tumor volume comprises several different microenvironments. Hence, predicting a voxel-wise dose map from the pre-RT and prescribed/desirable post-RT mpMRI will yield better control of radionecrosis-related toxicity. Furthermore, it is also important for the radiation oncologist to simulate voxel-wise radiologic outcomes of specific RT dose map prescriptions on post-RT mpMRI. To accomplish these two tasks, end-to-end deep neural networks are trained. The forward model is used to predict post-RT changes on mpMRI using pre-RT mpMRI when administered with the radiation dose map. A variant of the pix2pix GAN network is trained to predict post-RT ADC maps, T1wCE, T2w, T1w, FLAIR MRI from pre-RT mpMRI and the radiation dose maps. The results of the forward model are validated by identifying the tissue type maps like blood volume, gray matter, white matter, edema, non-enhancing tumor, contrast enhancing tumor, hemorrhage, fluid and comparing them with the GT maps. Further, the quantitative validation is carried out by comparing the percentage of volumes of these tissue type maps from pre-RT, post-RT and predicted post-RT mpMRI. The results of the forward model are also tested with the simulated dose maps and comparing the changes on the predicted post-RT ADC maps that are mechanistically relatable to voxel-level tumor response to therapies. Next, a variant of pix2pix GAN is trained to predict the radiation dose maps from the pre-RT ADC maps and the prescribed post-RT ADC maps. This is called as the inverse model. It is determined from the simulated results that to achieve higher ADC values, higher RT dose maps are required.

In summary, the results of the feasibility study showed that it is possible to identify various tissue type habitats from the reconstructed mpMRI scans using only 18% k-space data. This dissertation also highlights that it is possible to alleviate the manual aspects of Radiation Therapy planning by using pre-RT and post-RT mpMRIs to predict the Radiation dose maps.

Chapter 1: Introduction

1.1 Image Guided Radiotherapy

Image-Guided Radiotherapy (IGRT) is a process of using noninvasive imaging modalities to guide the delivery of radiation therapy. High-quality imaging scans help guide the accurate and focused radiation on the tumor region with minimal damage to the healthy tissue [17]. The primary aim is to optimize the Radiotherapy (RT) plan to target potentially radiation-insensitive lesions while avoiding radionecrosis and associated toxicity [71]. The standard IGRT setup uses Computed Tomography (CT) imaging for treatment planning and dose delivery. The radiation oncologist typically uses information from other imaging modalities such as MRI, PET, etc. These imaging modalities augment the information from previously acquired diagnostic quality CT scans when customizing the RT plan for a given patient. In the treatment planning phase, procedures such as marker placement and immobilization mask, depending on the requirement, are performed to identify the treatment site [17]. The next step is a delineation of Gross Target Volumes (GTV), Clinical Target Volumes (CTV), Planning Target Volumes (PTV) and Organs at Risk (OAR). GTV is the primary tumor volume that needs to be treated. The microscopic extensions of the tumor not visible with imaging in addition to the GTV is known as CTV. PTV is addition of CTV, safety margins for organs, patient movements, dose homogeneity within the CTV and position-related uncertainties [114]. These prescriptions act as an optimization constraint to generate optimal fluence maps that are used to deliver radiation therapies such as Intensity Modulated Radiation Therapy (IMRT), Volumetric Modulated Arc Therapy (VMAT), Stereotactic Radiosurgery (SRS), etc., as a single dose or in multiple fractions. The treatment response

is then evaluated using the follow-up scans. Figure 1.1. shows a basic workflow of Image Guided Radiotherapy.

While this workflow is successful, it suffers from limitations due to poor tissue contrast of CT, the registration error between the planning CT and additional imaging modalities [92]. The misregistration error introduced during the therapy planning stage is often propagated to the treatment stage. This may lead to higher Planning Tumor Volume margins and dose spilling for organs at risk leading to increased risk of dose toxicity [34]. Radio opaque markers known as fiducials are often used to identify the accurate tumor positions and limit the PTV margins. However, these markers need to be implanted using surgery before therapy, which is often stressful for patients [18]. Furthermore, with the advancements in IMRT and VMAT, the requirements for the delineation of target volume have become more stringent [103].

Radiation treatment dose map planning is a critical step for effective control of cancer. However, dose map planning is time-consuming and relies heavily on the experience and expertise of the treatment planner. Several studies have been carried out to automate the process of dose map planning such as Knowledge-Based Planning (KBP) [72][91]. However, these methods required many model parameters. Additionally, the generated dose map may be optimum but not clinically acceptable [84]. The present state-of-the-art IGRT prescribes homogeneous radiation doses without considering the voxel level information. However, it is now well established that the tumors are non-homogeneous and comprise several heterogeneous tumor microenvironments or habitats [55][16]. Tumor cells within distinct habitats may be differentially sensitive to RT, with some habitats requiring dose escalation while other habitats may provide scope for dose reduction with consequent decrease in risk of toxicity, radionecrosis to nearby normal tissues. In the next section, MR-Guided Radiotherapy (MRgRT) is discussed, which offers an improvement over the standard state-of-the-art IGRT system.

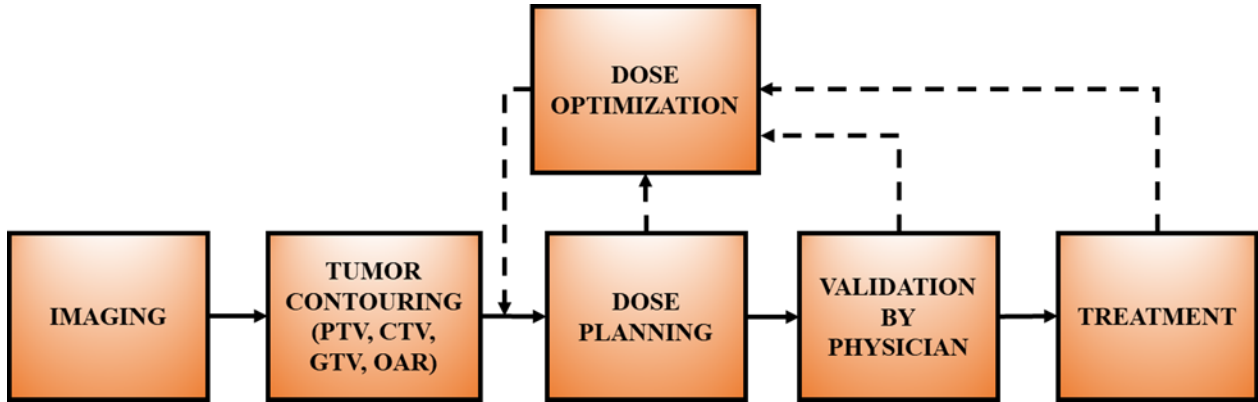


Figure 1.1: Block Diagram of Online Adaptive Radiotherapy Process for MRgRT.

1.2 MR Guided Radiotherapy

The integration of MR imaging and linear accelerators (LINAC) has recently led to MR-guided radiotherapy using MR-LINACs, which has become an important alternative to standard Image-guided radiotherapy, that uses CT as the primary imaging modality. Compared to CT, variants of MRI can be acquired with superior soft-tissue contrast. Moreover, combination of information from multiparametric MRI can provide information on intratumoral habitats [98]. MRgRT has the advantage of planning and treatment positions being performed on the same setup. As a result, registration errors and hardware-dependent image distortion might be easy to handle [129]. Furthermore, target volume delineation and real-time treatment RT adaption are possible with MRgRT. Real-time tumor response assessment and RT adaptation are very important in case of daily targeting and planning optimization where gross tumor volume evolves quickly. One of the examples is prostate cancer, where the tumors between and during the treatments change very quickly [47]. In case of the brain, when administered with Hypofractionated Stereotactic Radiosurgery, the resection cavity may change in response to the radiation therapy, within 3 to 5 visits [15][48][24]. It is determined that real-time online plan adaptation, better visualization of target position, and constrained smaller PTV using MRI may prolong the reoccurrence of tumors and lower the toxicity of thoracic lung cancer [24].

Multiparametric MRI offers the potential for discriminating between radio-sensitive and radio-resistant tumors. This feature may be used to optimize the radiation plan by dose-escalating for lesions predicted to be radio-resistant or more likely to recur after treatment [65]. In addition to anatomic or structural information, multiparametric MRI (mpMRI) sequences also provide functional information containing insights into biological processes and tumor microenvironments. Functional MR imaging biomarkers such as Diffusion Weighted Imaging (DWI) are useful for personalized biologically individualized voxel-level RT prognosis [111]. Changes in the micro-vascular properties in the presence of angiogenesis obtained from Diffusion Contrast Enhanced (DCE) MRI are used as tumor biomarkers [14]. mpMRI, particularly Apparent Diffusion Coefficient (ADC) maps, provide information about tumor cell regrowth, inflammation, fibrosis and fat infiltration. For example, solid tumors with dense cellularity have mean ADC values around $10^{-3} mm^2/s$ that shifts to higher values in therapeutically responsive tumor regions following cytotoxic therapy. This occurs due to a decrease in the intracellular space, restricted water mobility from cell death and the consequent increase in the extracellular space, greater water mobility, [36]. The biological insights obtained using the real-time mpMRI obtained from MRgRT may be useful in improved tumor localization and hence optimized RT dose maps. In conventional radiotherapy intra-treatment, tumor motion correction is usually obtained by higher PTV margins or implants. However, with adaptive MRI-guided radiotherapy, stringent irradiation of the tumor region is possible [59]. In MR- only treatment planning machines, the mpMRI is also helpful in identifying the tissue types used to generate synthetic CT and in deriving the electron density values necessary for radiation dose calculation [18].

1.3 Challenges of MR Guided Radiotherapy

There are certain challenges that must be overcome so that MRgRT LINAC can be used for the benefit of patients. The entire pipeline for real-time MRgRT can be divided into MRI acquisition, tumor segmentation, accurate estimation of radiation dose maps and

administering treatment. It is important to determine the GTV, CTV, PTV and OAR changes in real time to optimize the radiation maps and avoid damage to healthy tissues. As noted by Thorwarth et al. in [111], MRI acquisition takes up around 50% of the total time of this pipeline. Moreover, geometric accuracy for precise delivery of RT is an important consideration for real-time MRI acquisition. Also, longer scans are vulnerable to motion-related artifacts when compared to shorter scans. To counter this, real-time MR-guided RT acquires the k-space data at higher readout bandwidths but at the cost of lower SNR [18][117]. Moreover, when compared to diagnostic MRI scanners and the planning MRI or MRI simulator, at present the MR LINAC 1.5 T high field (Elekta Unity, Elekta Instrument AB, Stockholm, Sweden) and 0.35 T (MRIdian Linac, ViewRay, Oakwood, CA, USA) can acquire only standardized limited built-in sequences [129]. While the 1.5 T MR LINAC can acquire 3D-TSE T2w and T1w images, the acquisition of DWI is currently very challenging [63][64]. The acquired DWI has a lower Signal-to-Noise Ratio (SNR) and highest possible b-value measurement is 500 only due to the suboptimal hardware [129]. Specific Absorption Rate (SAR) leading to tissue heating is one of the limiting factors for high field MRgRT systems and also for some acquisition protocols [111]. Real-time 3D imaging effectively corrects the intra-fraction motion for MR-only radiotherapy, however the acquisition and reconstruction latency for 3D imaging may degrade the dose accuracy of radiotherapy [107].

MRgRT also requires accurate real-time identification of GTV, PTV, CTV and OAR regions. Currently, deep learning methods have been very successful in the segmentation of MRI. However, owing to the variability and diversity among different tumor types, the generalizability of these algorithms remain challenging. Deep Learning methods have also been tried for real-time estimation of dose maps using the anatomical structure contours derived from MRI. However, the stringent requirements for real-time dose map prediction to ensure robustness, accuracy and precision have limited their use mostly for research purposes while its clinical translation remains challenging [111].

1.4 Contributions

Information from multiple sequences is ideally required to properly define and visualize intratumoral habitats, but acquisition of such a rich MRI dataset at adequate spatial resolution is currently too time consuming for routine deployment in the clinical setting. In this work, two important aspects of the MRgRT pipeline are addressed: Accelerate reconstruction of mpMRI and predict the dose map from pre-RT mpMRI.

1. Developed an algorithm to accelerate the reconstruction of mpMRI from undersampled k-space data and used these mpMRI sequences to identify the intra-tumoral habitats.
 - (a) Developed a joint reconstruction algorithm to reconstruct a series of T1w images, the corresponding proton density and T1 maps.
 - (b) Developed a framework to identify tissue type maps like fluid, adipose, muscle and tumor.
 - (c) Repeated the joint reconstruction algorithm with minor modification to reconstruct a series of T2w, T2*w images, the corresponding proton density, T2 and T2* maps.
 - (d) Validated the reconstruction of T2*w images by implementing the fat and water estimation framework to identify the proton density fat fraction, proton density water fraction, field inhomogeneity, Ψ , relaxation rates of water R_{2w}^* and fat R_{2f}^* .
 - (e) Validated and compared the results of the proposed joint reconstruction framework with the FCSA-MT Algorithm [51].
2. Developed an automated framework to enable optimal Radiation therapy dose planning from pre-RT mpMRI.
 - (a) Performed data analysis on the mpMRI scans of Breast Cancer Metastases to Brain (BCMB) patients to identify the changes between pre-RT and post-RT mpMRI.

- (b) Performed data analysis to identify the key differences between the responding and recurring lesions in BCMB patients.
- (c) Developed a forward model to predict the post-RT changes on mpMRI using the pre-RT mpMRI and the radiation dose maps.
- (d) Developed an inverse model to predict the optimal RT dose map from pre-RT ADC and prescribed/desired post-RT ADC.
- (e) Validated the results of the forward model by subjecting the predicted post-RT mpMRI to tissue type segmentation framework and comparing them to the ground truth maps.

The results in this dissertation have been published as peer-reviewed article [95] and presented at several national and international conferences [67][94][93].

1.5 Dissertation Organization

The literature review and the research methodology used is described in the following chapters.

1.5.1 Chapter 2-Brief Introduction to the Concepts of MRI

This chapter introduces the concepts related to MRI necessary to understand the first task, i.e., accelerating the reconstruction of mpMRI from under sampled k-space. Basics of MRI acquisition and comparison of different MRI sequences are described along with the concepts of MRI reconstruction. A literature review on existing techniques to accelerate the reconstruction of MRI are included in this chapter in addition to the introduction to fat and water estimation methods. Finally, the multispectral analysis of MRI to identify the tumor microenvironment is also included.

1.5.2 Chapter 3-Accelerating the Reconstruction of mpMRI

This chapter provides a detailed overview of the implemented joint reconstruction framework. A brief description of how the data was collected and the underlying process is provided. Next, a detailed derivation of the mathematical objective function to reconstruct a series of T1w images and the corresponding T1 maps is presented, followed by a comprehensive description of the optimization framework used to solve the objective function. An extension of the joint reconstruction framework for T2w, T2*w images and the parameter maps is also highlighted. In addition, the validation framework, the qualitative and quantitative results are summarized. Finally, the chapter is concluded by presenting the summary of the findings, possible extensions to the framework and discussions.

1.5.3 Chapter 4-Radiation Therapy Treatment Planning

A detailed description of the radiation therapy process flow is provided in this chapter and the challenges of the radiation therapy process also discussed. Next, automated methods of radiation dose map planning and a brief literature review highlighting the strengths and weaknesses of the methods are provided. Finally, a comprehensive review of the deep learning-based framework to automate dose map planning is presented in this chapter.

1.5.4 Chapter 5-Image to Image Translation

This chapter briefly introduces neural networks. A mathematical perspective on the Generative Adversarial Networks (GAN) is presented. The extension of GAN, i.e., the pix2pix framework for image-to-image translation is also described.

1.5.5 Chapter 6-Prediction of Radiation Dose Maps from mpMRI

This chapter provides a detailed overview of the implemented deep learning-based framework to predict images. A brief description of data acquisition, preprocessing and analysis is presented along with a detailed description of the pix2pix GAN framework to predict post-

RT mpMRI images from the radiation dose maps and pre-RT mpMRI. This is followed by a description of the data pre-processing and deep learning framework for the inverse model, i.e., to predict the radiation dose maps from pre-RT ADC and prescribed post-RT ADC. Finally, the chapter is concluded by presenting the summary of findings and discussions.

1.5.6 Chapter 7-Conclusion and Future Work

A summary of the findings of this research is provided in this chapter. Then, directions for future research with respect to improving the end-to-end framework for MRgRT has been provided in this chapter. In particular, the extension of joint reconstruction framework to accelerate the reconstruction of ADC maps is discussed. In addition, future directions for improving the algorithm to predict radiotherapy dose maps is also discussed.

Chapter 2: MRI

2.1 Introduction to MRI

MRI is a noninvasive imaging technique that produces high-resolution images with excellent soft tissue contrast of the anatomical organs. MRI signal is obtained by manipulating the spin angular momentum of the hydrogen nucleus, i.e., a proton, which comprises a large percentage of the human body [74]. In the absence of a magnetic field, the magnetic moments of individual hydrogen nuclei in the tissue, mostly on water molecules precess randomly with a net zero magnetic moment. Imposition of a strong external magnetic field generates a net magnetic moment aligned with the field, which is manipulated using Radio Frequency (RF) pulses and directional magnetic fields called gradients, to produce a signal. The MRI scanner comprises primary magnets, gradient magnets, radiofrequency coils, RF detectors and the computing device.

In the presence of the primary magnetic field, B_0 , the hydrogen protons align themselves to the longitudinal magnetic field. The three gradient coils localize the body part that needs to be scanned in x, y, and z-direction. The RF coil and detectors transmit the excitation pulse and receive the signal from the excited spins. RF coils are designed for specific body regions. Furthermore, multiple RF coils may also be used to improve the SNR of the acquisition. When subjected to the gradient field, the hydrogen atoms align themselves in the direction of the applied gradient field, resulting in a high longitudinal signal called spin-lattice relaxation as seen in Figure 2.1. When an RF excitation pulse is applied to the precessing hydrogen atoms, they are knocked off and result in a high signal in the transverse direction. As the excitation pulse is removed, the transverse signal decays exponentially, called as transverse relaxation, spin-spin relaxation process. Simultaneously, the longitudinal signal grows back

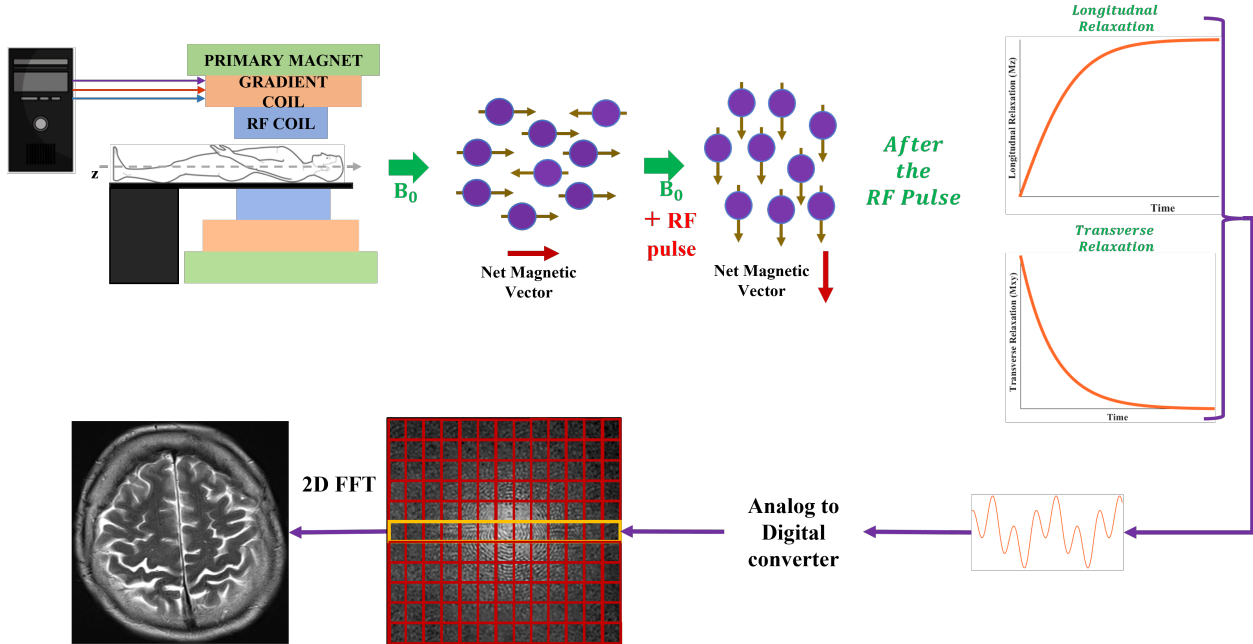


Figure 2.1: Block Diagram of MRI Acquisition and Reconstruction.

to the maximum signal and is termed as the longitudinal relaxation process. The antenna receives the RF signal emitted during this process and the analog signal is digitized using the A/D conversion. The digitized frequency encoded information is recorded from left to right as one of the lines of k-space data. The excitation process is repeated m times with different gradient strengths. As a result, each k-space line has a unique phase along this direction and is called phase encoding direction. The frequency encoding and the phase-encoded information thus form the $m \times n$ k-space data, which is then processed to generate the image of size $m \times n$ [74].

The transverse relaxation process is defined by the model Equation $A \cdot e^{-T_E/T_2}$. Here, T_E is the echo time, T_2 is the time constant of the transverse relaxation rate and A is the proton density. The images resulting due to transverse relaxation process is called as T2 weighted, T2w, image and the corresponding relaxation maps are called as T2 maps. The actual relaxation rate T_2 is much faster than the effective relaxation rate T_2^* in the presence of the field inhomogeneity and susceptibility. The relation between the actual and effective

relaxation rate is given by Equation 2.1.

$$\frac{1}{T_2^*} = \frac{1}{T_2} + \frac{1}{T_2'} \quad (2.1)$$

Here, $\frac{1}{T_2} = \gamma \Delta B_i$ is the relaxation rate resulting due to field inhomogeneity ΔB_i in each voxel, γ is a gyromagnetic ratio. Similarly, the longitudinal relaxation process is defined by the model equation $A \cdot (1 - e^{-T_R/T_1})$ where, T_R is the repetition time and T_1 is the time constant of the longitudinal relaxation rate. The resulting image is the T1 weighted, T1w, image and the corresponding relaxation maps are called as T1 maps. The T1 and T2 relaxation rates depend on the tissue composition. For example, T1 relaxation rate is longer for water-based tissue compared to the fat.

DWI is a type of MRI which measures the Brownian motion of the water molecules within the tissue to be scanned. The molecular movement of the water molecule is a function of the tissue type. For example, in case of a tumor, the diffusion of the water molecule is highly impeded compared to that in the Cerebrospinal Fluid (CSF). The unrestricted movement of the molecules in the homogenous medium is called isotropic diffusion. However, in the case of biological tissue like axons, the movement of the water molecule will be constrained in the axial direction. This is called anisotropic diffusion. DWI is acquired using two diffusion-sensitizing gradient fields. When the body part that needs to be scanned is subjected to these diffusion-sensitizing gradients as shown in Figure 2.2, the water molecules in motion experience less refocus than the stationary water molecules. As a result, the signal from highly diffused water molecules is less strong than that from the stationary case. If the diffusion gradient is applied in x-direction the acquired DWI image S_x can be defined as $S_x = S_0 e^{-bD_{xx}}$. Here, b defines b-value which is the factor denoting the strength of the diffusion sensitizing gradient fields applied in x direction. S_0 is the DWI signal obtained for $b = 0$. Correspondingly, the DWI images acquired when the diffusion gradient is applied in y and z direction are defined as $S_y = S_0 e^{-bD_{yy}}$ and $S_z = S_0 e^{-bD_{zz}}$ respectively. The

DWI in multiple different directions are combined to generate a trace DW image defined as $S_{DWI} = (S_x S_y S_z)^{\frac{1}{3}} = S_0 e^{-bADC}$; where $ADC = \frac{(D_{xx} + D_{yy} + D_{zz})}{3}$ is the apparent diffusion coefficient defining the diffusion constant. The echo times are longer for acquiring DWI images. As a result, the areas of longer T2 values sometimes suffer from the ‘‘T2 shine-through effect’’. ADC maps are used to differentiate artifacts from true pathology and are very important quantitative MRI type. In the case of lesions, strokes and abscesses where there is restricted diffusion, the ADC values are lower and conversely, where there is unimpeded diffusion, CSF, ADCs will be bright as highlighted in Figure 2.3 [4]. DWI images are the combinations of x, y and z directions and when acquired in anisotropic directions are called diffusion tensors. The corresponding images are Diffusion Tensor Images (DTI) that are often used in the diagnosis of white matter pathologic features such as ischemia, edema and axonal damage [2].

In addition to T1w, T2w and DWI there are other MRI sequences like Fluid-Attenuated Inversion Recovery (FLAIR) are used to suppress the signals from fluid. In case of DCE map the vascular information is augmented [58]. It can be deduced from the literature that while each MRI sequence highlights specific tissue information, the combined analysis of the acquired sequences can provide a wealth of information. Figure 2.3 shows an example slice of the MRI sequences like T1w, T2w, FLAIR and ADC which have similar structural details but different contrast.

2.2 MRI Reconstruction

In the acquired k-space data, each line of the k-space contains time-domain data from the entire slice. The spatial information of a given voxel in each slice is encoded as a function of frequency and phase. In order to decode the image from the k-space data, a 2D Fourier Transform is carried out. The generation of the MR Image ‘u’ from the k-space data ‘k’ can be defined by Equation 2.2.

$$u = E^{-1}(k) \tag{2.2}$$

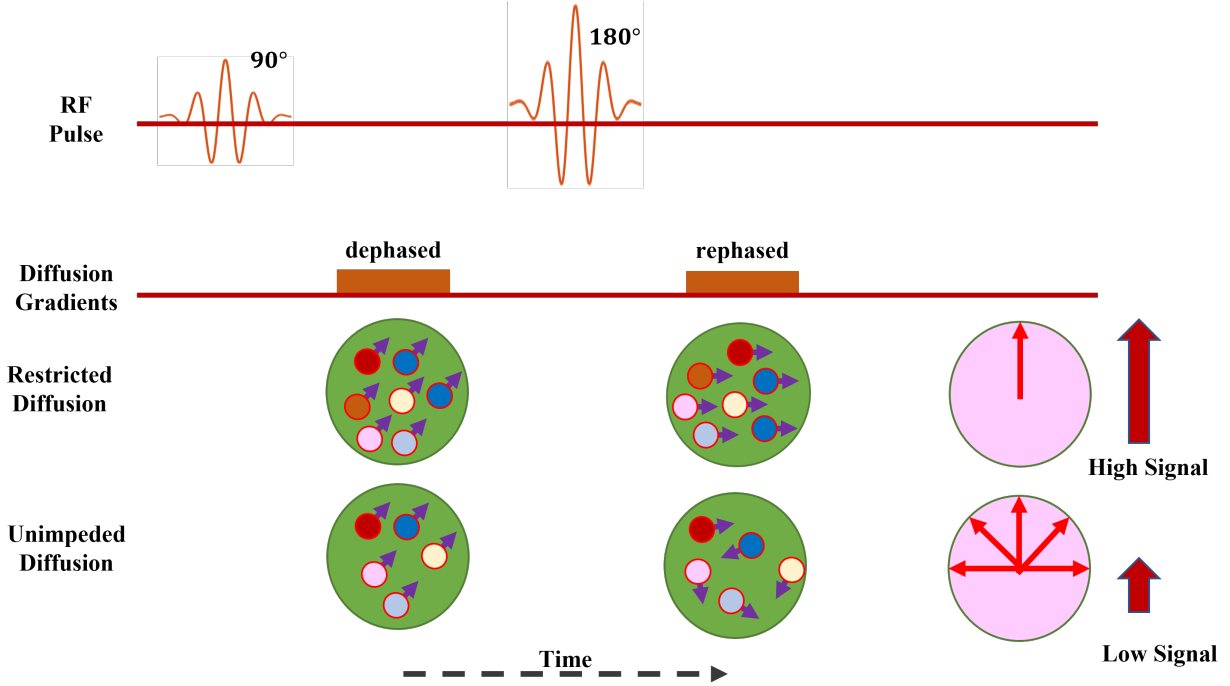


Figure 2.2: Diffusion Weighted Imaging (Image Adapted from [68]. Permission is included in Appendix C.).

Here, E is the encoding matrix. If the acquired k-space data is twice the maximum frequency, then the solution is immediate and the MR Image ‘ u ’ can be obtained by 2D inverse Fast Fourier Transform of the k-space data as shown in Equation 2.3.

$$u = IFFT(k) \quad (2.3)$$

Acceleration of the acquisition of MR Images is achieved by acquiring less k-space data, i.e., below the Nyquist rate. Some of the methods wherein less data is acquired are non-cartesian data acquisition, parallel imaging, compressed sensing and others. The simplest solution to acquiring less data is skipping some lines from phase encoding direction. Less k-space data reduces the acquisition time but the reconstruction problem becomes ill-posed. As a result, solution using direct inversion is not possible. Iterative reconstruction methods like conjugate gradient [104], non-linear conjugate gradient [8], alternating direction method

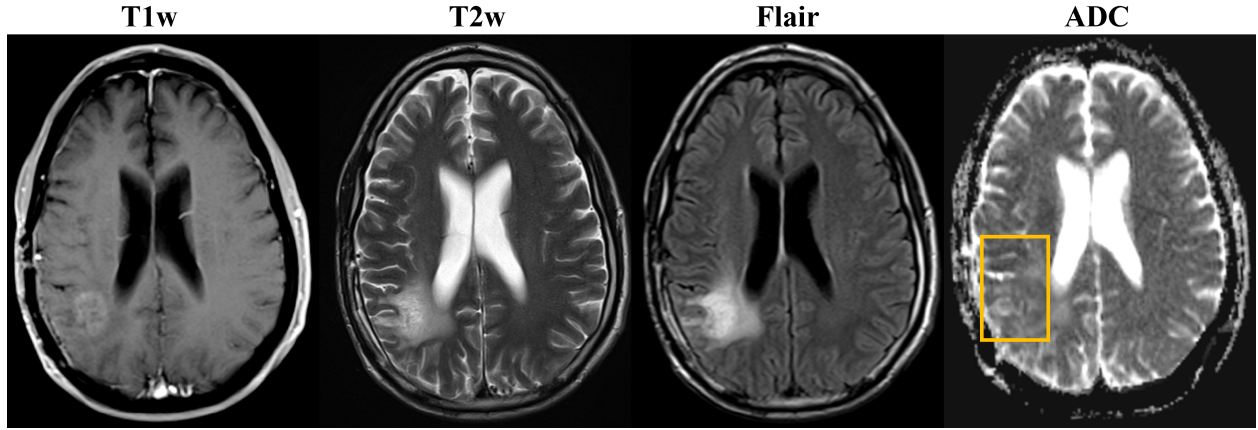


Figure 2.3: Types of MRI Sequences.

of multipliers [10] and others are used to find solutions for the k-space data acquired below the Nyquist rate.

2.3 Accelerating the MRI Reconstruction

Parallel Imaging (PI) methods, like Sensitivity Encoding (SENSE) and Penalised Auto-calibrating Partially Parallel Acquisitions (GRAPPA) have been used to accelerate the acquisition of MRI [97][44]. These are hardware-based techniques where instead of single receiver coil, multiple coils with focused sensitivities are used to collect the k-space data. Using a sophisticated MRI reconstructing algorithm, the information from multiple coils is processed to reconstruct the MRI. However, the acceleration factors achieved by PI methods are limited by the number of coils used for acquisition [27].

Prior-Information driven methods use techniques like regularization to obtain the solution of the under determined system equations [123]. Equation 2.4 defines a least square term with the regularization term.

$$\min_u \|Eu - k\|_2^2 + \lambda \mathcal{J}(u) \quad (2.4)$$

Here, $\mathcal{J}(u)$ is the regularizer; $\lambda > 0$ is the weighing term. Intuitively, the first term enforces the data consistency requirement where the reconstructed images “u” are consistent with the acquired k-space data. The regularizer term is a form of prior knowledge available

about the solution space. In the case of MRI, various regularization priors have been used to obtain the best estimates from undersampled k-space data. These priors try to exploit the redundancy in the MR image domain, spatio frequency domain, k-space and time-domain, for example, cardiac imaging, or a combination of them [113]. For dynamic imaging methods like cardiac imaging, the temporal correlations between scans acquired at two-time points are exploited to acquire accelerated MRI [80]. Methods such as k-t BLAST (Broad-use Linear Acquisition Speed-up Technique) and k-t SENSE under-sample the RF data in both the spatial and temporal domain [113]. In addition, some commonly used priors are total variation-based priors, sparsity-based priors, low-rank-based priors, etc.

Compressed sensing-based image reconstruction methods can be expressed as shown in Equation 2.5.

$$\min_u \|Eu - k\|_2^2 + \lambda \|\Psi u\|_1 \quad (2.5)$$

Here, Ψ is a sparsity enforcing transform domain. The premise for compressed sensing-based MRI reconstruction methods is that the MR images may not be sparse but may be expressed with lesser coefficients in the sparsifying transform domain. Few examples of the sparse domains include difference function, wavelet domain, temporal domain in case of cardiac imaging, etc [125][78]. Sparsifying transforms, like overcomplete dictionaries generated from the data model, wavelet domain, finite differences, spatiotemporal separations and principal component analysis have also been used to estimate parameter maps directly from undersampled k-space data [29][30][96][132]. Furthermore, low-rank and model-based methods have been used to estimate MRI parameter maps from nonlinear model equations [9]. Low-rank-based constraints representing the linearized version of parameter maps obtained from training data [50][133] model consistency constraint (MOCCO) and MOCCO-local subspace have been used to estimate MRI parameter maps directly from the k-space data [81].

Total Variation (TV)-based priors [101] have been used by many researchers to compensate for the aliasing/noise caused by undersampling. Total variation-based MRI reconstruc-

tion in its basic form can be expressed by Equation 2.6.

$$\min_u \|Eu - k\|_2^2 + \lambda \sum_{n=1}^N |\nabla u_n| \quad (2.6)$$

Here, $\sum_{n=1}^N |\nabla u_n|$ is the total variation based prior. The MR images are only piecewise smooth. When sampled below the Nyquist rate, aliasing introduces noise in the reconstructed images, thereby increasing the TV [101]. As a result, the minimization of TV will smoothen the images and preserve edge information [69]. The concept of total variation has also been extended from the adjacent pixels to non-local regions to preserve the fine details of the reconstructed MRI [26]. Joint patch-based total variation can better characterize the image features [75]. In case of dynamic MRI there is a smooth transition in the temporal direction, constraints like TV, sparsity-based and nuclear norms are used to accelerate MRI reconstruction [51][127]. In addition, these second-order finite differences are beneficial when compared to the first-order total variation, especially in minimizing the staircase effect [62]. The single-channel total variation-based reconstruction has been extended to multichannel reconstruction. As mentioned in section 2.1, the different imaging modalities may highlight different tissue information however, their structural information remains unchanged. Joint reconstruction algorithms with different variants of TV priors were successfully used to jointly reconstruct multi-contrast MR and MR-PET images with high fidelity [33][121][20].

Additionally, joint total variation was also extended to the parallel MRI reconstruction and it has demonstrated superior performance to the reconstruction results of other parallel MRIs like GRAPPA, CGSPIRiT, SAKE, etc [124]. Studies to investigate the effects of various norms across different dimensions like contrast, modality, gradient and pixel have been conducted[23]. Vectorial/scalar TV and isotropic/anisotropic TV have also been tested by Researchers. In addition to using only the TV prior, combinations of compressed sensing priors and low rank-based approaches are being investigated to improve the efficacy of joint image reconstruction [52][127]. With the advent of deep learning methods, many studies

focus on developing AI-based fast acceleration reconstruction techniques. Broadly, they can be divided into the data-driven methods and model-based methods. Data-driven methods rely on training and learning one-to-one mapping between the k-space and image domain. On the other hand, model-based techniques rely on strong mathematical optimization algorithms along with the training data, which reduces the number of training parameters. CNN-based methods, encoder-decoder-based networks, GAN based networks are some of the deep learning techniques that have been used to reconstruct T1w and T2w from the undersampled k-space data to achieve acceleration factors up to 8 to 16 times [122][106][60].

2.4 Fat and Water Estimation

MRI signal is obtained from the precessing hydrogen proton that may be part of the water which is attached to protein, carbohydrates or fat molecules. The desired signal contrast from the given tissue can be obtained by adjusting the T1 and T2 relaxation times. In general, the signal intensity from the fat is higher compared to other tissue types, which often overshadows the tissues like edema, tumor and other pathologies. As a result, fat suppression is necessary for better visualization of the intended pathology [8].

A number of techniques were demonstrated in the literature to separate the fat and water efficiently. The relaxation time T_1 of fat is smaller than other tissue types in the body. Hence, techniques like Short T1 Inversion Recovery (STIR) which suppresses the short T_1 values have been used for fat suppression [8][3]. The triglyceride molecules of fat are better shielded by electron cloud from the externally applied magnetic field than water's hydrogen protons. As a result, the hydrogen protons in fat precess at a lower frequency than in the water proton. Chemical Shift based methods thus rely on the difference between the resonance frequency of the hydrogen protons of water and fat. When compared to the water peak the largest of the multiple fat peak is separated by approximately 3.5 ppm as shown in Figure 2.4. The chemical shift gap is a function of the magnetic field strength [8][3]. Dixon method relies on acquiring the MRI at specific echo times when the protons are in-phase and out-phase

defined as $S_{in} = W + F$ and $S_{out} = W - F$ respectively. The in-phase and out-phase images when added and subtracted generate water $W = \frac{S_{in} + S_{out}}{2}$ and fat $F = \frac{S_{in} - S_{out}}{2}$ only images respectively [28]. This method suffered from local susceptibility effects and to overcome this problem a 3-point method was tested [40][41].

Several improvements have been carried out to the original Dixon method for robust estimation of water and fat. One such improvement was using the IDEAL (Iterative Decomposition of water and fat with Echo Asymmetry and Least-squares estimation) method proposed for multi-coil acquisition with higher SNR and delimiting the phase unwrapping problems [99]. However, the IDEAL method cannot estimate the T_2^* values. Correct estimates of fat are hampered due to the incorrect T_2^* estimates resulting from iron deposits and as a result, an extension to IDEAL was proposed to estimate the water content, fat content and T_2^* along with the complex field map [128]. Yet, this method constraints the estimated T_2^* value to be identical for water and fat. A different version proposed by Bydder et al. does treat T_2^* of water and fat separately but constraints the T_2^* value of fat smaller than that of water [13]. This makes the estimates of T_2^* values of water and fat interdependent which may not be true. Chebrolu et al. estimated separate relaxation rates of water and fat thereby improving the estimates of water and fat fractions [21]. In this work, the T_2^* MRI reconstruction is validated by estimating the fat and water using the framework proposed by chebrolu et al.

2.5 Multispectral Analysis of MRI

Several combinations of treatment methodologies are used for effective cancer management. Tumor heterogeneity is an important factor that affects the treatment response and their resistance to therapy, a deciding factor for the treatment to be successful. It is now well-recognized that when a tumor develops, the heterogeneity of molecular signatures expressed by the cancer cells increases. Development of resistance to targeted anti-cancer drugs frequently results from intratumoral heterogeneity of tumor phenotypes, the tumor

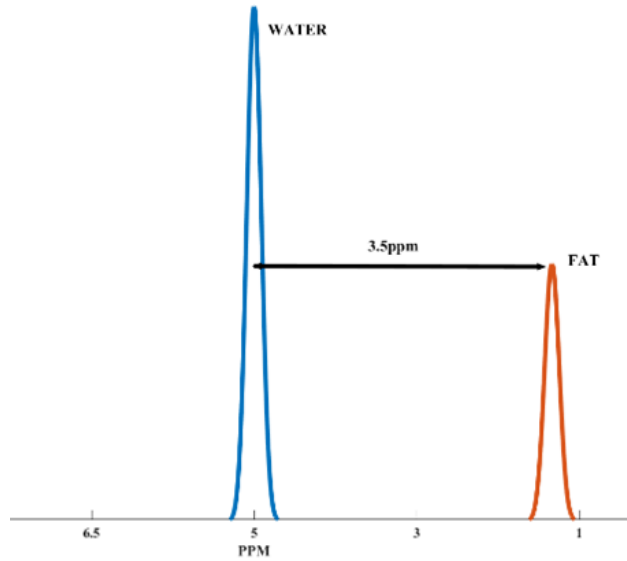


Figure 2.4: Water and Fat Peak Separated by ~ 3.5 ppm. (Image Adapted from [4]. Permission is included in Appendix D)

microenvironment and the interplay between these two factors. One view of solid tumors is that there is a continual Darwinian competition between drug-sensitive and drug-resistant phenotypes, with the relative success of the drug-resistant sub-population being dependent on the costs and benefits of the resistance mechanism in each microenvironmental tumor niche [37]. Adaptive therapeutic regimens are being tested clinically to exploit Darwinian dynamics within tumors to manage the development of resistance to therapies [35][131].

The promising feature of molecular imaging is that companion imaging diagnostics can be developed to inform precision medicine by providing non-invasive assays of the frequency and spatial distribution of the presence of specific molecular targets in a given patient's tumor [82]. It is determined that tumors comprise of several microenvironments that are hypoxic, necrotic or viable hence, tumor properties like perfusion, oxygenation, cell density and metabolism spatially vary within these microenvironments [55]. mpMRI like T1w, T2w, FLAIR and ADC maps exploit and can highlight different physiological tissue properties. They can therefore be used to visualize the tumor microenvironments. As seen in Figure 2.5, complex tumor characteristics like cell density and viability can be identified from ADC maps [55]. While T1w images can be important biomarkers for hemorrhage and blood products,

T2w images can identify the edema and mobile lipids within the tumor [16]. DCE images can highlight characteristics like perfusion, permeability and microvascular density within the tumor and can be used to determine if the underlying tissue is hypoxic or normoxic [55]. As a result, voxel-wise coregistered mpMRI can be analyzed to differentiate between tumor microenvironments.

The mpMRI can be compared to the satellite spectral images of the same geographical area but with different local variations of reflectance and emittance, which are often analyzed and fragmented into subregions using multispectral analysis. Analogously, multispectral analysis has also been applied on mpMRI to identify intratumoral habitats [115][116][42][110]. ADC maps, T2w and proton density maps have been subjected to a k-means clustering algorithm to identify the volumes of viable tumor tissue, necrosis and subcutaneous adipose tissues [16].

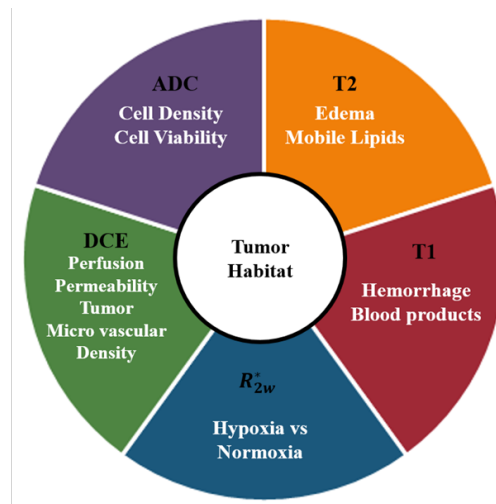


Figure 2.5: Multispectral Analysis of mpMRI.

Chapter 3: Framework to Identify the Intratumoral Habitats from mpMRI

3.1 Materials and Methods

3.1.1 Mice and Cell Culture

All procedures were approved by the IACUC at the University of South Florida, Tampa, Florida, USA. Mice were housed and used in accordance with IACUC-approved protocol number R1613 (Appendix F), standard operating procedures and IACUC principles of animal care and use, under a program fully accredited by AAALAC, with a written assurance on file with the PHS/NIH. Animals were fed standard chow and housed in specific pathogen-free conditions under a 12h/12h light/dark cycle. Female C57BL/6 mice (Charles River Laboratory, Inc.; Wilmington, MA) were inoculated with tumor cells at 7-8 weeks of age and 20 g in body weight. Lewis Lung Carcinoma (LLC) cells were obtained from the American Type Culture Collection and cultured in Dulbecco's Modified Eagle Medium supplemented with 10% fetal bovine serum. 5×10^5 LLC cells harvested in logarithmic growth were inoculated subcutaneously in volumes of 100 μ L into the backs of six syngeneic C57BL/6 mice ¹

3.1.2 Acquisition of Magnetic Resonance Imaging

All MRI measurements were made on a 7 T horizontal bore imager equipped with 600 mT/m self-shielded gradients (Bruker Biospin, Billerica, MA) using a 35 mm Litzcage small animal imaging coil (Doty Scientific, Columbia, SC). Mice were anesthetized using isoflurane, 2% in O₂, 1.5 L/min and animal body temperature was continuously monitored using a rectal thermometer (SAII, SA Instruments, Stony Brook, NY) and maintained at

¹This chapter is published in NMR in Biomedicine[95]. Permission is included in Appendix A.

37°C by an external heater. Respiratory function was monitored using a pressure transducer pad, SA Instruments, and maintained between 40-60 breaths/min.

All k-space data were acquired with cartesian encoding at the Nyquist Rate, from which undersampled k-space data were created using sampling masks. First, T2w FSE k-space data were acquired as high-quality anatomic reference information for the joint reconstruction algorithm. Co-registered T2w, T2w*, and T1w k-space data were then acquired with a common slab isocenter, number of slices (11), slice thickness (1 mm), field-of-view (35 mm x 35 mm), and matrix size (128 x 128). T2w k-space data were acquired using a multi-slice spin-echo sequence with a TR of 2400 ms, echo train length of 16 echoes, and echo spacing of 7.68 ms with the TE varied from 7.68 ms up to 122.88 ms. T2*w k-space data were acquired using a multi-gradient-echo sequence with an echo train length of 10, echo spacing of 3.84 ms, and TE varied from 3.84 ms to 38.4 ms. In-phase and opposed-phase T2* maps were calculated using TE ranging 3.84 ms to 38.4 ms, and 4.32 ms to 38.88 ms, respectively. A series of progressively saturated T1w spin-echo images were acquired with TE = 6.44 ms and TR = 232.3, 453.4, 737.5, 1136, 1808, and 5000 ms.

3.2 Joint Reconstruction Framework for T1w Images and T1 Maps

3.2.1 Proposed Method

The proposed algorithm is derived from the method reported by Ehrhardt and Betcke [32] wherein a single T1w image ‘u’ was reconstructed from undersampled k-space data by using a fully sampled T2w image ‘v’ to minimize the TV and improve confidence in the preservation of edge information. This is expressed by Equation 3.1.

$$wTV(u) := \sum_{n_1=1}^{N_1} \sum_{n_2=1}^{N_2} w_{(n_1, n_2)} |\nabla u_{(n_1, n_2)}| \quad (3.1)$$

Here, $w_{(n_1, n_2)} = \eta / |\nabla v_{(n_1, n_2)}|_\eta$ is a weighted total variation and $\eta > 0$.

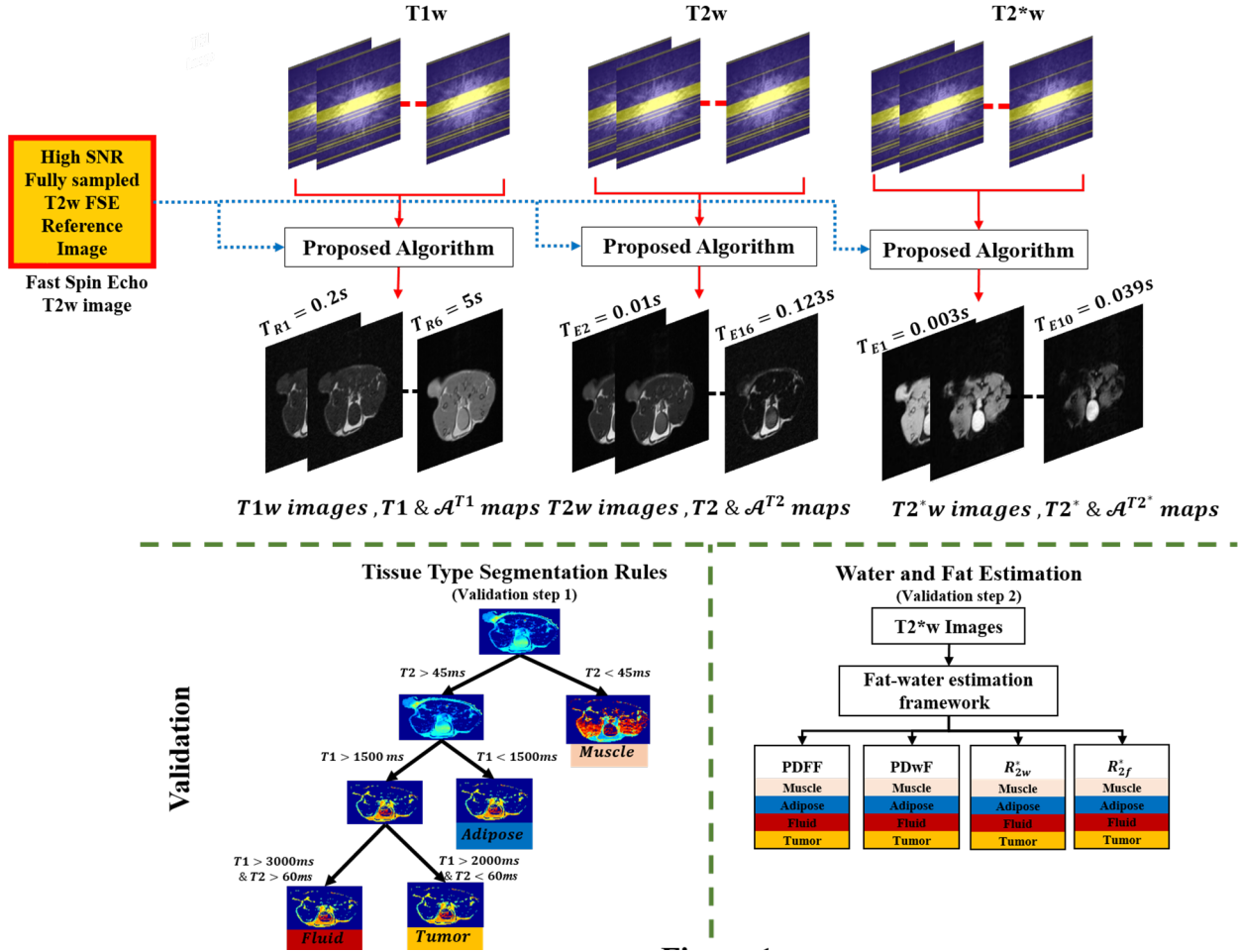


Figure 3.1: Block Diagram of Joint Reconstruction Algorithm.

We have extended the algorithm to jointly reconstruct a series of T1w images, \mathcal{A}^{T1} , proton density maps for T1 and T1 maps from undersampled k-space data using prior information from a co-registered high-quality fully sampled FSE reference image. In addition to this the reconstructed series of T1w images must satisfy the longitudinal relaxation model equation. This constraint will enable to preserve the relative contrast between the reconstructed T1w images.

As stated above, fully sampled Cartesian-encoded k-space data corresponding to T1w are initially acquired, which were processed by 2D FFT to generate GT T1w images. Variable density sampling masks with a high number of rows covering the center of k-space and randomly selected rows farther from the center along the phase-encoding direction were used

to generate undersampled k-space data for reconstruction. For a given rate of undersampling, the same mask was applied to all the repetition times of T1w.

The output of the reconstruction is a series of T1w images of size N1-by-N2-by-M, $\mathcal{A}_{(n_1, n_2)}^{T1}$, and the T1 map. $\mathcal{A}_{(n_1, n_2)}^{T1}$ and $T1_{(n_1, n_2)}$ are N1-by-N2 matrices of pixels representing \mathcal{A} and T1 maps, respectively. Undersampling a full data vector is represented using elementwise (Hadamard) multiplication of the k-space data and a mask S of size $N1 \times N2$ consisting of zeros and ones. The objective function to minimize our joint reconstruction problem is a linear combination of three terms: The least squares term that enforces the consistency between the M (complex) reconstructed T1w MR images is expressed by Equation 3.2.

$$\sum_{m=1}^M \sum_{n_2=1}^{N2} \sum_{n_1=1}^{N1} \frac{(S \cdot Fu^{(m)})_{(n_1, n_2)} - k_{(n_1, n_2)}^{(m)}}{2} \quad (3.2)$$

The weighted Joint Total Variation (wJTV) can be defined by Equation 3.3.

$$\sum_{m=1}^M \sum_{n_2=1}^{N2} \sum_{n_1=1}^{N1} \frac{\eta}{\sqrt{|\nabla v_{(n_1, n_2)}|^2 + \eta^2}} \sum_{m=1}^M |\nabla u_{(n_1, n_2)}^{(m)}| \quad (3.3)$$

Here, the edge template $\nabla v_{(n_1, n_2)}$ (where v is the fully sampled T2w FSE reference image) is derived from the fully-sampled image. The parameter $\eta \geq 0$ controls the weighting $w = \frac{\eta}{\sqrt{|\nabla v_{(n_1, n_2)}|^2 + \eta^2}}$ [32]. As a result, the minimization of the JTV for the given set of T1w images would be a logical prior. The edge template is exploited to spare the TV contribution of the edges in $u_{(n_1, n_2)}^{(m)}$ from the minimization. The least squares term that enforces the consistency between the M reconstructed T1w MR images and the relaxation model $\mathcal{A}_{(n_1, n_2)}^{T1}(1 - e^{-t_m/T1_{(n_1, n_2)}})$ postulated in the given tissue using Equation 3.4.

$$\sum_{m=1}^M \sum_{n_2=1}^{N2} \sum_{n_1=1}^{N1} \left[|u_{(n_1, n_2)}^{(m)}| - \mathcal{A}_{(n_1, n_2)}^{T1} \left(1 - e^{-t_m/T1_{(n_1, n_2)}} \right) \right]^2 \quad (3.4)$$

Here, $(t_m)_{m=1}^M$ are the operator-defined acquisition parameter TR, and $T1_{(n_1, n_2)}$ is the average relaxation time of tissue in the pixel at coordinate (n_1, n_2) . For readability we suppress the subscripts and abbreviate the functional to be minimized using Equation 3.5.

$$\min_{u^{(m)} \in \mathbb{C}^{N_1 \times N_2}, \mathcal{A}^{T1}, T1 \in \mathbb{R}^{N_1 \times N_2}} \sum_{m=1}^M \left\{ \frac{\|S \circ Fu^{(m)} - k^{(m)}\|_2^2}{2} + \alpha_1 \|[\mathcal{D}u]^{(m)}\|_1^1 + \alpha_2 \left\| u^{(m)} - \mathcal{A}^{T1} \left(1 - e^{-\frac{t_m}{T1}} \right) \right\|_2^2 \right\} \quad (3.5)$$

$$\text{Here, } [\mathcal{D}u]^{(m)} = \frac{\eta |\nabla u^m|}{\sqrt{|\nabla v^m|^2 + \eta^2}}.$$

3.2.2 Optimization Framework

The optimization is executed iteratively using an alternating direction strategy. First, we split the functional into computationally simpler sub-problems. For this, we rearrange the unconstrained optimization problem into a constrained form using Equation 3.6.

$$\min_{u^{(m)} \in \mathbb{C}^{N_1 \times N_2}, \mathcal{A}^{T1}, T1 \in \mathbb{R}^{N_1 \times N_2}} \sum_{m=1}^M \left\{ \frac{\|S \circ x^{(m)} - k^{(m)}\|_2^2}{2} + \alpha_1 \|[\mathcal{D}u]^{(m)}\|_1^1 + \alpha_2 \left\| F^{-1}x^{(m)} - \mathcal{A}^{T1} \left(1 - e^{-\frac{t_m}{T1}} \right) \right\|_2^2 \right\} \quad (3.6)$$

such that $x = Fz$ and $u = z$. Here α_1, α_2 are Lagrangian coefficients. Note that $\|F^{-1}x^{(m)} - \mathcal{A}^{T1}(1 - e^{-\frac{t_m}{T1}})\|_2^2 = \|x^{(m)} - F\mathcal{A}^{T1}(1 - e^{-\frac{t_m}{T1}})\|_2^2$ since the 2-dimensional Fourier transform is unitary. Accordingly, the associated scaled augmented Lagrangian is defined using Equation 3.7.

$$\sum_{m=1}^M \left\{ \frac{1}{2} \|S \circ x^{(m)} - k^{(m)}\|_2^2 + \alpha_1 \|[\mathcal{D}u^{(m)}]\|_1^1 + \alpha_2 \left\| F^{-1}x^{(m)} - \mathcal{A}^{T1}(1 - e^{-t_m/T1}) \right\|_2^2 + \frac{\rho}{2} \|x^{(m)} - Fz^{(m)} + \mu^{(m)}\|_2^2 - \frac{\rho}{2} \|\mu^{(m)}\|_2^2 + \frac{\rho}{2} \|u^{(m)} - z^{(m)} + \gamma^{(m)}\|_2^2 - \frac{\rho}{2} \|\gamma^{(m)}\|_2^2 \right\} \quad (3.7)$$

Here, $\mu^{(m)}$ and $\gamma^{(m)}$ are (complex) scaled dual variables and ρ an augmented Lagrangian parameter [10], and we have applied unitarity liberally. The alternating direction approach for the minimization of Equation 3.7 proceeds as follows. Note that for each iteration of the ADMM algorithm, L1 = 5 iterations of weighted FJGP (wFJGP), a variant of the Fast Gradient Projection [7] and FJGP algorithm [51], and L2 = 15 iterations of the Levenberg-Marquardt algorithm [45] were executed. A common number of iterations was heuristically chosen for all undersampling rates to permit comparison of reconstruction results across the different undersampling rates. L3 = 20 iterations of the ADMM algorithm yielded satisfactory reconstruction results for all 30 slices. The regularization parameters of $\eta = 0.1, \alpha_1 = 0.1, \alpha_2 = 0.008, \rho = 1$ and $\mu = 10$ are chosen heuristically for this dataset. For fixed $x, z, \mathcal{A}^{T1}, T1$, perform L1 iterations of the wFJGP algorithm using Equation 3.8.

$$\operatorname{argmin}_{u^{(m)} \in \mathbb{C}^{N1 \times N2}} \sum_{m=1}^M \left\{ \alpha_1 \left\| [\mathcal{D}u]^{(m)} \right\|_1 + \frac{\rho}{2} \left\| u^{(m)} - z^{(m)} + \gamma^{(m)} \right\|_2^2 \right\} \quad (3.8)$$

For fixed $u, z, \mathcal{A}^{T1}, T1$, execute Equation 3.9.

$$\operatorname{argmin}_{x^{(m)} \in \mathbb{C}^{N1 \times N2}} \sum_{m=1}^M \left\| S \circ x^{(m)} - k^{(m)} \right\|_2^2 + \alpha_2 \left\| F^{-1} x^{(m)} - \mathcal{A}^{T1} (1 - e^{-\frac{tm}{T1}}) \right\|_2^2 + \frac{\rho}{2} \left\| x^{(m)} - Fz^{(m)} + \mu^{(m)} \right\|_2^2 \quad (3.9)$$

The objective function here is simply an uncoupled sum of (complex) quadratics, and the solution is immediate and defined by Equation 3.10.

$$x^m = [S + (\rho + 2\alpha_2)]^{-1} \left[2\alpha_2 F \mathcal{A}^{T1} \left(1 - e^{-\frac{tm}{T1}} \right) + k^{(m)} + \rho (Fz^{(m)} - \mu^{(m)}) \right] \quad (3.10)$$

(Recall that $S = ST = STS$.)

For fixed $u, x, \mathcal{A}^{T1}, R$ execute Equation 3.11.

$$\begin{aligned} \operatorname{argmin}_{z^{(m)}} \sum_{m=1}^M \frac{\rho}{2} \left\{ \|x^{(m)} - Fz^{(m)} + \mu^{(m)}\|_2^2 + \|u^{(m)} - z^{(m)} + \gamma^{(m)}\|_2^2 \right\} \\ = \frac{F^{-1}(x^{(m)} + \mu^{(m)}) + u^{(m)} + \gamma^{(m)}}{2} \end{aligned} \quad (3.11)$$

again, an uncoupled sum of quadratics.

For fixed u, x, z execute $L2$ iterations of the Levenberg-Marquardt algorithm using Equation 3.12.

$$\operatorname{argmin}_{\mathcal{A}^{T1}, T1} \sum_{m=1}^M \sum_{n=1}^N \left| z_n^{(m)} - \mathcal{A}^{T1}(1 - e^{-\frac{tm}{T1}}) \right|^2 \quad (3.12)$$

Detailed steps of ADMM Algorithm and wFJGP are shown in Algorithm 1 and Algorithm 2 respectively. For the wFJGP algorithm derived from [51][7], the definition of \mathbb{P}_T and \mathbb{P}_U are defined using Equation 3.13.

$$\mathbb{P}_T(x) = \max(x, 0) \quad (3.13)$$

\mathbb{P}_U is a projection operator and can be defined as $\mathbb{P}_U(U, V) = (P, Q)$ to satisfy the following.

$$\begin{aligned} P_{n_1, n_2, m} &= \frac{U_{n_1, n_2, m}}{\max(1, \sqrt{\sum_{m=1}^{m=M} U_{n_1, n_2, m}^2 + V_{n_1, n_2, m}^2})}, \\ n_1 &= 1, 2, \dots, N1 - 1; n_2 = 1, 2, \dots, N2 - 1 \\ &= \frac{U_{n_1, N2, m}}{\max(1, \sqrt{\sum_{m=1}^{m=M} U_{n_1, N2, m}^2})}, \quad n1 = 1, 2, \dots, N1 - 1; \\ Q_{n_1, n_2, m} &= \frac{V_{n_1, n_2, m}}{\max(1, \sqrt{\sum_{m=1}^{m=M} U_{n_1, n_2, m}^2 + V_{n_1, n_2, m}^2})}, \\ n_1 &= 1, 2, \dots, N1 - 1; n_2 = 1, 2, \dots, N2 - 1 \end{aligned}$$

$$= \frac{U_{N1,n2,m}}{\max(1, \sqrt{\sum_{m=1}^{m=M} V^2_{N1,n2,m}})}, \quad n_2 = 1, 2, \dots, N2 - 1;$$

This algorithm was coded in MATLAB R2018b, The MathWorks, Inc., Natick, MA, USA with standard and in-house developed functions and scripts that are available upon request. On a basic workstation with an Intel I5 processor @ 3GHz and 8 Gb RAM the computation times for reconstructing complex T1w and T2w images and corresponding parameter maps was 108 s and 55 s respectively for the various % of k-space undersampling.

3.2.3 Extension Framework for T2w/T2*w Images and their Maps

We extended the joint reconstruction framework to reconstruct the series of T2w/T2*w images and T2/T2* maps. While the data consistency term (3.2) and the joint total variation term (3.3) are unchanged the constraint for model equation are defined by the transverse relaxation model equation defined by $\mathcal{A}_{(n_1, n_2)}^{T2}(e^{-t_m/T2(n_1, n_2)})$. Correspondingly, the least squares term that enforces the consistency between the M reconstructed T2w/T2*w MR images and the transverse relaxation model equation postulated in the given tissue is defined as Equation 3.14.

$$\sum_{m=1}^M \sum_{n_2=1}^{N2} \sum_{n_1=1}^{N1} [|u_{(n_1, n_2)}^{(m)}| - \mathcal{A}_{(n_1, n_2)}^{T2}(e^{-t_m/T2(n_1, n_2)})]^2 \quad (3.14)$$

Here, $\{t_m\}_{m=1}^M$ are the operator-defined acquisition parameter TE, and $T2(n_1, n_2)$ is the average relaxation time of tissue in the pixel at coordinate (n_1, n_2) . In-phase and opposed-phase T2*w images were reconstructed separately, to permit the use of a mono-exponential relaxation model constraint for each set.

Algorithm 3.1 ADMM Algorithm to Solve Joint Reconstruction

Input: $k^m \equiv S \circ k^m \in \mathbf{C}^{N1 \times N2}$ MRI Data

S : Sampling Mask

$L_3 \in \mathbf{N}$ number of iterations

$u_0^m = F^{-1}(Sk^m) \in \mathbf{C}^{N1 \times N2}$ Initialization of M images

$A_0^{T1}(1 - e^{-tm/T1_0}) \leftarrow u_0^m$ Initialize $A_0^{T1}, T1 \in \mathbf{R}^{N1 \times N2}$ using Levenberg-Marquardt Method

Output: $u^m \in \mathbf{C}^{N1 \times N2}$

function: JointReconstruction($k^m, S, itr, u_0^m, A_0^{T1}, T1_0$)

$\alpha_1, \alpha_2 \geq 0, \eta > 0, \rho_0 \leftarrow 1, \mu_0^m, \nu_0^m \leftarrow 0$

for $i = 1:L_3$ Compute

$u_i^{(m)}$ update using weighted-(FJGP) algorithm with total L_1 iterations

$$x_i^{(m)} \leftarrow \frac{2\alpha_2 F A_{i-1}^{T1} (1 - e^{-tm/T1_{i-1}}) + k^{(m)} + \rho(Fz_i^{(m)} - \mu_{i-1}^{(m)})}{S + \rho_{i-1} + 2\alpha_2}$$

$$z_i^{(m)} \leftarrow \frac{F^{-1}(x_i^{(m)} + \mu_{i-1}^{(m)} + u_i^{(m)} + \nu_{i-1}^{(m)})}{2}$$

$A_i^{T1}, T1_i \in z_i^{(m)}$ update using Levenberg-Marquardt Method with total L_2 iterations

$$\mu_i^{(m)} \leftarrow \mu_{i-1}^{(m)} + \rho_{i-1}(x_i^{(m)} - Fz_i^{(m)})$$

$$\nu_i^{(m)} \leftarrow \nu_{i-1}^{(m)} + \rho_{i-1}(u_i^{(m)} - z_i^{(m)})$$

Update $\rho_i \leftarrow \rho_{i-1}$

return $u_i^{(m)}$

3.3 Validation Framework

We applied the joint reconstruction framework on 30 mouse slices, 6 mice with 5 slices each. The quantitative validation of our reconstructed results was carried out using all 30 mouse slices at 4 stages of our framework, as discussed below.

3.3.1 T1w and T2w MRI

Mutual Information (MI) [25][11] is a metric of image matching calculated between the reconstructed and GT image. MI values signify how similar the reconstructed images are to the corresponding GT images on a pixel-by-pixel basis. The statistical analysis was carried out over $n = 30$ mouse slices, 6 mice with 5 slices each since each slice from a given mouse was reconstructed from under-sampled k-space data independently of the other slices. Quantitative validation for reconstructed T1w and T2w images was carried out by calculating the mean and SEM of MI values over $n = 30$ slices.

Algorithm 3.2 weighted Fast Joint Gradient Projection (wFJGP) Algorithm

Input: $y^m \in \mathbf{C}^{N_1 \times N_2}$ is a proximal point

$\alpha_1 \in \mathbf{R}, \gamma \in \mathbf{R}, t_0 \leftarrow 1, h_0 \in \mathbf{R}$

$L_1 \in \mathbf{N}$ number of iterations

$y^m = z^m - \frac{v^m}{\rho}$ Initialization from ADMM Algorithm

$w \in \mathbf{R}^{N_1 \times N_2}, \mathbf{P}, \mathbf{Q}, \mathbf{U}, \mathbf{V} \in \mathbf{C}^{N_1 \times N_2}$

Output: $u^m \in \mathbf{C}^{N_1 \times N_2}$

Function: wFJGP($w, y^m, L_1, \mathbf{P}_0^m, \mathbf{Q}_0^m, \mathbf{U}_0^m, \mathbf{V}_0^m, t_0, \gamma$) for $j = 1:L_1$ Compute

$g_j^m \leftarrow \alpha_1 w \circ \nabla [P_T(y + \alpha_1 \text{div}((\mathbf{P}_{j-1}^m, \mathbf{Q}_{j-1}^m) \circ w))]$

$(\mathbf{U}_j^m, \mathbf{V}_j^m) \leftarrow P_U((\mathbf{P}_{j-1}^m, \mathbf{Q}_{j-1}^m) + \gamma g_j^m)$

$h_j \leftarrow \frac{1 + \sqrt{1 + 4(t_{j-1})^2}}{2}$

$(\mathbf{P}_j^m, \mathbf{Q}_j^m) \leftarrow (\mathbf{U}_j^m, \mathbf{V}_j^m) + \frac{t_{j-1}-1}{h_j}(\mathbf{U}_j^m - \mathbf{U}_{j-1}^m, \mathbf{V}_j^m - \mathbf{V}_{j-1}^m)$

$h_j \leftarrow t_j$

End For

$u^m \leftarrow P_T(y^m + \alpha_1 \text{div}((\mathbf{U}_j^m, \mathbf{V}_j^m) \circ w))$

return u^m

3.3.2 T1 and T2 Maps

A tissue type segmentation framework is used to identify four tissue types, tumor, muscle, fluid, and adipose, from the reconstructed T1 and T2 maps and compared to those obtained from GT T1 and T2 maps. The GT T1 and T2 maps were obtained by fitting the GT T1w and T2w images to the longitudinal and transverse relaxation model equations, respectively. As shown in Figure 3.1, voxels were classified as fluid, adipose, muscle, or tumor tissue types based on the following rules applied to the T1 and T2 maps. Voxels with T2 < 45 ms are classified as muscle. A mask of all the remaining voxels with T2 >= 45 ms is applied to the T1 map. Voxels within this mask with T1 < 1500 ms are classified as adipose tissue, with the remainder of voxels constituting a mask to which the following rules are applied: voxels with T1 > 3000 ms and T2 > 60 ms are designated as fluid, while voxels with T1 > 2000 ms and T2 < 60 ms are designated as tumor tissue type. The threshold values for T1 and T2 that comprise these rules are determined from the averages of values within the hand-drawn region of interest over the four tissue types on GT images, n = 30, from 6

Table 3.1: Quantitative Validation of Joint Reconstruction Algorithm.

Mean T2 values (ms)					Mean T1 values (ms)					Dice Coefficient			
GT	JTV		FCSA-MT		GT	JTV		FCSA-MT		JTV		FCSA-MT	
	36%	27%	36%	27%		36%	27%	36%	27%	36%	27%	36%	27%
135	125	126	129	131	3949	3208	3160	2756	2778	0.88	0.84	0.71	0.62
67	69	70	65	64	935	973	992	1062	1074	0.91	0.88	0.89	0.88
33	43	43	42	42	2344	2619	2736	2097	2072	0.91	0.86	0.86	0.79
53	51	51	52	52	2829	2664	2696	2239	2257	0.42	0.30	0.26	0.20

mice with 5 slices per mouse. The mean and SD of the reconstructed T1 and T2 maps were calculated over $n = 30$ mouse slices for different undersampling rates and compared to the corresponding mean and SD values in GT maps. To validate the tissue type segmentation maps for different rates of undersampling, the mean and SEM of the dice coefficient values were computed over $n = 30$ slices.

3.3.3 T2*w MRI

The GT T2*w images are subjected to the fat and water estimation framework proposed by Reeder and colleagues [21] to obtain GT PDFF, PDwF, R_{2f}^* , R_{2w}^* , and Ψ maps. The process is repeated for the reconstructed T2*w images obtained from the proposed algorithm. The mean and SD of the PDFF, PDwF, R_{2f}^* , R_{2w}^* in each of the tissue types across all reconstructed 30 mouse-slices is calculated and compared against their GT counterparts.

3.3.4 Comparison with FCSA-MT Algorithm

We have also compared results from our proposed algorithm to those obtained using the FCSA-MT algorithm [52]. Briefly, T1w images are jointly reconstructed from the under-sampled k-space data using the FCSA-MT algorithm. These reconstructed T1w images are fit to the longitudinal relaxation model equation to compute T1 maps. This process is repeated for T2w images and T2 maps. The T1 and T2 maps obtained thus are subjected to the tissue type segmentation rules in Figure 3.1 to segment the images into adipose, fluid, muscle, and tumor tissue types. The T2*w images are also reconstructed analogously

using the FCSA-MT algorithm, and these are processed using the fat and water estimation framework to compute maps of PDFF, PDwF, R_{2f}^* and R_{2w}^* .

3.4 Results

Figure 3.2 shows example T1w images of two mice for TR of 0.4 s (2nd, 4th columns) and 5 s (3rd, 5th columns), reconstructed with 27% and 36% of the k-space data using the sampling mask in the 1st column. MI values for reconstructed T1w images with the different TR are presented in the last column of Figure 3.2. Expectedly, MI values increase monotonically with the increasing amount of k-space used in the reconstruction at all TR. However, the rate of improvement starts to flatten as more k-space data is used for the reconstruction. For a given percent of k-space data, mean MI values are higher for higher TR. Overall, the under-sampled reconstructions show good agreement with the GT T1 images, last row, reflected in MI values ranging from 1.35-1.5. Qualitatively, edge information was preserved (6th and 7th columns, zoomed-in images), and preservation of the relative contrast within each image and across the different TR is also visible.

Figure 3.3a shows example T2w images of the same two mice and slices as in Figure 3.2, acquired with TE of 15.36 ms (1st, 3rd column) and 46 ms (2nd, 4th columns), reconstructed with 27% and 36% of the k-space data using the sampling mask shown in Figure 3.2. The under-sampled reconstructions show good similarity with the GT T2w images (bottom row), reflected in MI values ranging from 1.35 to 1.5. Preservation of the relative contrast within each image and across the different TE and edge features in the under-sampled reconstructions (5th and 6th columns, zoomed-in images) is also visible. The similarity between the under-sampled reconstructions and the GT T2w images of n=30 mouse slices imaged using the various TE are summarized in Figure 3.3b as plots of MI values. As with T1w images, MI values for T2w images are found to monotonically increase with the amount of k-space data used at all TE, with a flattening rate of improvement at higher percentages of k-space data used. The saturation of MI values, Figure 3.2 last column and Figure 3.3b as the amount of

k-space data increases can be attributed to the truncation effects resulting from the approximation of the wide range of Fourier frequencies with the limited number of Discrete Fourier coefficients. For a given percent of k-space data, mean MI values are higher for lower TE. Further, higher average MI values for shorter TE and longer TR images may be due to the superior signal-to-noise ratio.

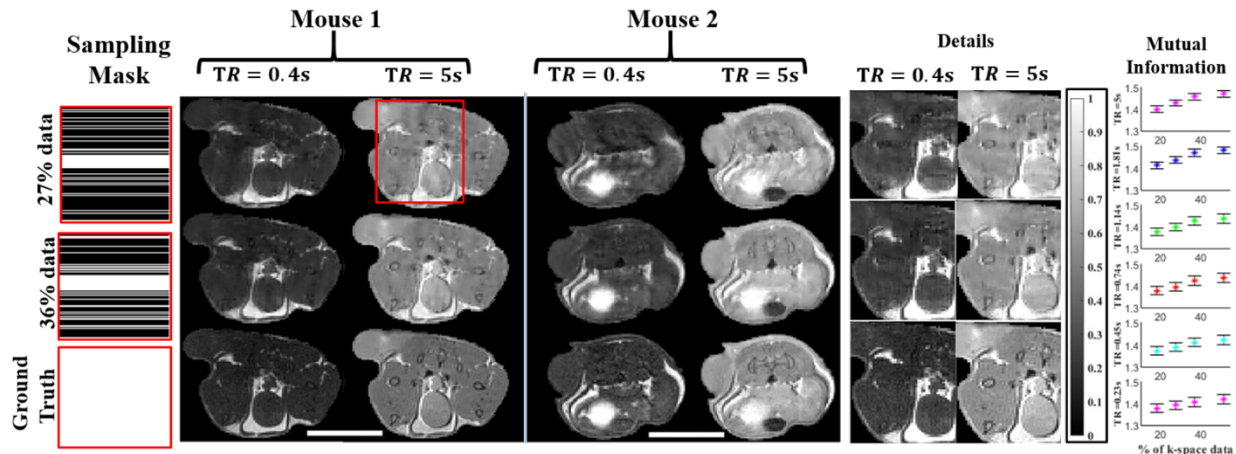


Figure 3.2: Reconstruction Results for T1w Images.

Figures 3.4a and 3.4b show example reconstructed T1 and T2 maps, respectively. Qualitatively, the T1 maps reconstructed using 27% and 36% of k-space data show a close resemblance to the GT T1 map (Figure 3.4a). Likewise, T2 maps reconstructed using 27% and 36% of k-space data resemble the GT T2 maps (Figure 3.4b). Compared with the GT maps, the reconstructed T1 and T2 maps appear to piecewise smoothen some regions, though edge details are still visible. Tissue type segmentation is performed using the T1 and T2 thresholding rules shown in Figure 3.1. Despite some loss of fidelity vis-à-vis the GT T1 and T2 maps, tissue type maps computed from under-sampled T1 and T2 maps show visual agreement with tissue type maps computed from GT T1 and T2 maps (Figure 3.4c).

Quantitatively, some of the regions in T1 maps are underestimated compared to GT maps, especially in the fluid region. The underestimation of T1 values in the fluid tissue type may be attributed to the longest TR acquired being only 5 s and the resulting fitting errors being exacerbated during the reconstruction of under-sampled data. Mean, and SD values

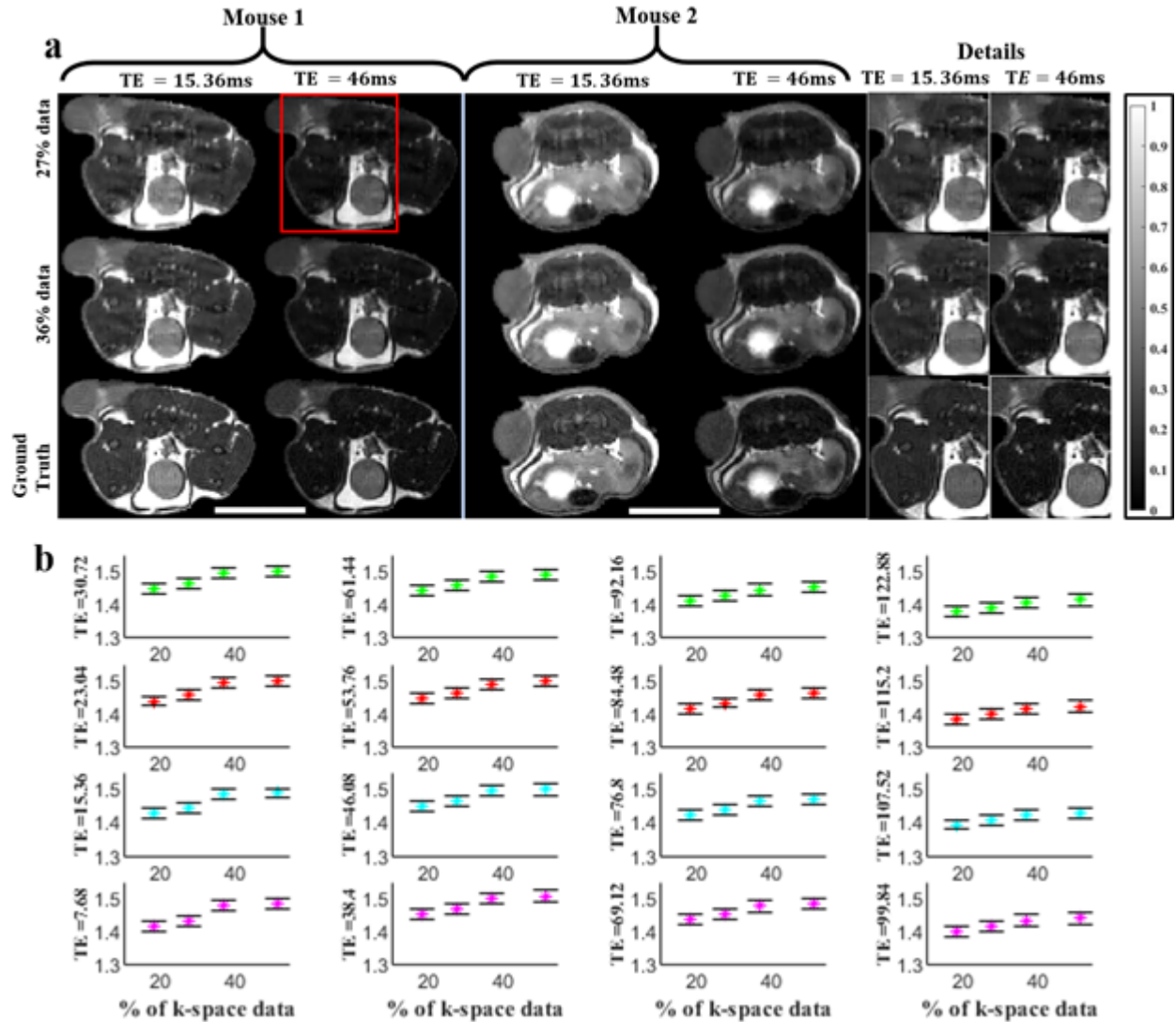


Figure 3.3: Reconstruction Results for T2w Images.

of T1 and T2 over all pixels within each objectively segmented tissue type are summarized in Figures 3.4d and 3.4e, respectively, for different amounts of k-space data used in the reconstructions. The SD values represent the true heterogeneity of T1 and T2 values within a tissue type. From Figure 3.4d, the mean T1 values of adipose, muscle, and tumor tissue types computed using 18-52% of the k-space data are comparable to GT T1 values. However, the mean T1 values in fluid computed from under-sampled data are somewhat underestimated compared to the GT T1 estimates. It can also be noted that the heterogeneity of T1 values, i.e., the SD, within the adipose tissue type is lower than in other tissue types, possibly because

of a T1-based rule used to define this tissue type. From Figure 3.4e, the mean T2 values of the tumor, fluid, and adipose tissue types computed using 18-52% of the k-space data are comparable to GT T2 values. In muscle, the estimated T2 values from under-sampled k-space data are somewhat overestimated compared to GT T2 values. Lower heterogeneity, i.e., SD, in the estimated and GT T2 values are observed within muscle and tumor relative to fluid and adipose tissue. This may be a consequence of rules used to define these tissue types; the muscle tissue type definition includes a rule that T2 should be lower than 45 ms, while the tumor tissue type definition includes a rule that the T2 value is between 45 and 60 ms. Figure 3.4f presents a quantitative characterization of the similarity of the tissue type maps computed from under-sampled data to the GT tissue type maps. The mean and SEM of the Dice coefficient computed for tissue type maps of $n = 30$ different mouse slices are depicted. Expectedly, the average Dice coefficient values increased as the amount of k-space data used in the reconstructions increased for all tissue types. Tissue type maps computed using 18% k-space data were visually similar to GT tissue type maps, with dice coefficients ranging from 0.43-0.73 for tumor, fluid, adipose, and muscle tissue types.

As described in the validation framework, T2*w images reconstructed from under-sampled k-space data are processed using the algorithm described by Reeder and colleagues [21]. This algorithm's outputs are maps of PDFF, PDwF, R_{2f}^* and R_{2w}^* , and the Ψ . The PDFF, PDwF, R_{2f}^* and R_{2w}^* maps computed using 27% and 36% of the k-space data and the corresponding GT maps are shown in Figures 3.5a and 3.5b for two example mouse slices. The mean and SD of PDFF, PDwF, R_{2f}^* and R_{2w}^* computed within fluid, adipose, muscle, and tumor tissue types are summarized in Figure 3.5c. Here too, SD measures the heterogeneity of the parameter values within a given tissue type as defined by the rules shown in Figure 3.1. Some loss of fidelity for the estimated PDFF and PDwF maps vis-à-vis the corresponding GT maps is apparent in Figure 3.5a. Nonetheless, the higher PDFF in the tumor region of both mice is preserved even on estimates from undersampled T2*w data. From the PDFF plots shown in Figure 3.5c, 1st column, it can be deduced that the mean PDFF

values are highest in adipose tissue (0.33), followed by tumor tissue (0.27), muscle (0.24), and fluid (0.23). The relative order of PDwF computed in the four tissue types agrees with expectations, with the highest PDwF computed in fluid (0.77), followed by muscle (0.76), tumor (0.73), and adipose tissue (0.67). Non-zero PDFF values are obtained in the fluid tissue type even for the GT PDFF maps, which may reflect the limitations of the algorithm in [21].

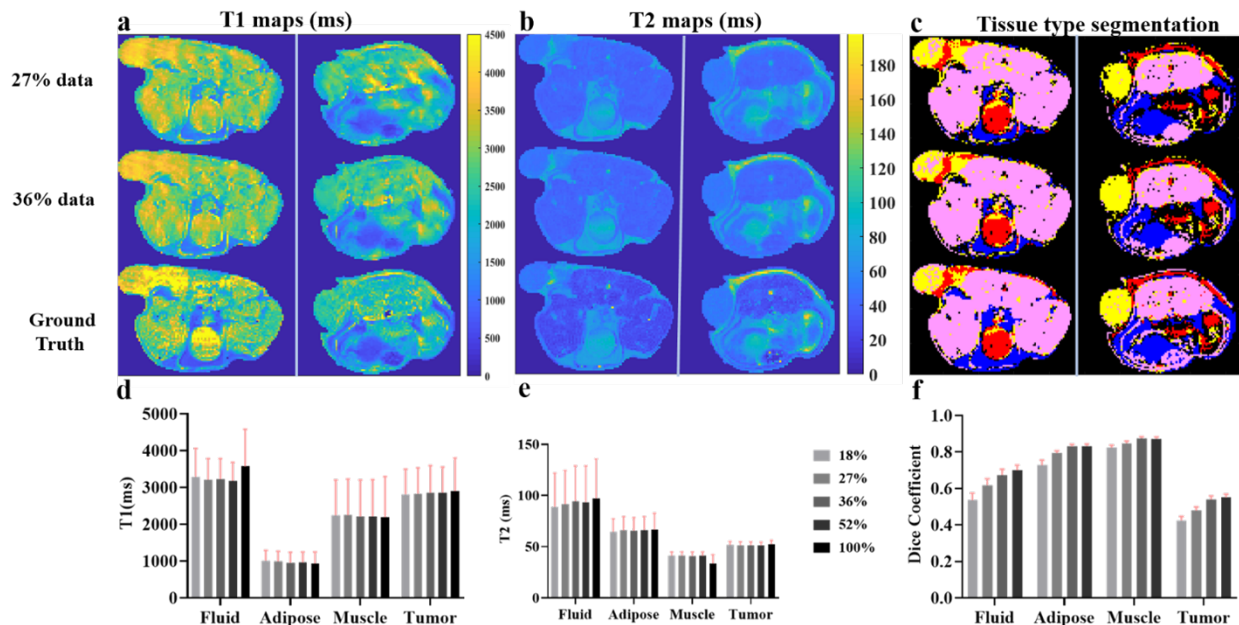


Figure 3.4: Results of T1 and T2 Parameter Maps and Tissue Type Maps.

In the case of PDFF and PDwF the GT values in the different tissue types may be inferred from physiology. But in the case of R_{2f}^* and R_{2w}^* the expected values are not as readily apparent. Based on R2 differences between water and fat one would expect $R_{2f}^* > R_{2w}^*$, although susceptibility effects might dominate both relaxation rates. Figure 3.5b shows maps of R_{2f}^* and R_{2w}^* computed from T2*w images reconstructed using 27% and 36% of the k-space data in two selected mouse-slices. In general, the R_{2f}^* and R_{2w}^* maps from undersampled data showed only moderate agreement with the corresponding GT maps. Moreover, both R_{2f}^* and R_{2w}^* computed from undersampled T2*w data tended to be underestimates of corresponding GT values in all tissue types (Figure 3.5c).

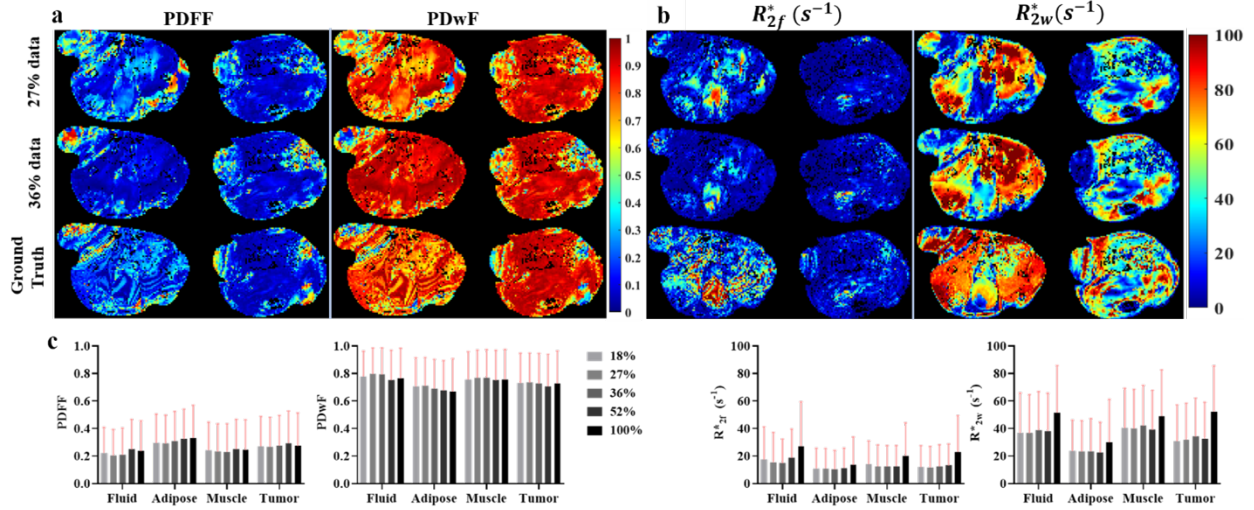


Figure 3.5: Results of PDFFF, PDwF and Relaxation Rates of Water and Fat.

We have compared the performance of the proposed joint reconstruction algorithm against results obtained using the FCSA-MT algorithm with tuned regularization parameters [52]. In Figure 3.6, reconstructed T1w images for $TR = 1.1$ s and 5 s are shown in columns 1 and 2, while reconstructed T2w images for $TE = 7.68$ ms and 23 ms are shown in columns 4 and 5. For reference, the GT images are shown in the bottom row. Using 36% k-space data, both the proposed algorithm and FCSA-MT produced images that are qualitatively like the GT. When using 27% k-space data, there was greater blurring of some of the finer details with the FCSA-MT algorithm compared to the proposed algorithm (Figure 3.6, 3rd column). T1 maps computed using the proposed algorithm and FCSA-MT algorithm are shown in column 6 of Figure 3.6. Both algorithms underestimate the T1 values in pixels that have long GT T1 values, though the proposed algorithm performs somewhat better than the FCSA-MT algorithm in this respect as summarized in Table 3.1. T2 maps computed using the proposed algorithm and FCSA-MT algorithm are shown in column 7 of Figure 3.6. Both algorithms tend to underestimate T2 in pixels with long T2 values, with the performance of the two algorithms being generally comparable, as summarized in Table 3.1. Tissue type segmentation results, using the rules in Figure 3.1 and the reconstructed T1 and T2 maps, were superior with the proposed algorithm compared to the FCSA-MT algorithm both qual-

itatively (Figure 3.6, column 8) and on the basis of Dice similarity coefficient with the GT tissue type maps (Table 3.1). PDFFF maps computed using the two algorithms are compared with PDFFF maps from GT data in column 9 of Figure 3.6.

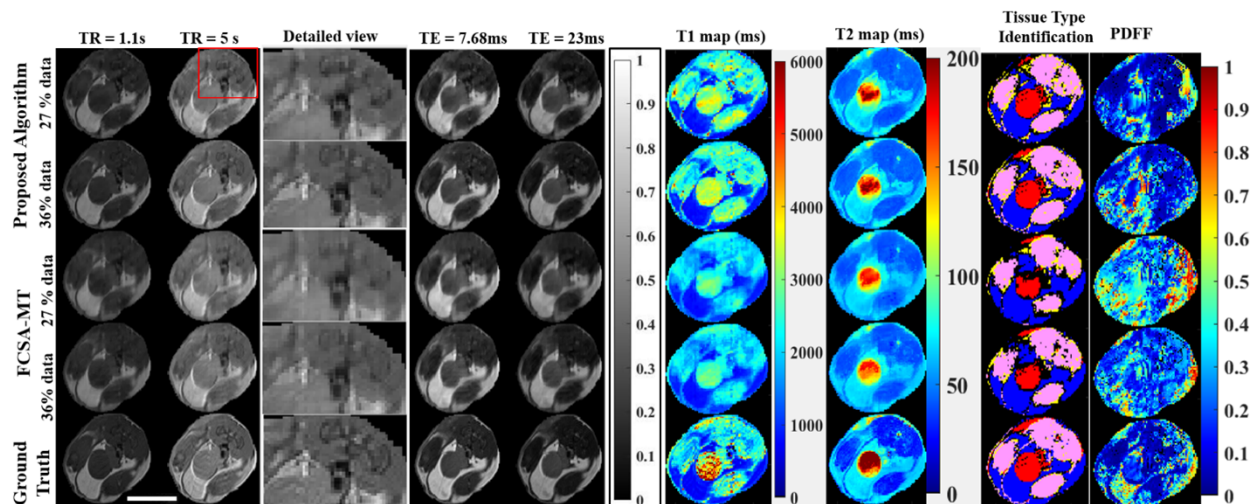


Figure 3.6: Comparison of Proposed Algorithm with FCSA-MT and GT.

3.5 Discussion

Our objective in this preliminary work is to demonstrate that the proposed image reconstruction approach can recapitulate maps of broad tissue types using undersampled k-space information. With the proposed framework, we jointly reconstructed a series of MRI and their parameter maps using 18% k-space data with Cartesian undersampling that is readily implementable on most preclinical MRI scanners. In this work, for a given percentage of k-space data, a common pattern was used to undersample k-space data across all the TRs in given series of T1w images. Greater improvements in the quality of reconstructions may be obtainable by using randomly varied undersampling patterns across different TRs for acquiring a given series of T1w k-space data. Qualitative image features and parameter maps such as edge and contrast were efficiently preserved in the reconstructed images. Although the mean T1 values in the fluid tissue type were underestimated relative to GT values, the overall heterogeneity in the reconstructed maps was preserved, and tissue type maps could

be objectively computed that bore a high similarity to GT tissue type maps based on Dice coefficient values. The tumor T1 values of ~ 2800 ms that we have measured are significantly longer than the 1000-1800 ms at 4.7 T [83][120] and 7 T [134][70][126] reported in various preclinical tumor models by other groups. The one noteworthy difference between our study and these other studies is that in our mice, tumor cells were inoculated subcutaneously on the backs of the animals rather than in the more common flank or orthotopic locations. There were pockets of fluid around the tumor that were visible on the images and in the parameter maps, which we have not previously noticed in flank tumor models, and this may be an explanation for the longer T1 values that we measured. The tumor T2 values that we measured (50-60 ms) agree with those reported recently by Tomaszewski et al. [112] in pancreatic tumor xenografts grown in mouse hind limbs. In our case, the proposed algorithm performed better than the FCSA-MT algorithm for the reconstruction of the T1w images and T1 maps, while the fidelity to GT of the reconstructed T2w images and T2 maps was comparable between the two methods. In the proposed algorithm, parameter maps are estimated from reconstructed images at each iteration, which provides an additional constraint on pixel values in the form of the relaxation model equation, in addition to information from the JTV, and improves the accuracy of the results of the reconstruction process.

Accelerated mpMRI parametric mapping will enable objective mapping of tissue histological characteristics [115][116][42][110][89] and intratumoral habitats [55][16][98][38][108], which in turn will enable the development of better imaging biomarkers for understanding tumor resistance to therapies and the development of adaptive anti-cancer therapy regimens [35][131]. Alternate approaches being investigated to this end include MR Fingerprinting (MRF), which is a dictionary-based technique that is gaining popularity for accelerated acquisition of mpMRI in research settings. Advances in MRF techniques for preclinical imaging include the development of specialized pulse sequences for MR vascular fingerprinting [73] and methods such as Regularly Incremented phase encoding MRF [5] to reduce sensitivity to motion. Our proposed method can accelerate mpMRI parametric mapping with under-

sampled Cartesian acquisition of k-space data. Accelerated methods for estimating PDwF, PDFF, R_{2f}^* , R_{2w}^* will enable improved understanding of tumor physiology and response to therapies. On our scanner, fully sampled T1w, T2w and T2*w data required a total scan time of approximately 34 minutes, which could theoretically be reduced to 6 minutes if acquiring only 18% of the k-space data (Table 3.2). The saved scan time may be used for acquiring additional functional MRI scans such as DW-MRI and DCE-MRI while keeping the total scan time low enough that the known perturbations of mouse and tumor physiology by prolonged anesthesia [77][6][56] are mitigated.

Table 3.2: Comparison of mpMRI Reconstruction Time.

MRI Scan Type	Fully sampled (128 lines)	18% k-space	27% k-space	36% k-space	52% k-space
T2-FSE	1(4 averages)	1	1	1	1
T2w series	5(1 average)	0.9	1.4	1.8	2.6
T1w series	20(1 average)	3.6	5.4	7.2	10.4
T2*w series	8(2 averages)	1.4	2.2	2.8	4.2
Total Time	34	7	10	13	18

The PDFF and PDwF maps computed from under sampled T2*w data were physiologically reasonable and compared well with corresponding GT maps. Computed from both reconstructed and GT T2*w images, the R_{2f}^* and R_{2w}^* of adipose tissue were lower than the corresponding values in the fluid tissue type; this was somewhat unexpected and may be attributable to potentially higher susceptibility effects in the fluid tissue type arising from endogenous sources such as iron. More concerning is the underestimation of R_{2f}^* and R_{2w}^* for different undersampling rates compared to fully sampled data, which may be due to cumulative errors during reconstruction introduced by undersampling, or fitting errors generated from the fat and water estimation framework [21]; and these errors propagated to the tissue type definitions.

Chapter 4: Radiation Therapy

4.1 Basics of Radiotherapy Treatment

Radiotherapy is an important treatment technique for palliative or curative management of cancer in addition to surgery, chemotherapy, immunotherapy and others. In the case of radiotherapy, controlled ionizing radiation, X-ray or photon, is focused on the tumor cells to damage the DNA of cancer cells [114][53]. Proton therapy uses proton beams and has advantages of controlled depth deposition with a finite range. However, photon therapy is the most common and delivered using techniques like Three-Dimensional Conformal Therapy (3D CRT), IMRT and VMAT. The success of radiotherapy depends on the precise deposition and gradation of the ionization onto the GTV, CTV and PTV region without affecting the OAR and other healthy tissues. To achieve the acceptable and deliverable dose plan, optimal machine parameters must be determined and this process is called as treatment planning [84]. The acceptable deliverable dose plan looks for the dose distributions that do not exceed define dose limit recommendations but must be sufficient enough to damage the DNA of the cancer cells [114]. This can be done in two ways: forward planning and inverse planning. In case of forward planning the beam parameters are fixed and correspondingly, the machine parameters are determined. This is a long iterative process [84][114].

A more viable solution is the inverse planning process which defines treatment planning as a constraint optimization problem defined using Equation 4.1.

$$\min_x f(x) \text{ subject to } g_1(x), g_2(x), \dots, g_n(x) \geq 0 \quad (4.1)$$

Here, the objective function is defined voxel wise where we constraint the radiation dose values received by each voxel based on their delimitations defined by GTV, CTV, PTV or OAR. There can be multiple optimal solutions to this objective function but the clinically viable plan is selected based on the experience of a treatment planner. Once the optimal plan and the machine parameters are determined, the radiotherapy can be delivered to the patient. The treatment therapy starts with the linear accelerator that generates high-energy electron beams. The photon beams are guided by a Multi-Leaf Collimator (MLC) and filters that project the desired shape on the tumor region [84][114]. It must be noted that the treatment planning process is a time-consuming iterative task and often the treatment delivery is spread over multiple sessions. This may change the delineations of GTV, CTV, PTV and OAR. Further it may be required to optimize the machine parameters on the fly and as a result, automated treatment planning methods are becoming more popular.

4.2 Knowledge Based Methods of Treatment Planning

Automated treatment planning methods have been developed since the 1980s to tackle the labor and time-intensive task of manual radiotherapy treatment planning [39]. In general, the KBP methods use the prior information from the clinically approved database to generate new plans [19]. KBP methods can be classified into atlas-based methods and model-based methods. Atlas-based methods find the closest match for the new patient from the existing reference treatment plans followed by the transfer of parameters used as a starting point to determine optimal plan for the new patients. The search for the atlas-based closest match can be further divided into direct and indirect methods. Direct methods look for similarities between the database and new patient using patterns like OARS, tumor location, dose constraints, beam geometry, etc. The closest matched features are then used to predict the dose parameters. The indirect method uses models to directly predict the dose parameter. Next, the closest match case to the predicted dose parameter is selected [39][88]. From the literature survey conducted by Ge et al. it may be deduced that direct methods are

widely used for treatment planning process compared to the indirect methods [39]. Model-based methods are more rigorous automated planning methods as they use the combination of data from database and mathematical models to determine the treatment parameters for a new case. Mathematical models like multi-linear, logistic regression, Support Vector Machines and K-Nearest neighbors define the relationship between the feature vector and model parameters. Some input features comprise PTV-OAR overlap, OAR distance to PTV, Overlap Volume Histogram (OVH), etc. First, the mathematical model is solved using the input feature to estimate the model parameters. When a new case is queried, the fitted model predicts the Dose Volume Histogram (DVH). Recently, with the progress in database integration, computer hardware and availability of large datasets, the domain of KBP is now migrating towards the deep neural network frameworks that will be explored more in the following section.

4.3 Neural Network-Based Radiotherapy Treatment Planning

KBP methods suffer from several disadvantages like identification of correct feature set in terms of anatomical delineation, limited feature set derived from contours resulting in missing inherent structure characteristics and 1D prediction of DVH lacking the spatial information [84][118]. In one of the studies for radiation-induced rectal bleeding it is deduced that the performance of the dose distribution not only depends on the volumetric information but also on the morphological aspects [12]. Therefore, neural network-based techniques like Convolutional Neural Network (CNN) which incorporates the spatial information for dose prediction may perform better. KBP based methods use machine learning models which use structured data for precise predictions. Compared to conventional machine learning model neural network architectures try to find out feature sets in high dimensions which are reliable for accurate dose map prediction [105]. Feature sets identified by the neural network architectures are better at handling inter-patient variability when compared to the hand-picked feature sets used in KBP [79]. In the literature, a standard workflow of a deep neural

network to predict the clinical dose distributions comprises of the multi-layer neural network. UNET [100] architecture is the most used neural network framework for dose map prediction. Further, delineations like OAR, GTV, PTV, CTV targets, other anatomical contours and beam configurations are widely used inputs [118][76][114]. The underlying framework of densely connected nodes extracts the complex latent features in addition to the simple handpicked contours. As a result, neural network architectures have an inherent advantage over the standard KBP methods. In addition to the standard 2D U-NET architecture, other variants like Hierarchically Densely Connected U-net (HD U-NET) offer advantages such as extraction of features in the interslice direction without incurring high computation cost of 3D U-net. [90]. ResNet [22] architectures have also been used to improve the dose map predictions. A Generative Adversarial Network with a feature extraction Dual Attention Module (DAM) which incorporates better internal semantic information has also been tried for dose map predictions [130].

Chapter 5: Generative Adversarial Networks

5.1 Introduction to Deep Neural Networks

Deep Neural networks are a subset of supervised machine learning models. They are comprised of numerous linear and nonlinear functional units called neurons. These neurons perform simple computations to learn the complex relationships between the input and output data. Training of the neural network is similar to the system identification method. The unknown “parameters” of the network are learned by computing the error functions. The unknown parameters are then tuned to the point that the minimum of the error function is reached. One of the important differences between neural networks and other machine learning models is feature extraction. While standard machine learning models use handpicked features, neural networks can determine unstructured features. This is very important for tasks like image segmentation, object localization and detection, image analysis, image classification, etc. A Fully Connected Network (FCN) is a neural network wherein every neuron in the given layer is connected to all the neurons in the next layer. They are very useful for analyzing and predicting 1-D data where spatial or time series information is unimportant.

Conversely, the Convolutional Neural Network (CNN) incorporates spatial information by using simple filters. They prevent the overfitting by using only neighborhood information called as receptive field. As a result, CNN has been very successful in image processing, analysis and synthesis tasks. Further, CNN has an important property of translational equivariance, under some conditions. Since all the input images share the same weight, CNNs can identify objects in each irrespective of their positions [49]. This property is very useful in image processing tasks where blurring or noise due to motion is challenging. An important requirement for training a deep neural network is large number of labeled datasets.

However, in the case of medical image processing availability of the labeled dataset is sparse. Generative Adversarial Networks are an important variant of neural networks which can synthesize realistic images. Due to this, they find their applications in vast medical image synthesis tasks [31]. The next two sections provide a mathematical introduction to GAN and its variant pix2pix GAN [54].

5.2 Basics of GAN

GANs are a variant of deep neural network models used to synthesize realistic images. The underlying mathematical idea is as follows: Determining the probability distribution μ from the underlying training data set $\mathcal{X} \subset \mathbb{R}^n$ is challenging since only a finite set of samples from the large data set can be drawn. As a result, it is impossible to know the exact distribution μ ; instead, an approximate distribution ν is determined that will generate samples similar to that in \mathcal{X} [119]. In the case of GAN, there are two neural networks generator and discriminator which are set in an adversarial setting. They are trained to reach the zero-sum Nash equilibrium. The generator is a neural network that aims to find the approximation of the distribution μ . The generator initially starts to draw samples from the probability distribution γ which is $N(0,1)$ and tries to find mapping function $G: \mathbb{R}^d \rightarrow \mathbb{R}^n$ such that if $z \in \mathbb{R}^d$ is drawn from distribution γ than $G(z)$ has a distribution μ . The sample predicted by the generator is critiqued by the discriminator network. It outputs a probability $D(x): \mathbb{R}^n \rightarrow [0, 1]$ for every sample x stating if the sample comes from the desired distribution. Initially, the generator is not good at predicting the samples from the desired distribution and hence it is easy for discriminator to determine that the sample is fake. But as the $\gamma \rightarrow \mu$, generator predicts more and more realistic samples and it becomes difficult for discriminator to tell the difference. Iteratively when these networks are tuned the improvement in one network (Generator) cannot be achieved without degrading the performance of another network (Discriminator). It is expected that when these two-players zero-sum minmax game reaches equilibrium the generator will produce complex photorealistic

tic images which discriminator cannot identify [87][43]. This can be mathematically defined by Equation 5.1.

$$\min_G \max_D V(D, G) := \min_G \max_D (\mathbb{E}_{x \sim \mu} [\log D(x)] + \mathbb{E}_{z \sim \gamma} [\log (1 - D(G(z)))])) \quad (5.1)$$

While the basic GAN can generate photorealistic images for a given training dataset, it has no control on the types of images that are generated. conditional GAN [86] is a variant of basic GAN that can map the complex relationship between the points in the latent space and the target space. Hence, conditional GAN is used for the targeted image generation using some conditions like class labels, image type, etc. The data sample x is augmented with some additional information y (class labels, image types) in both discriminator and generator. This can be represented using Equation 5.2.

$$\min_G \max_D V_c(D, G) := \min_G \max_D (\mathbb{E}_{x, y \sim \mu} [\log D(x, y)] + \mathbb{E}_{z, y \sim \gamma} [\log (1 - D(y, G(y, z)))])) \quad (5.2)$$

5.3 Pix2Pix GAN

Pix2Pix is a variant of GAN that translate images from the input domain to the target domain. In case of pix2pix GAN, in addition to the euclidean norm of the conditional GAN, an L1 loss function is added to preserve the fine details of the predicted images without blurring [54] and is defined by Equation 5.3.

$$\mathcal{L}_{L1}(G) = \mathbb{E}_{x, y, z} [\|x - G(y, z)\|_1] \quad (5.3)$$

Hence, the final objective function can be defined using Equation 5.4.

$$G^* = \arg \min_G \max_D V_c(D, G) + \lambda \mathcal{L}_{L1}(G) \quad (5.4)$$

Further, the generator of pix2pix network is a “U-Net” based architecture [100] with skip connections between layer i and layer $n - i$, where n is the total number of layers in the architecture. The GAN discriminator preserves the high frequencies in the generated images by restricting the discriminator loss computation using local image patches. The patch GAN discriminator thus penalizes structures at the scale of patches.

A pix2pix GAN framework is optimized iteratively so that when the generator network is trained, the discriminator network is held constant. Similarly, when the discriminator is being trained generator network is unchanged. Pix2pix framework is widely used for image-to-image translation tasks like converting aerial photos to maps, medical image translation, synthesizing MRI from CT [57], etc.

Chapter 6: Prediction of Optimal Radiation Therapy Dose Maps from the mpMRI

6.1 Relation between Radiation Dose Maps and mpMRI

As seen from the literature review, most of the work on dose map prediction has been done using the anatomical contours and structures as the input. Drawing delineations is time-intensive and need to be done by an expert. Further, as the therapy progresses, the drawn delineations may not hold true next time in the treatment process due to the anatomical changes. In this work, we want to determine the latent representations of the complex relations between pre-RT and post-RT MRI in response to radiation therapy. We hypothesize that pre-RT and post-RT T1w, T1w-CE, T2w, and FLAIR MRI, and particularly ADC maps, contain sufficient information to predict the radiosensitivity of BCMB lesions. We will characterize the voxelwise relationship between RT dose, pre-RT intensities on T1w, T1wCE, T2w, FLAIR, and ADC, and post-RT changes in intensities on these images. We call this a “forward model” that can predict the post-RT changes on mpMRI using the pre-RT mpMRI and the RT dose maps. This will enable the radiation oncologists to simulate the dose maps and determine their effects on post-RT MRI. We have also developed an “inverse model” to predict the optimal dose map from the pre-RT ADC and prescribed/desired post-RT ADC values. In this work, we demonstrate that the information contained in spatially co-registered pre-RT and post-RT MRI is sufficient to predict the delivered RT dose map and vice-versa. Both these models have been trained end-to-end without the need for manual contouring².

²This work is published in International Journal of Radiation Oncology.Biology.Physics [66]. Permission is included in Appendix B

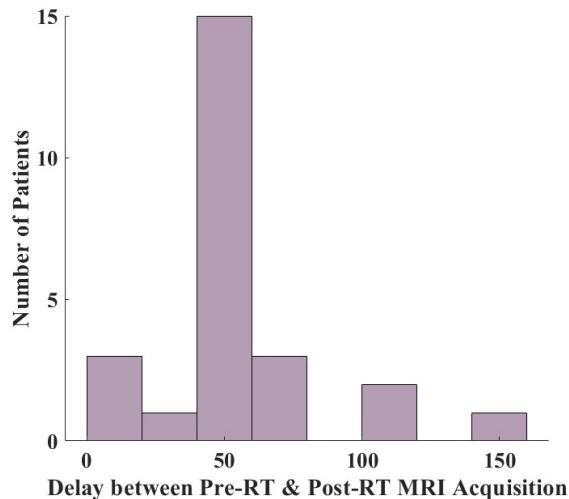


Figure 6.1: Histogram of Post-RT Acquisition Time Gap vs. Number of Subjects.

6.2 Data Preprocessing

In a retrospective IRB-approved study, planning CT images and associated RT dose maps, and T1w, T1wCE, T2w, FLAIR images, and ADC maps acquired at pre-RT, post-RT (15 to 158 days) and at tumor recurrence (54 to 831 days) in 24 BCMB subjects were curated from our Radiology and Radiation Oncology databases [85]. Figure 6.1 shows the histogram of the number of subjects against the delta time between pre-RT and post-RT mpMRI acquisitions. The dataset comprises recurring and responding lesions, 24 lesions. BCMB subjects received a mean SRS dose of 21 Gy, range: 15-30 Gy, in 1-5 fractions. The data preprocessing steps are summarized in the block diagram shown in Figure 6.3. mpMRI images from all scan dates were co-registered to the planning CT using MIRADA-RTx (Mirada Medical, Denver, CO, USA). GTV contours and the RT dose map associated with the planning CT could be applied to the mpMRI after co-registration. Voxel intensities were calibrated on T2w, FLAIR, T1w and T1wCE images using two reference normal tissues [108]. T1w and T1wCE were calibrated using the same ‘slope’ and ‘intercept’ calculated from the same subject and scan session. ADC and RT dose maps are not calibrated. Intensity-calibrated voxels on co-registered mpMRI were assigned to objectively defined tissue types [46]. All the images were cropped to size 256 x 256. End slices without any visible tissue

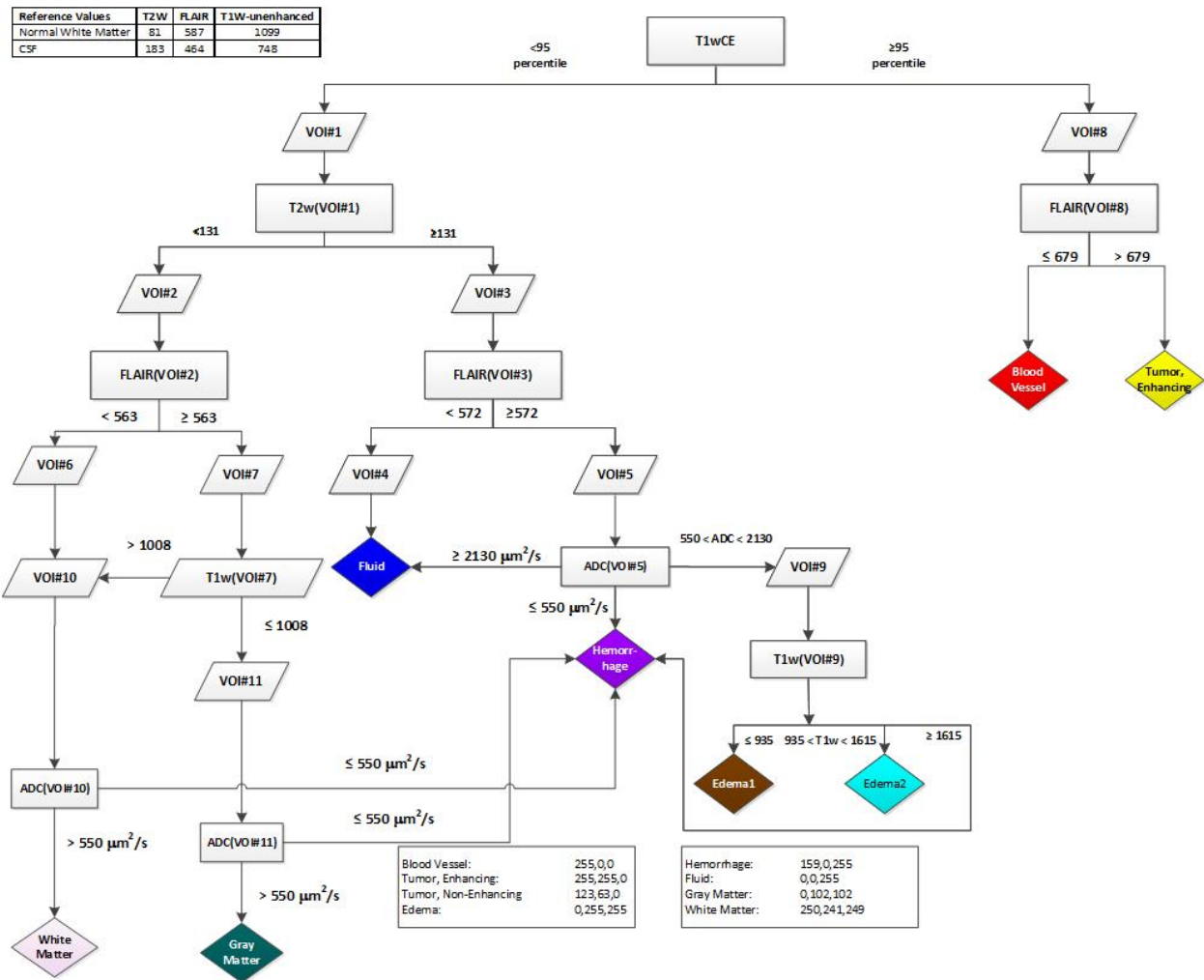


Figure 6.2: Quantitative Validation of Forward Model.

were removed from the dataset. Figure 6.4 shows the example slice from our data set. The first column shows planning CT, administered Dose map and the corresponding GTV. Rows 1,2 and 3 show the pre-RT mpMRI, post-RT mpMRI and mpMRI acquired at recurrence, respectively. Maps of objectively defined tissue types defined in Figure 6.2. The tissue type maps are computed from MRIs of an example subject provide visual confirmation of the utility of the intensity-calibration process (last column Figure 6.4).

Table 6.1: Mean and Standard Deviation Estimated from Training Data.

MRI Scan Type	Mean	Std	Subjects
ADC	1.13E+03	588	18
FLAIR	572	104	18
T2W	101	42	16
T1W and T1WCE	970	206	17
RT Dose Map	3.9	8.9	18

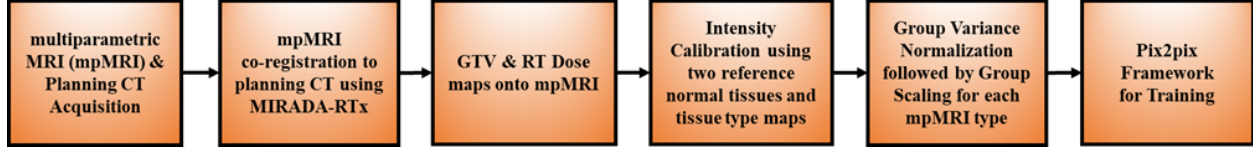


Figure 6.3: BCMB Data Preprocessing.

Variance normalization was done by calculating each scan type’s global mean and standard deviation, as defined by Equation 6.1.

$$variancenormalized_{MRIttype} = \frac{Image - mean_{MRIttype}}{std_{MRIttype}} \quad (6.1)$$

Each scan type’s global mean and standard deviation are shown in the Table 6.1. Mean and standard deviation were obtained from subjects with only spin-echo sequences; hence variable subject numbers can be observed for each scan type. From the histograms of variance-normalized intensities of all voxels within the brain mask pooled over all subjects and scan dates, we identified low and high thresholds, as seen in the Table 6.2. We then scaled the voxel values between -1 and +1 by using the Equations 6.2 and 6.3.

$$scaled_{MRIttype} = m_{MRIttype} \times (variancenormalized_{MRIttype}) + c_{MRIttype} \quad (6.2)$$

$$m_{MRIttype} = \frac{2}{H_{MRIttype} - L_{MRIttype}} \quad (6.3)$$

$$c_{MRIttype} = 1 - \frac{2 \times H_{MRIttype}}{H_{MRIttype} - L_{MRIttype}} \quad (6.4)$$

The global low and high thresholds used for scaling are tabulated in Table 6.2. We divided our dataset into training and test sets with 18 and 6 subjects. We then generated a simulated post-RT mpMRI for training. The simulated post-RT mpMRI for training the forward and inverse model was generated using the pre-RT and post-RT mpMRI. The range of the RT dose map in our data is 0-36 Gy. Correspondingly, we generated a sigmoidal function defined by $S = \frac{1}{1+\exp(-RT+13)}$ shown in Figure 6.5. We generated the post-RT simulated image by incorporating information from pre-RT and post-RT mpMRI using the Equation 6.5.

$$postRT_{targetMRI} = preRT_{MRItype} (1 - S(RT)) + postRT_{MRItype} \times S(RT) \quad (6.5)$$

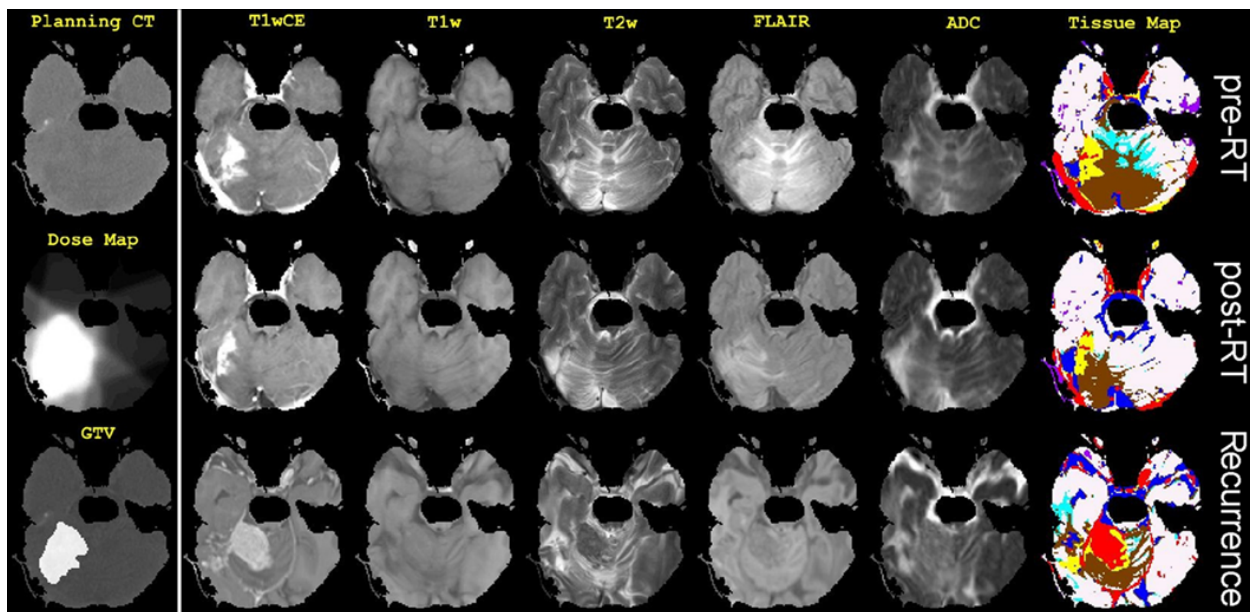


Figure 6.4: Example Slice from BCMB Dataset.

Intuitively the equation(6.5) states that for lower values of RT, the post-RT target must be the same as pre-RT MRI and for higher values of RT, the post-RT target will be equal to post-RT MRI. We generated the post-RT training MRI value for all the 5 MRI types, T1w, T1wCE, T2w, FLAIR and ADC, for training our forward and inverse models.

Table 6.2: Identified Global Low and High Threshold from Training Data.

MRI Scan Type	Low Threshold(L)	High Threshold(H)	Subjects
ADC	-1.93	4.02	18
FLAIR	-5.48	5.52	18
T2W	-2.41	3.9	16
T1W and T1WCE	-4.7	4.02	17
RT Dose Map	-0.44	4.01	18

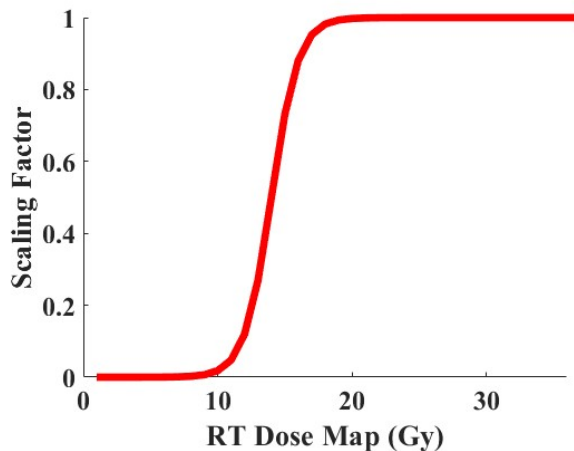


Figure 6.5: Scaling Factor Used for Generating the Training Images.

6.3 Preliminary Data Analysis

A preliminary data analysis was conducted to determine the relationship between the pre-RT and post-RT mpMRI when subjected to an RT dose map using 24 subjects. Within the RT dose maps, we computed the mean and standard deviation for differences between the pre-RT and post-RT mpMRI. Figure 6.6 shows the results of the changes between the post and pre-RT mpMRI as a function of the RT Dose map. Delta changes are apparent from the plots where RT values are greater than 20. To determine the characteristics of the responding and recurrent tumor, we computed volume change, post-RT - pre-RT mpMRI, within six different tissue types, namely fluid, GM, WM, hemorrhage, BV+CE and NE+Edema. We then determined the positive/negative sign change for 14 recurrent and 10 responding lesions, as shown in Figure 6.7. The total number of tumors with negative volume change in both recurrent and responding tumor type was higher in WM, Hemorrhage and NE+Edema. The

total number of tumors with positive volume change in responding tumor type was higher in BV+CE. However, no specific conclusions can be drawn for responding and recurrent tumor types using the tissue type maps with this limited dataset.

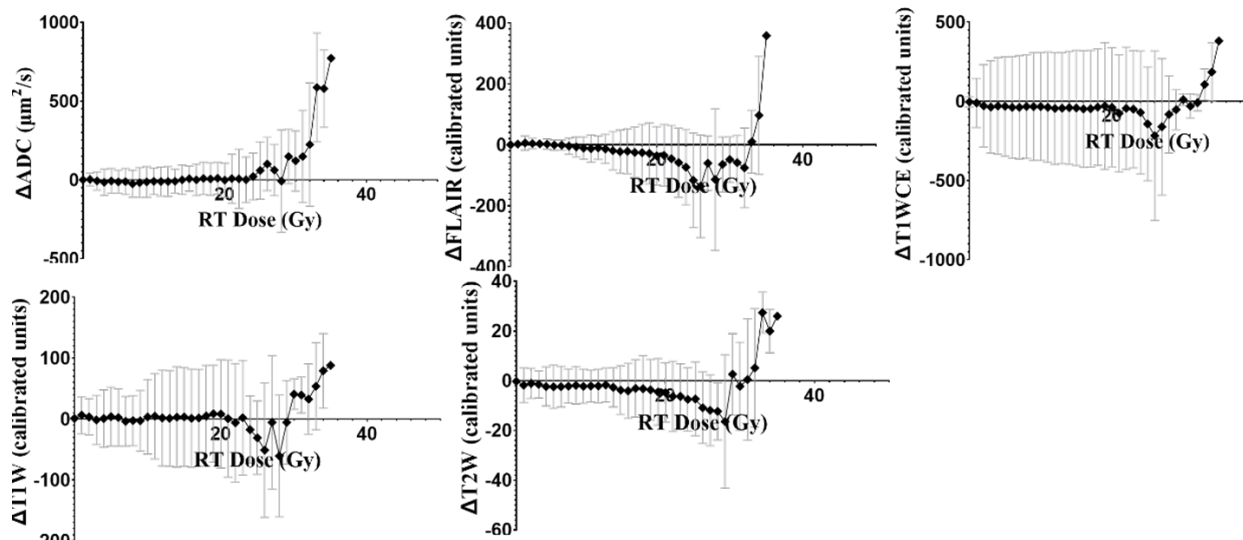


Figure 6.6: Delta Changes of mpMRI vs. RT Dose Plots.

6.4 Model Architecture

We use a variant of Pix2Pix architecture [54] for training the forward and inverse model shown in Figures 6.8 and 6.9, respectively. The main components of the architecture are the generator and discriminator, as discussed below.

6.4.1 Generator

The generator of our framework is a variant of the UNET architecture [100]. At its core, it is an encoder-decoder network with contracting and expanding pathways that can efficiently encode the latent representations of the data at the input channel. The skip connections of the network add the higher resolution feature maps from the encoder to enhance the learning process. The entire network can be formed using UNET up and UNET down blocks. The UNET up block has a convolution filter of size 4×4 , batch normalization,

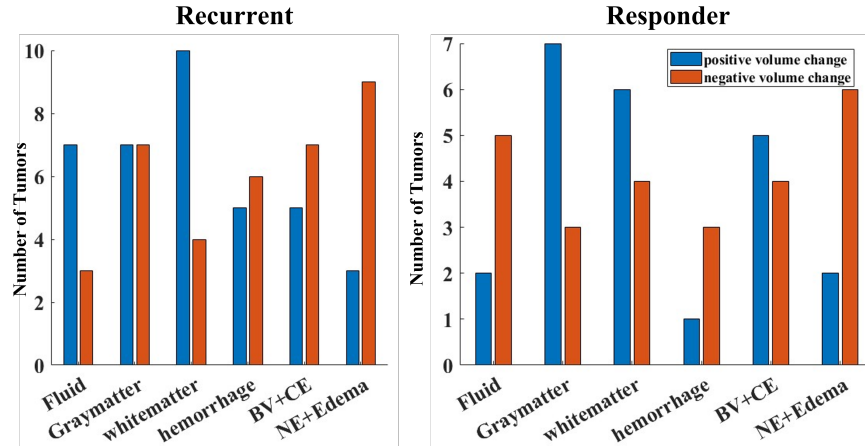


Figure 6.7: Tumor Volume Change for Recurrent and Responding Lesions.

except the first block and leaky ReLU. The UNET down block has a transposed convolution filter of size 4×4 , batch normalization, drop out layer and ReLU activation. The input to the generator is $C = 6$, pre-RT T1wCE, T1w, FLAIR, T2w, ADC and RT dose maps, shown in Figure 6.8 in the case of a forward model and $C = 2$, pre-RT and post-RT ADC, for the inverse model shown in Figure 6.9. Tanh activation was used at the output layer. A detailed architecture of the generator is attached in Appendix G.

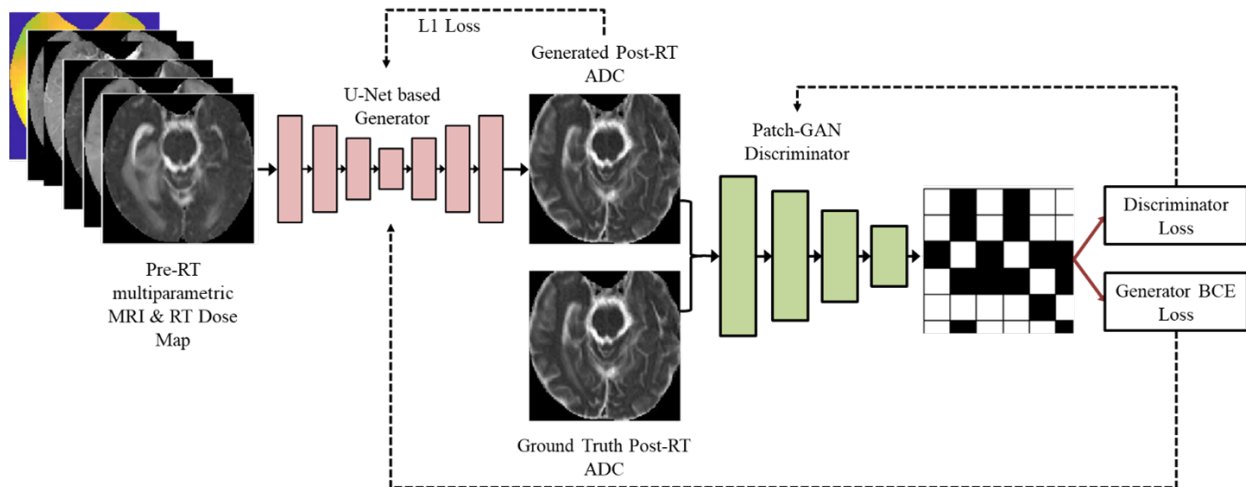


Figure 6.8: Proposed Forward Model.

6.4.2 Discriminator

The discriminator is a patchGAN discriminator, as described in [54]. A standard discriminator outputs only one value stating if the input image is real or fake. In the case of patch GAN, the output patch is of size 16 x 16 encompassing the local features. Our discriminator is a five-block module where each module has a convolution filter of size 4 x 4, Batch normalization and Leaky ReLU. The output layer is a sigmoidal activation layer. The input to the discriminator is an MRI image in the case of the forward model and RT dose maps in the case of the inverse model. The detailed architecture of the discriminator is attached in Appendix H.

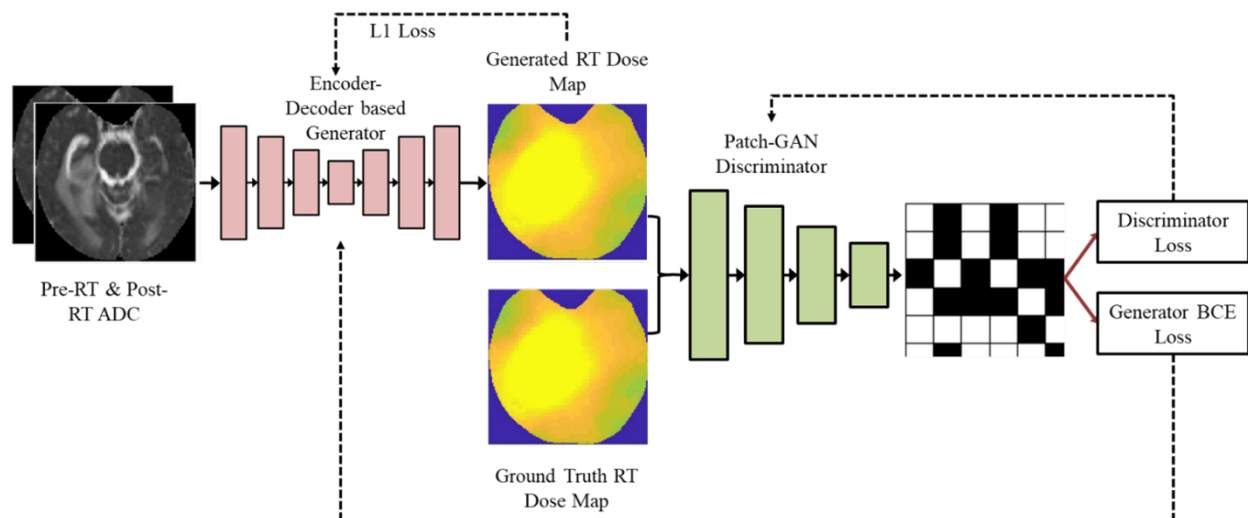


Figure 6.9: Proposed Inverse Model.

6.5 Training and Implementation

We trained both the discriminator and generator using ADAM optimizer [61]. The learning rate $\eta=0.0002$, $\beta_1=0.5$ and $\beta_2=0.999$. In case of generator BCE vs. L1 loss were weighted by a factor of 1:100 [54]. We added gaussian noise with zero mean and exponentially decaying std deviation to both real and fake input of discriminator. While experimenting, it was observed that the discriminator was overpowering the generator without adding noise. After noise imputation, the training between the discriminator and generator could be balanced.

For both the generator and discriminator we initialized weights from gaussian distribution with $\mu=0$, $\sigma=0.02$.

We trained our forward model with 5 pre-RT mpMRI and RT dose maps at the input against the post-RT target MRI. We run five forward models for target MRI T1wCE, T1w, T2w, FLAIR and ADC maps separately. Our inverse model was trained for pre-RT ADC maps and post-RT ADC maps at the input against the RT Dose maps. We determined the number of epochs for each forward model by calculating the correlation values between the ground truth and the predicted values. The number of epochs was then chosen by identifying the breakpoint where the correlation improvements became stagnant. Figure 6.10 shows the examples of the correlation vs. the number of iteration plots computed for T1wCE and FLAIR training data. We alternate a single gradient descent step between the discriminator and the generator for each epoch. The implementation of our algorithm is performed using Python 3.9 and we implemented the Pix2Pix architecture in TensorFlow 2.0. Our hardware is comprised of i7 CPU with 128 GB RAM and Geforce-GTX1660 SUPER 6GB RAM GPU.

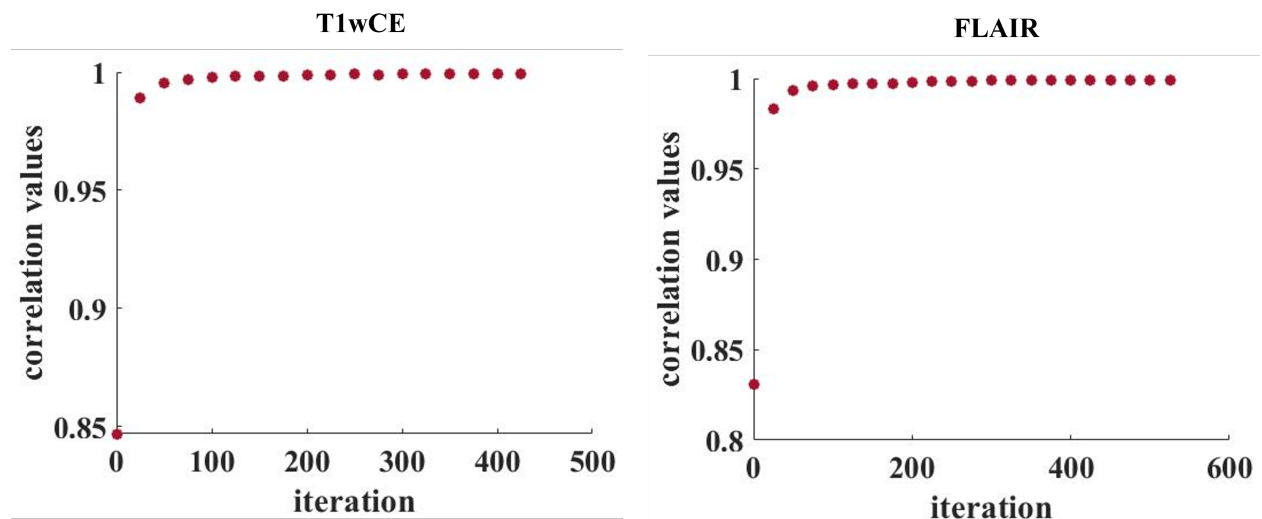


Figure 6.10: Iteration vs. Correlation Values for Training Data.

6.6 Validation Framework

6.6.1 Forward Model

A qualitative and quantitative validation is performed on six test subjects. The trained forward models are tested using six test subjects to predict post-RT ADC, FLAIR, T1wCE, T1w and T2w images. Histograms of the Post-RT and the Predicted Post-RT ADC, FLAIR, T1wCE, T1w and T2w values within the Brain Mask and GTV are computed. The tissue type maps like Blood Vessel, Enhancing Tumor, Fluid, Non-Enhancing Tumor, Edema, Gray Matter, White Matter and Hemorrhage are estimated from pre-RT, post-RT and predicted-post-RT mpMRI using the algorithm shown in Figure 6.2 [108]. Next, the percentage volume of tissue type maps is computed for pre-RT, post-RT and predicted-post-RT mpMRI. As discussed in section 1.1, ADC maps contain information mechanistically relatable to voxel-level tumor response to the therapies [36][1]. Hence, to validate our forward model for boundary conditions, expected values, we used ADC maps. We simulated the RT dose map values by increasing the RT values within the GTV of the brain mask. The simulated RT dose map and the pre-RT mpMRI were then used to predict the post-RT ADC values. We then compared the histograms of the predicted-post-RT ADC values for increasing RT Dose Map values within the GTV.

6.6.2 Inverse Model

The trained inverse model to predict the RT-Dose Map from pre-RT and post-RT ADC is also tested using six test subjects. We simulated the desired post-RT ADC map by using the pre-RT ADC map. We prescribed the desired ADC values within the GTV of pre-RT ADC, leaving the values outside the GTV unchanged. We then used the pre-RT ADC map and the desired post-RT ADC as input to the inverse model to predict the RT Dose Map. Finally, we compared the histograms of the predicted RT dose maps resulting from the increasing simulated ADC values.

6.7 Results

Figures 6.11 and 6.12 show the histogram of the actual and predicted post-RT T2w, FLAIR, T1w, T1wCE and ADC values, whole brain, obtained from 18 training and six test subjects, respectively. The training plots show that the forward model has effectively learned the probability distribution from the training data and the predicted histograms are contained within the standard deviation of the actual post-RT training data. The test histograms for the predicted values look similar to the actual values except for T1wCE data. This may be due to the T1wCE acquisition scheme which comprises of GRE and spin echo sequence. T1wCE sequences of our training data were mostly acquired using the spin echo technique. However, 50% of T1wCE sequences of the test data were acquired using the GRE pulse sequence.

Figure 6.13 shows the result of the forward model. Post-RT ADC map is predicted using pre-RT mpMRI (only pre-RT ADC is shown) and the delivered dose maps as the input to the forward model. The overall predicted post-RT ADC map looks similar to actual post-RT ADC maps. However, it can be observed that predicted post-RT ADC values within the treated GTV are underestimated compared to actual post-RT ADC. This can also be verified from the histograms of the predicted and actual post-RT ADC values within the GTV obtained from the six test subjects shown in Figure 6.14. Overall, the histograms of all predicted post-RT mpMRI for test data are underestimated for higher values and overestimated for lower values compared to the actual post-RT mpMRI. Figure 6.15. shows the comparison of the histogram of predicted post-RT mpMRI and actual post-RT mpMRI within the GTV from the 18 Training subjects. The predicted post-RT histograms within the GTV of all image types closely resemble that calculated from the actual data.

Figure 6.16 compares the tissue type maps computed from pre-RT, post-RT and predicted post-RT mpMRI for two different slices obtained from two subjects. Colors red, yellow, blue, brown, cyan, green, white and magenta signify Blood Volume (BV), Contrast Enhancing (CE) tumor, fluid, Non-Enhancing (NE) Tumor, edema, Gray Matter (GM), White Matter

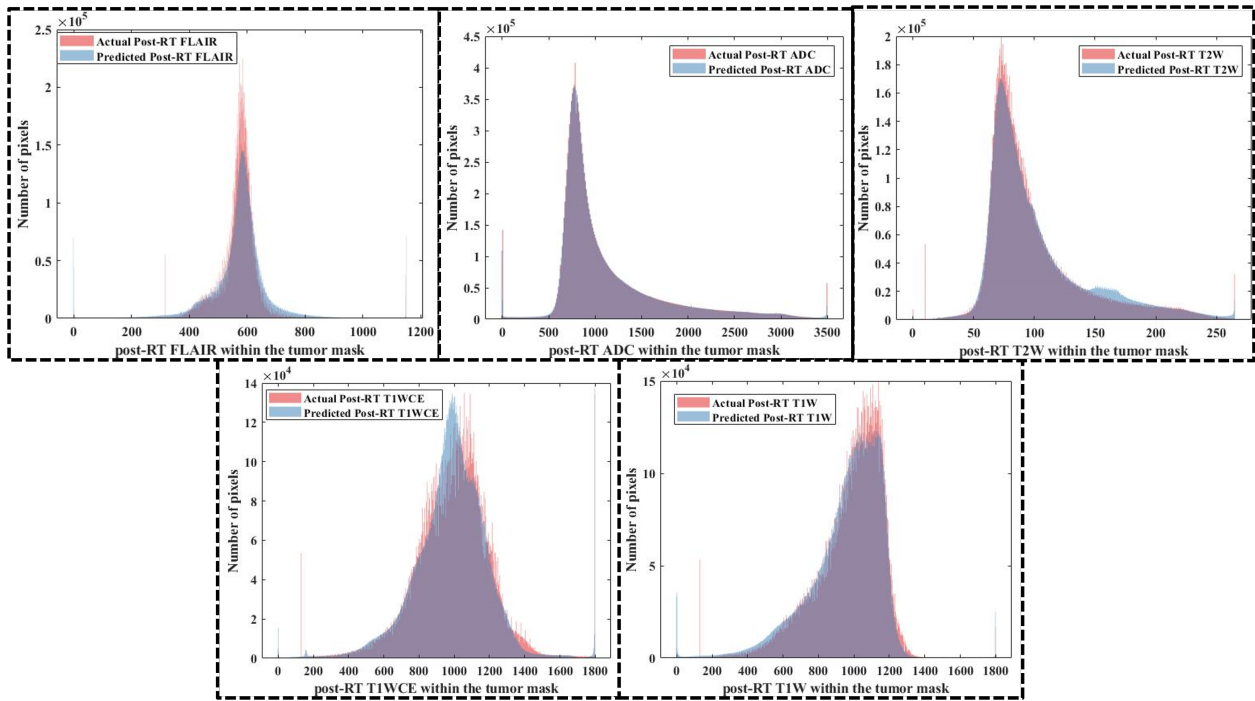


Figure 6.11: Predicted Histograms within the Brain Mask for Training Subjects.

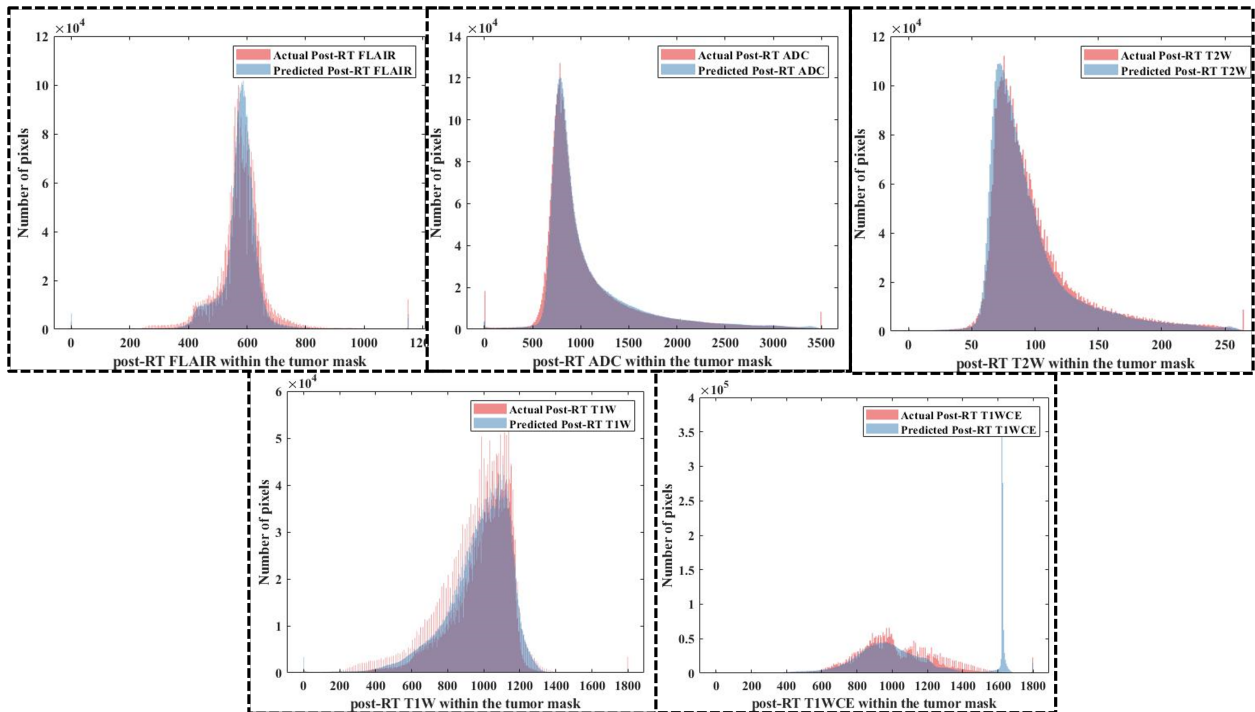


Figure 6.12: Predicted Histograms within the Brain Mask for Test Subjects.

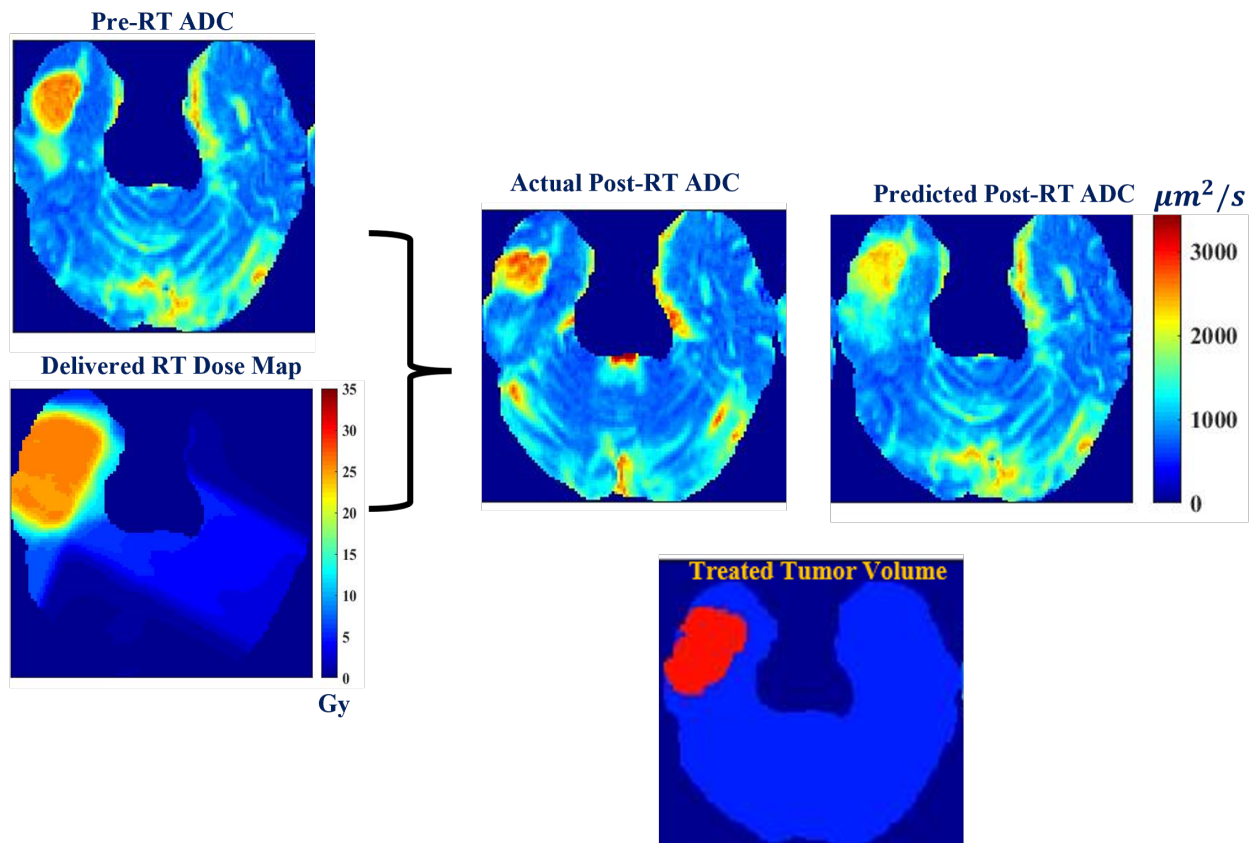


Figure 6.13: Results of the Forward Model.

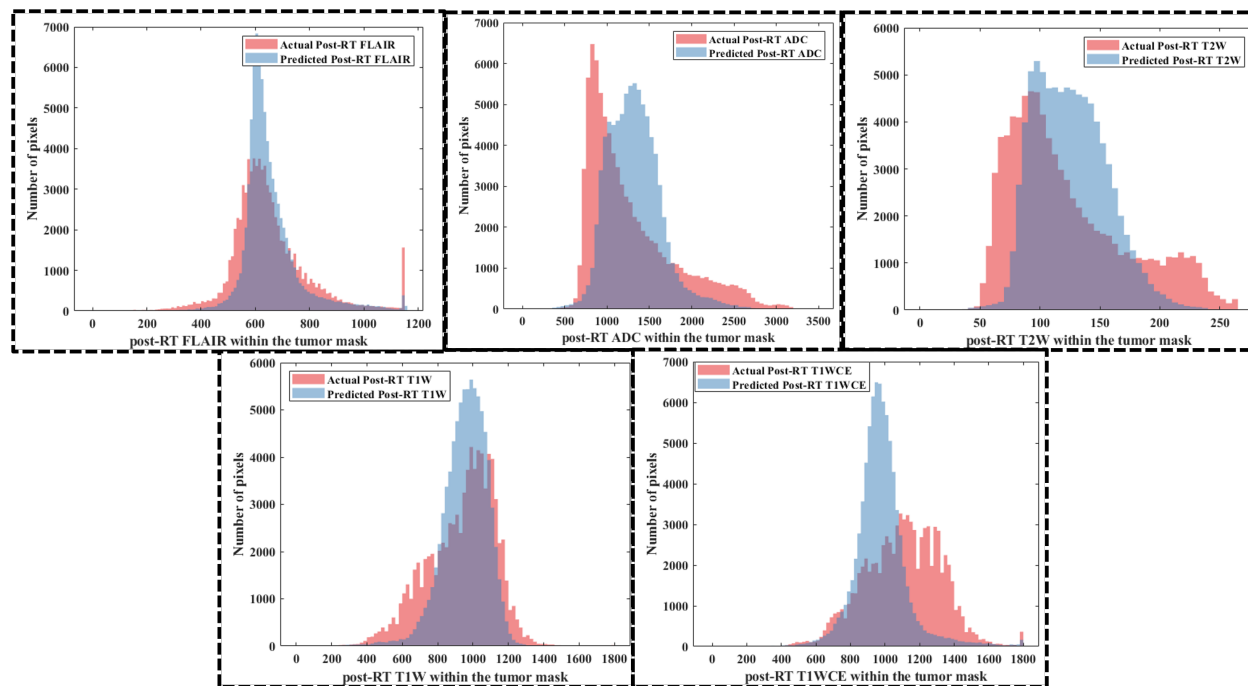


Figure 6.14: Predicted Histograms within the GTV for Test Subjects.

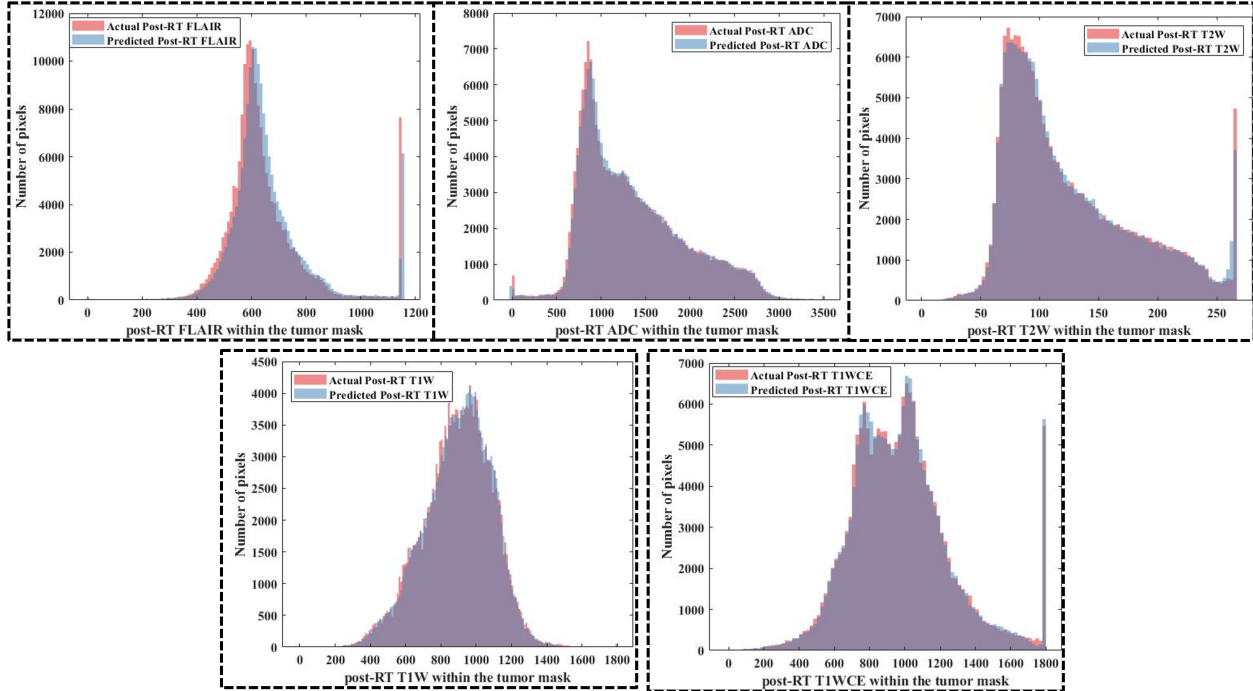


Figure 6.15: Predicted Histograms within the GTV for Training Subjects.

(WM) and hemorrhage respectively. Overall, the tissue type maps of the predicted post-RT and actual post-RT for both the slices (top and bottom row) look similar. Most of the pixels within the tumor GTV of predicted post-RT are identified as a fluid that agrees with the actual post-RT. However, the combinations of pixels at the boundary of the GTV signifying CE, edema and NE are classified as NE tumors. For subject 6 (bottom row), the NE tumor within the GTV of predicted ADC post-RT is consistent with the actual post-RT. Next, the percentage volume of tissue types like fluid, GM, WM, hemorrhage, BV+CE (BV and CE combined), NE+Edema (NE and Edema combined) from pre-RT, post-RT and predicted post-RT mpMRI are computed and shown in Figure 6.17. As expected, the BV+CE volume has shrunk for post-RT mpMRI compared to pre-RT mpMRI. The computed BV+CE volumes for predicted post-RT are close to the actual post-RT volumes. However, for subjects 1 and 3, the BV+CE volumes are underestimated, and for subject 4, it is overestimated. Further, the NE+Edema tissue type for the predicted post-RT is mostly

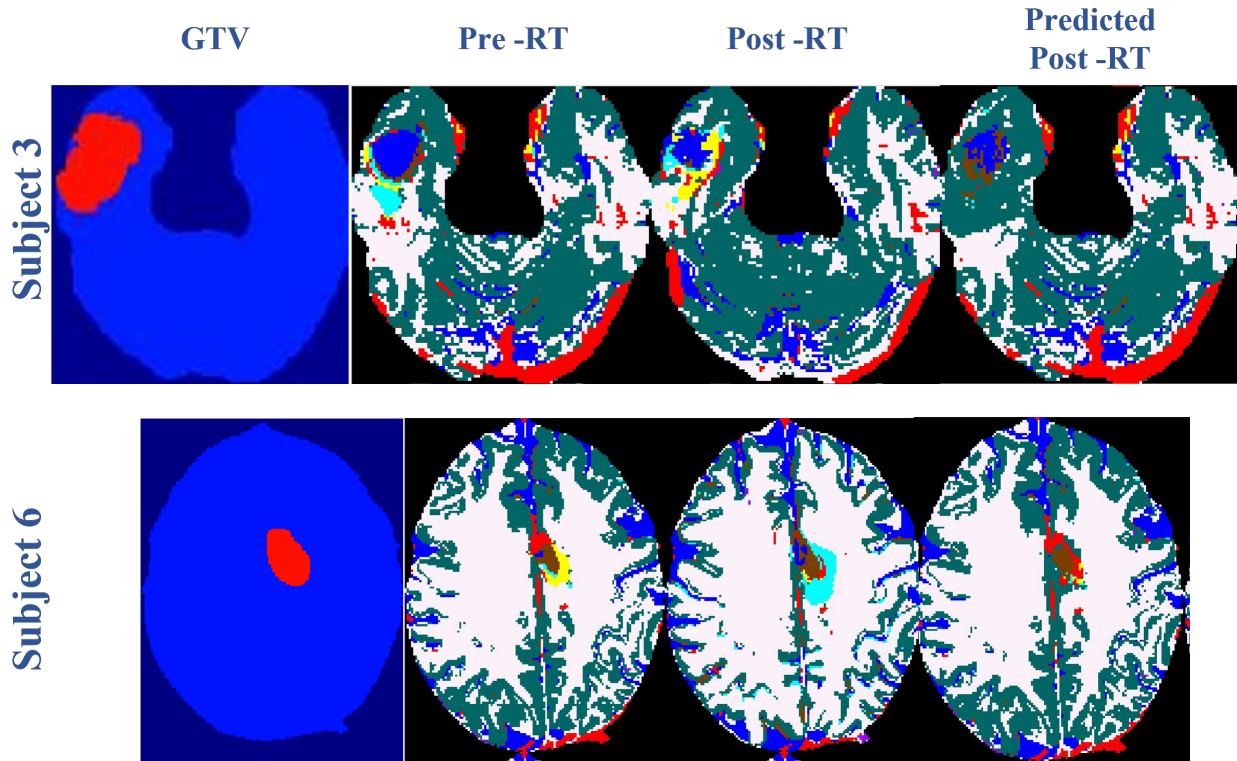


Figure 6.16: Tissue Type Maps Computed from Forward Model.

underestimated. The computation of the % volume for the training data is shown in Figure 6.18, 6.19, and 6.20.

Figure 6.21 shows the simulated results of the forward model for two slices from two different subjects. The first row shows the GTV and actual pre-RT and post-RT ADC maps. The next two rows show the simulated post-RT ADC maps resulting from an increase in the RT values within the GTV at the input of the forward model. As the RT dose map values increase within the GTV, the predicted post-RT ADC values within the GTV also increase. This agrees with the expected values of ADC, which increase in response to the RT due to cell death increasing extracellular space. This can also be verified from the histograms of predicted post-RT ADC values within the GTV shown in Figure 6.22. As expected, as the amount of RT dose map increases, the histogram of the predicted post-RT ADC values shifts to the right.

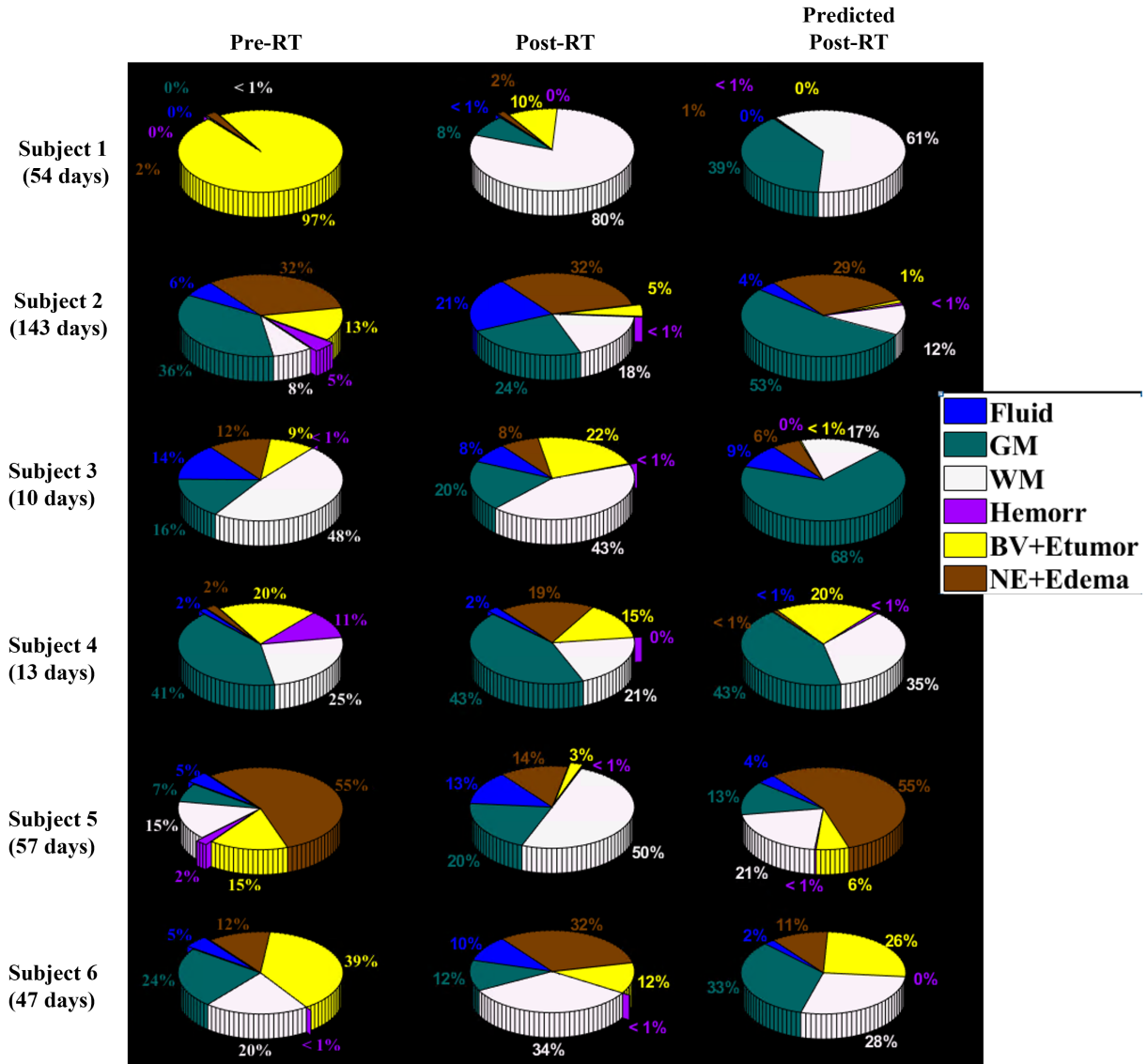


Figure 6.17: Quantitative Validation of Forward Model for Six Test Subjects.

Finally, Figure 6.23 shows the inverse model results for two slices from two subjects. As seen in the Figure 6.23 (left), the input to the inverse model is a pre-RT ADC map and prescribed post-RT ADC maps with increasing ADC values within the GTV. The output of the inverse models is the RT dose map. As the Figure 6.23 (right) shows, the predicted dose maps increase as the prescribed ADC values within the GTV increase. This means that the RT dose map values must be high to generate high ADC values. This can also be verified from the histogram of the predicted RT dose map values within the GTV shown in Figure

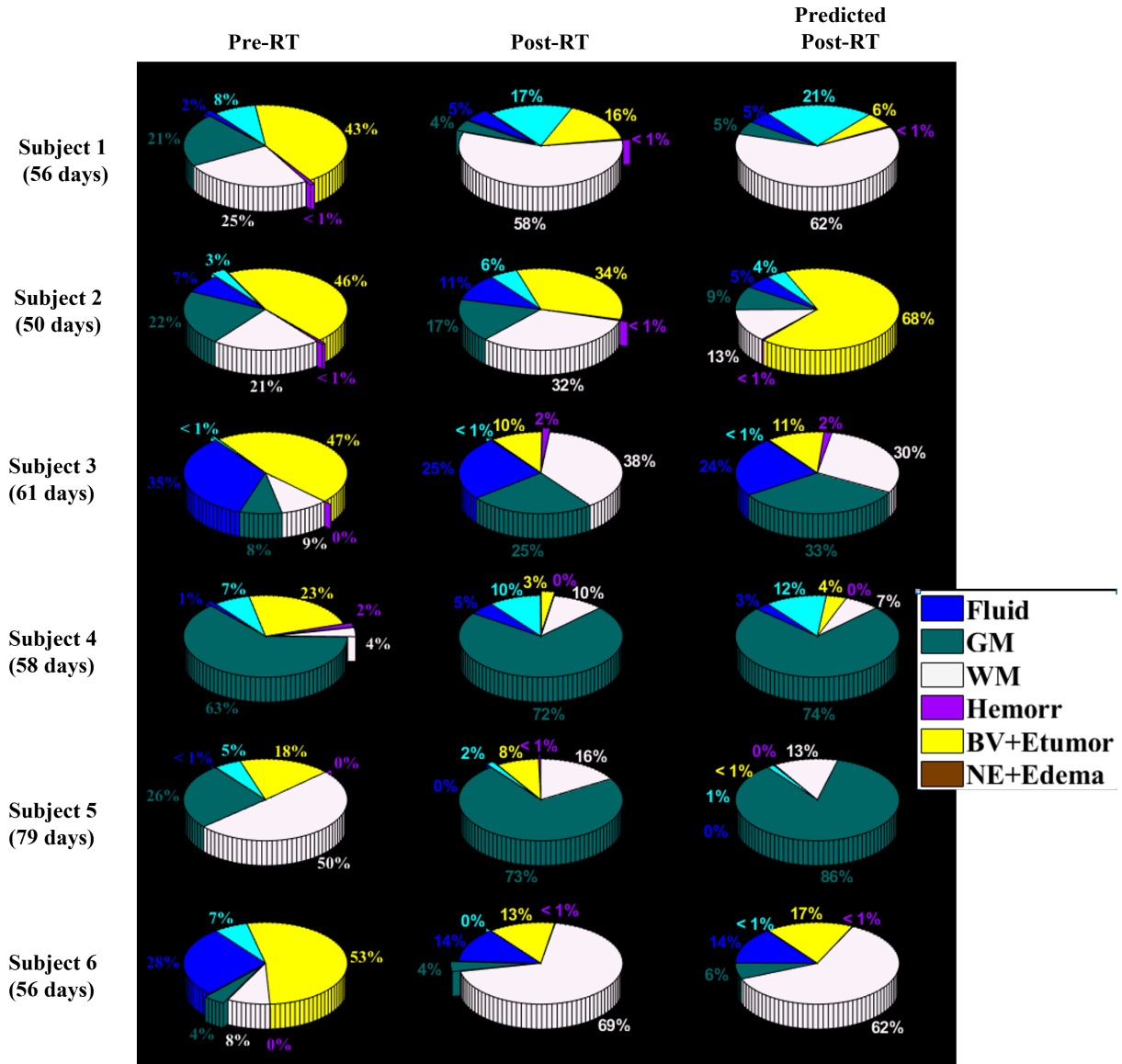


Figure 6.18: Quantitative Validation of Forward Model for 1-6 Training Subjects.

6.24. As the ADC values increases within the GTV, the histograms of the predicted RT dose maps shift towards the right.

6.8 Discussions

Our objective for this preliminary work is twofold. Firstly, we demonstrate the voxelwise relationship between the RT Dose and pre-RT mpMRI intensities to predict the changes in intensities on the post-RT mpMRI using the forward model. Next, using the inverse model,

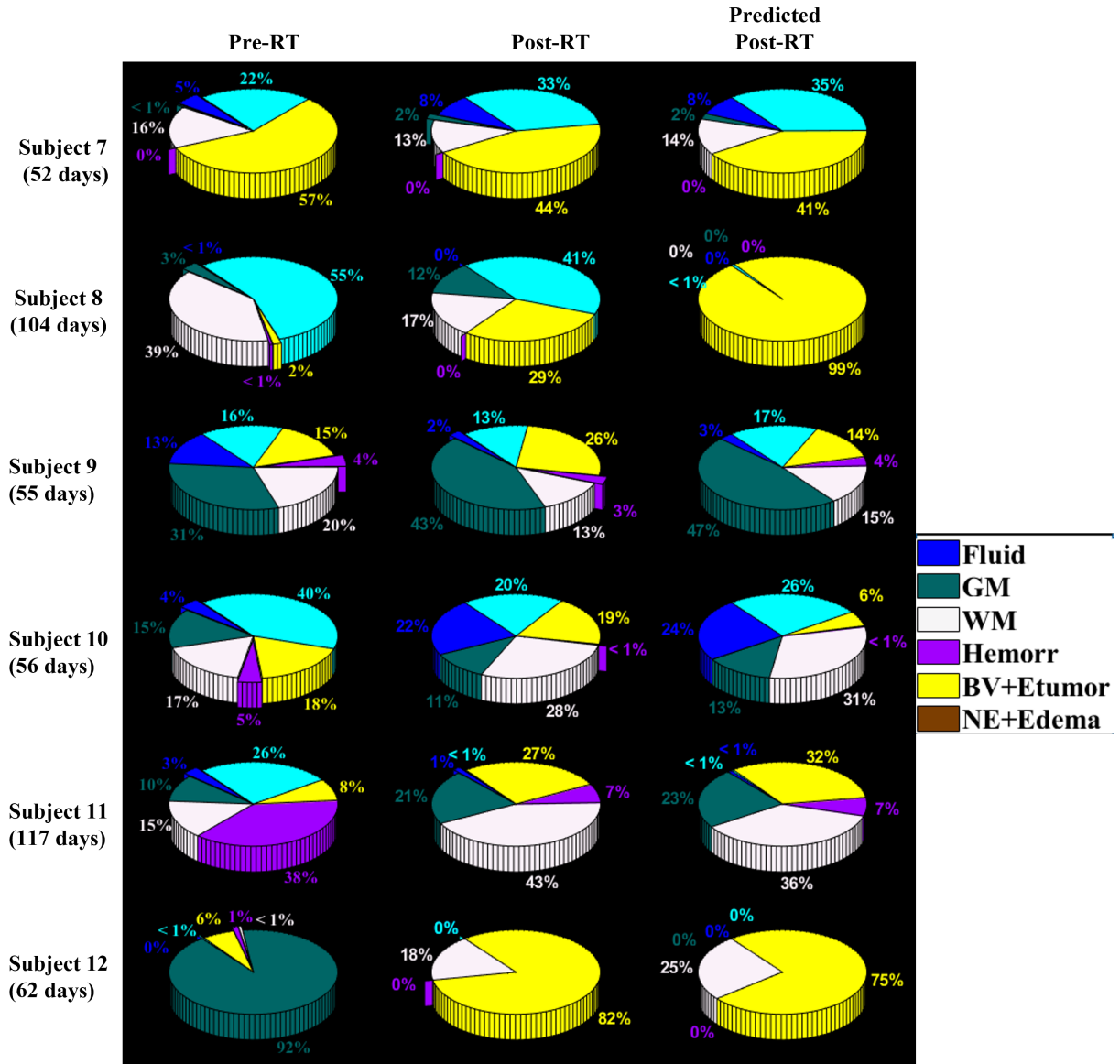


Figure 6.19: Quantitative Validation of Forward Model for 7-12 Training Subjects.

we also predict the RT dose map for producing prescribed changes on the post-RT ADC. Overall, the results of the predicted post-RT mpMRI from the forward model resemble those computed from the actual post-RT mpMRI. However, the distribution of the intensities within the GTV of predicted-post RT mpMRI have lower standard deviations compared to the actual for all mpMRI types, which is also evident from the histograms of the predicted post-RT mpMRI. There may be multiple reasons which resulted in underestimations of the predicted values. Firstly, our preliminary data analysis suggested that the apparent changes

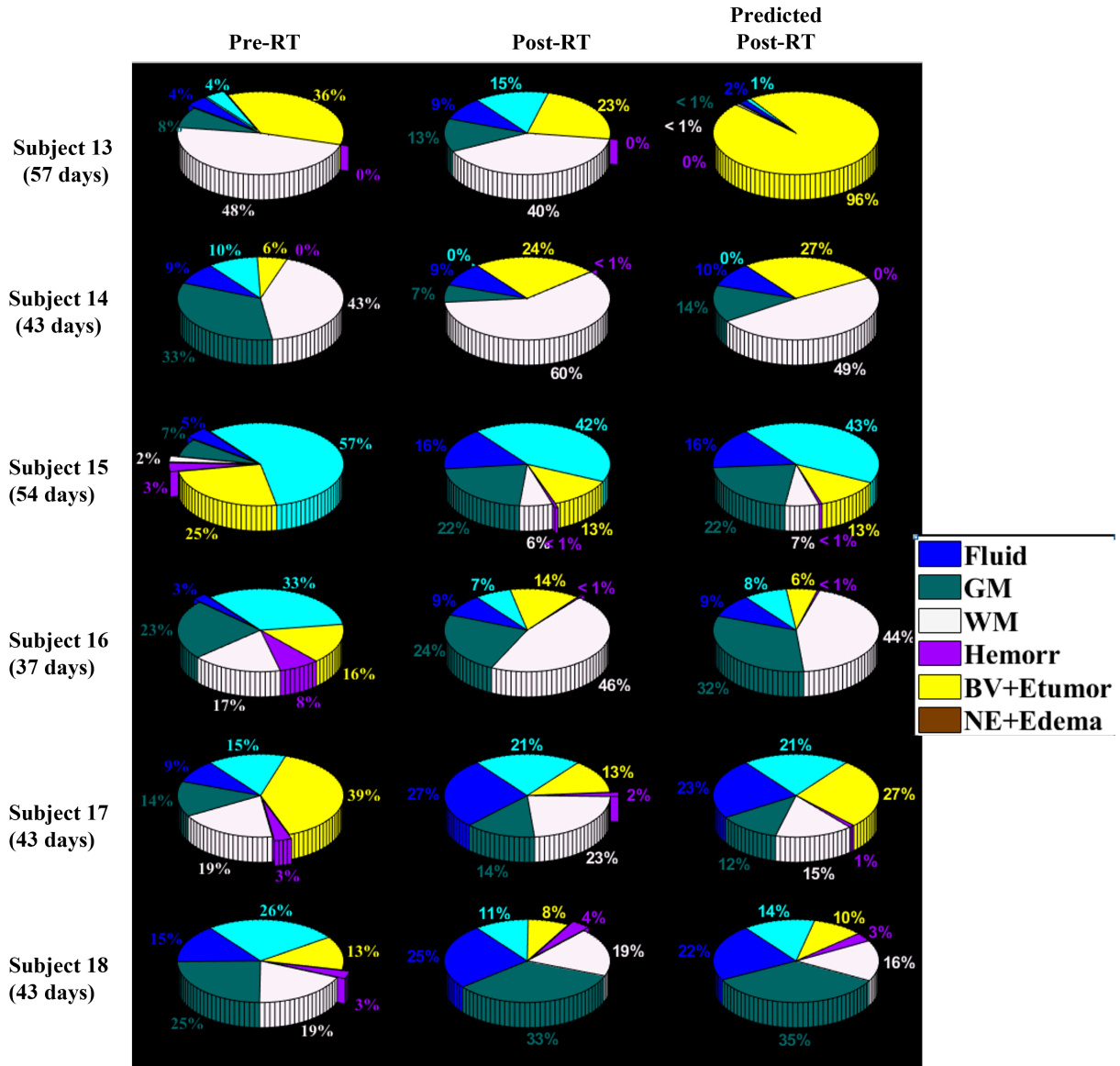


Figure 6.20: Quantitative Validation of Forward Model for 13-18 Training Subjects.

between pre and post-mpMRI occur for high RT values, especially for $RT > 20$. Further, the number of voxels that received the $RT \geq 10$, i.e., had tumor contours was hardly 0.1% of all the voxels in the 24 BCMB subject. Also, the time between the acquisition of pre- and post-RT mpMRI is variable, ranging from 15 to 158 days. As discussed in the introduction, ADC intensities are very sensitive to the time of acquisition after the RT, which may have affected the ADC values in the considered dataset. Qualitatively, the predicted post-RT tissue type maps closely resemble those estimated from the actual post-RT dose map. Some

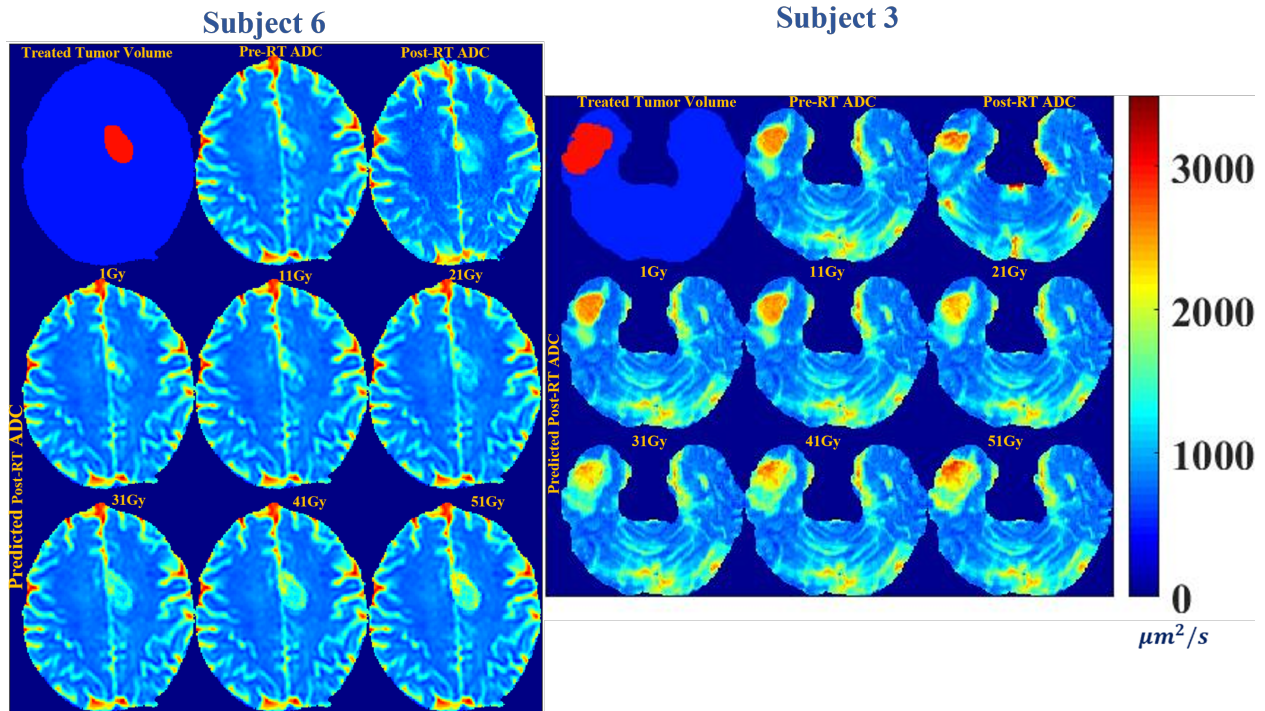


Figure 6.21: Simulated Predictions of Forward Model.

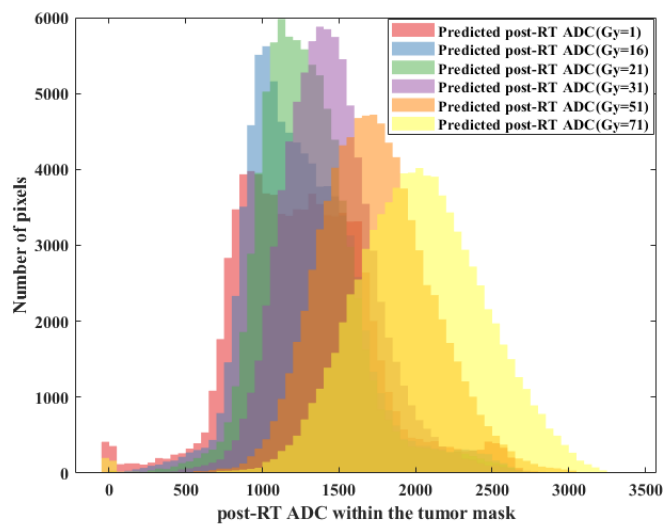


Figure 6.22: Simulated Predicted Histograms from the Forward Model.

loss of fidelity for the predicted post-RT tissue type maps vis-à-vis the corresponding GT maps in the GTV is apparent. This may be due to cumulative errors introduced by five predicted post-RT MRIs and the rules for estimating the tissue type maps. An alternate approach to tackle these limitations will be to use the GAN techniques like multimodal GAN,

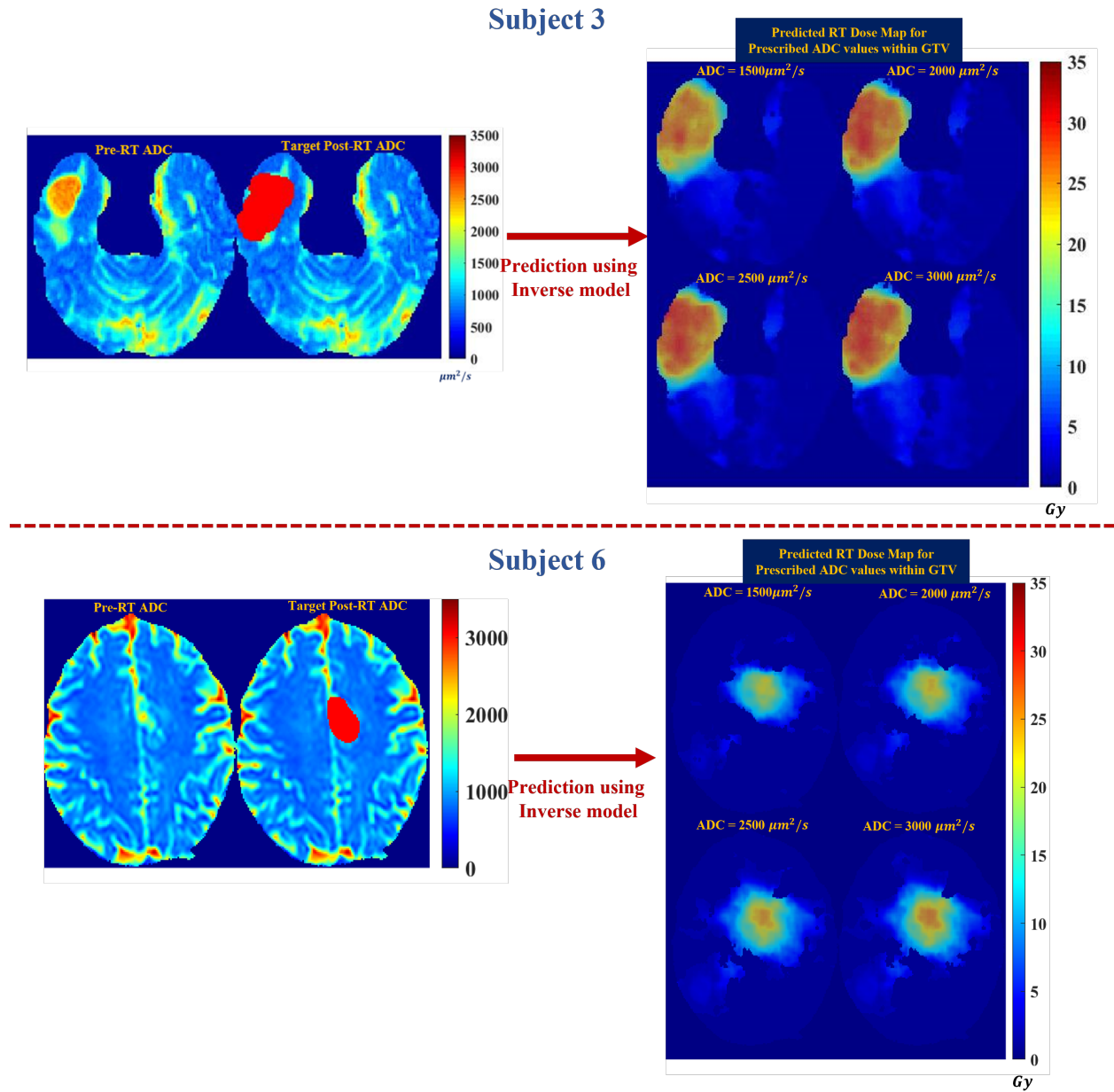


Figure 6.23: Simulated Predictions of the Inverse Model.

which can synthesize all five post-RT MRI sequences using one neural network architecture [102]. Further, to handle the problem of an unbalanced dataset where in our case, only 0.1% of data received high radiation values, the forward model could be improved by penalizing the GAN loss for the minority class.

The simulated results of the proposed forward model meet the boundary conditions, i.e., the expected changes on the ADC when administering the high RT values. Similar condi-

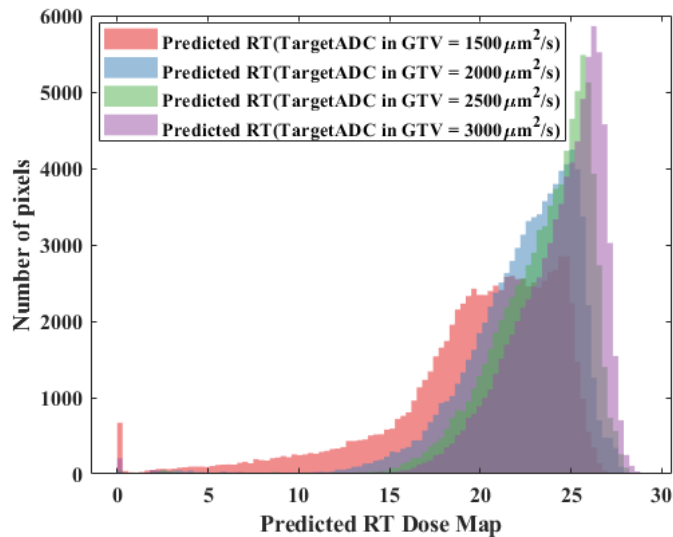


Figure 6.24: Simulated Predicted Histograms from the Inverse Model.

tions could be checked for other MRI types, given that enough data is available to identify the voxel-wise RT sensitivity for other MRI types. Further, they would provide criteria for defining a favorable post-RT MRI appearance of the tumor. This information could then be used as an input to the inverse model to improve the prediction of RT dose maps. Further, these voxel-level parameters could inform an eco-evolutionary model to predict tumor dynamics. The simulated results of the proposed inverse model meet the expectations of requiring higher RT values to generate higher ADC values within the GTV. However, the improvement in the results may be obtained by training the model by incorporating all the five pre-RT and post-RT mpMRI types.

Chapter 7: Conclusions and Future Work

7.1 Conclusions

In this work, the two aspects of the MRgRT LINAC are discussed. First, accelerating the reconstruction of multiparametric MRI (mpMRI). Second, prediction of precise dose maps from the pre-radiation therapy mpMRI sequences without the need of manual contouring. With the proposed Joint Reconstruction Framework, we accelerated the reconstruction of T1w, T2w, and T2*w by approximately five fold for preclinical mice data. We developed a single algorithm that could reconstruct a series of complex images and their parameter maps. Further, the complex T2*w images were used to estimate the fat and water content and their relaxation rates. With our approach, we could identify the tissue type maps like adipose, fluid, muscle, and tumor with high accuracy using only 18% of the under-sampled k-space data. To alleviate the manual aspects of RT planning and generate the optimized RT dose maps necessary for local tumor control and decreased toxicity, forward and inverse models using a variant of pix2pix GAN neural networks were trained. It was possible to predict the post-RT mpMRI changes using pre-RT mpMRI and RT dose maps using the forward model. In agreement with the expectations, the forward model also predicted the increasing post-RT ADC values within the GTV with increasing simulated RT doses in the range of 1 to 51 Gy. With the inverse model, we determined that higher RT values are required to generate higher ADC values within the GTV. Finally, it is envisioned that the forward models will assist the radiation oncologist in initial RT dose plan optimization, while the inverse model may be useful for daily RT plan optimization.

7.2 Future Work

The current work uses preclinical and clinical data for demonstrating the acceleration of joint reconstruction mpMRI and the prediction of optimal dose maps, respectively. In future work, we want to test our model end to end. We want to use the accelerated data set to predict the optimal RT dose maps. The end-to-end framework could use the accelerated mpMRI dataset to identify the sub-segments of tumor i.e. habitats. The precise identification of the habitats can then be used to generate voxel level dose predictions which can better control the local tumor habitats.

In future work, we plan to improve the proposed joint reconstruction algorithm to directly estimate the R_{2f}^* and R_{2w}^* and their corresponding \mathcal{A} maps from the under sampled k-space data. In the proposed framework, we define $u^m = \mathcal{A}^{T1}(1 - e^{-\frac{im}{T1}})$, i.e., reconstructed images “u” must satisfy the relaxation model equation. The left side of our equation is complex since we defined u as a complex quantity. However, the right side of our equation is approximated as real, i.e. we defined A and T1 as real quantities. So, the complex u is approximated by the real A and T1 which may not be exact. Hence, in future work we can improve this approximation using a complex A. Our ultimate goal is to extend this approach to objectively define physiologically meaningful sub-segments of tumors i.e. habitats using undersampled data, for which we anticipate needing to include multiple additional rules based on R_{2w}^* , R_{2f}^* , PDFF, PDwF, ADC, and microvascular parameters calculated from DCE-MRI. In future work, we aim to extend this image reconstruction approach to ADC mapping as well. Since the acquisition of ADC maps is a time consuming, we anticipate developing a neural network-based framework which can use the undersampled DWI k-space data to estimate the ADC maps.

The deep learning framework implemented for the forward and inverse model uses a conventional data-driven approach wherein we used the training data to map the input distributions to the target distributions. In future work, we want to use the model-driven approach to improve our prediction. We know that the relation between the RT dose map and

the pre-RT mpMRI to predict post-RT mpMRI is a complex process. Further, mathematical and biological models have been used to model the interaction between the tumor cells and the tissue microenvironments [109]. If we can incorporate these model equations into the deep neural network, we might be able to improve our prediction results. This will also be useful in cases where the amount of labeled data is scarce. At present, we have trained our deep learning framework for BCMB tumor types. In future work, we may want to update our model to incorporate other tumor types. In future work, we want to collect more data and identify the voxelwise relationship between RT dose and pre-RT intensities on mpMRI in locally responding and recurrent lesions.

References

- [1] A Afaq, A Andreou, and DM Koh. Diffusion-weighted magnetic resonance imaging for tumour response assessment: why, when and how? *Cancer Imaging*, 10(1A):S179, 2010.
- [2] Andrew L Alexander, Jee Eun Lee, Mariana Lazar, and Aaron S Field. Diffusion tensor imaging of the brain. *Neurotherapeutics*, 4(3):316–329, 2007.
- [3] MRIquestions.com Allen D. Elster. Fat suppression methods, 2021.
- [4] MRIquestions.com Allen D. Elster. Trace dwi and adc map, 2021.
- [5] Christian E Anderson, Charlie Y Wang, Yuning Gu, Rebecca Darrah, Mark A Griswold, Xin Yu, and Chris A Flask. Regularly incremented phase encoding–mr fingerprinting (ripe-mrf) for enhanced motion artifact suppression in preclinical cartesian mr fingerprinting. *Magnetic resonance in medicine*, 79(4):2176–2182, 2018.
- [6] Christine Baudelet and Bernard Gallez. Effect of anesthesia on the signal intensity in tumors using bold-mri: comparison with flow measurements by laser doppler flowmetry and oxygen measurements by luminescence-based probes. *Magnetic resonance imaging*, 22(7):905–912, 2004.
- [7] Amir Beck and Marc Teboulle. Fast gradient-based algorithms for constrained total variation image denoising and deblurring problems. *IEEE transactions on image processing*, 18(11):2419–2434, 2009.

- [8] Thorsten A Bley, Oliver Wieben, Christopher J François, Jean H Brittain, and Scott B Reeder. Fat and water magnetic resonance imaging. *Journal of Magnetic Resonance Imaging*, 31(1):4–18, 2010.
- [9] Kai Tobias Block, Martin Uecker, and Jens Frahm. Model-based iterative reconstruction for radial fast spin-echo mri. *IEEE transactions on medical imaging*, 28(11):1759–1769, 2009.
- [10] Stephen Boyd, Neal Parikh, Eric Chu, Borja Peleato, Jonathan Eckstein, et al. Distributed optimization and statistical learning via the alternating direction method of multipliers. *Foundations and Trends® in Machine learning*, 3(1):1–122, 2011.
- [11] M Brett. Mutual information as an image matching metric, 2021.
- [12] Florian Buettner, Sarah L Gulliford, Steve Webb, and Mike Partridge. Using dose-surface maps to predict radiation-induced rectal bleeding: a neural network approach. *Physics in Medicine & Biology*, 54(17):5139, 2009.
- [13] Mark Bydder, Takeshi Yokoo, Gavin Hamilton, Michael S Middleton, Alyssa D Chavez, Jeffrey B Schwimmer, Joel E Lavine, and Claude B Sirlin. Relaxation effects in the quantification of fat using gradient echo imaging. *Magnetic resonance imaging*, 26(3):347–359, 2008.
- [14] Yue Cao. The promise of dynamic contrast-enhanced imaging in radiation therapy. In *Seminars in radiation oncology*, volume 21, pages 147–156. Elsevier, 2011.
- [15] Yue Cao, Chia-Lin Tseng, James M Balter, Feifei Teng, Hemant A Parmar, and Arjun Sahgal. Mr-guided radiation therapy: transformative technology and its role in the central nervous system. *Neuro-oncology*, 19(suppl_2):ii16–ii29, 2017.

- [16] Richard AD Carano, Adrienne L Ross, Jed Ross, Simon P Williams, Hartmut Koeppen, Ralph H Schwall, and Nicholas Van Bruggen. Quantification of tumor tissue populations by multispectral analysis. *Magnetic Resonance in Medicine: An Official Journal of the International Society for Magnetic Resonance in Medicine*, 51(3):542–551, 2004.
- [17] Memorial Sloan Kettering Cancer Center. Image-guided radiation therapy, 2021.
- [18] Hersh Chandarana, Hesheng Wang, RHN Tijssen, and Indra J Das. Emerging role of mri in radiation therapy. *Journal of Magnetic Resonance Imaging*, 48(6):1468–1478, 2018.
- [19] Vorakarn Chanyavanich, Shiva K Das, William R Lee, and Joseph Y Lo. Knowledge-based imrt treatment planning for prostate cancer. *Medical physics*, 38(5):2515–2522, 2011.
- [20] Itthi Chatnuntaweck, Berkin Bilgic, Adrian Martin, Kawin Setsompop, and Elfar Adalsteinsson. Fast reconstruction for accelerated multi-slice multi-contrast mri. In *2015 IEEE 12th International Symposium on Biomedical Imaging (ISBI)*, pages 335–338. IEEE, 2015.
- [21] Venkata V Chebrolu, Catherine DG Hines, Huanzhou Yu, Angel R Pineda, Ann Shimakawa, Charles A McKenzie, Alexey Samsonov, Jean H Brittain, and Scott B Reeder. Independent estimation of t^* for water and fat for improved accuracy of fat quantification. *Magnetic Resonance in Medicine: An Official Journal of the International Society for Magnetic Resonance in Medicine*, 63(4):849–857, 2010.
- [22] Xinyuan Chen, Kuo Men, Yexiong Li, Junlin Yi, and Jianrong Dai. A feasibility study on an automated method to generate patient-specific dose distributions for radiotherapy using deep learning. *Medical physics*, 46(1):56–64, 2019.
- [23] Yunmei Chen, Ruogu Fang, and Xiaojing Ye. Joint image edge reconstruction and its application in multi-contrast mri. *arXiv preprint arXiv:1712.02000*, 2017.

- [24] Stefanie Corradini, Filippo Alongi, Nicolaus Andratschke, C Belka, L Boldrini, F Cellini, J Debus, M Guckenberger, J Hörner-Rieber, FJ Lagerwaard, et al. Mr-guidance in clinical reality: current treatment challenges and future perspectives. *Radiation Oncology*, 14(1):1–12, 2019.
- [25] J Delpiano. Fast mutual information of two images or signals, 2021.
- [26] Chengzhi Deng, Shengqian Wang, Wei Tian, Zhaoming Wu, and Saifeng Hu. Approximate sparsity and nonlocal total variation based compressive mr image reconstruction. *Mathematical Problems in Engineering*, 2014, 2014.
- [27] Anagha Deshmane, Vikas Gulani, Mark A Griswold, and Nicole Seiberlich. Parallel mr imaging. *Journal of Magnetic Resonance Imaging*, 36(1):55–72, 2012.
- [28] W Thomas Dixon. Simple proton spectroscopic imaging. *Radiology*, 153(1):189–194, 1984.
- [29] Mariya Doneva, Peter Börnert, Holger Eggers, Christian Stehning, Julien S enegas, and Alfred Mertins. Compressed sensing reconstruction for magnetic resonance parameter mapping. *Magnetic Resonance in Medicine*, 64(4):1114–1120, 2010.
- [30] Mariya Doneva, J S enegas, P B ornert, Holger Eggers, and Alfred Mertins. Accelerated mr parameter mapping using compressed sensing with model-based sparsifying transform. In *Proceedings of the International Society for Magnetic Resonance in Medicine*, volume 17, page 2812, 2009.
- [31] Jens M Edmund and Tufve Nyholm. A review of substitute ct generation for mri-only radiation therapy. *Radiation Oncology*, 12(1):1–15, 2017.
- [32] Matthias J Ehrhardt and Marta M Betcke. Multicontrast mri reconstruction with structure-guided total variation. *SIAM Journal on Imaging Sciences*, 9(3):1084–1106, 2016.

- [33] Matthias J Ehrhardt, Kris Thielemans, Luis Pizarro, David Atkinson, Sébastien Ourselin, Brian F Hutton, and Simon R Arridge. Joint reconstruction of pet-mri by exploiting structural similarity. *Inverse Problems*, 31(1):015001, 2014.
- [34] Sarah Elliott, Alexandra Berlangieri, Jason Wasiak, Michael Chao, and Farshad Foroudi. Use of magnetic resonance imaging-guided radiotherapy for breast cancer: a scoping review protocol. *Systematic reviews*, 10(1):1–7, 2021.
- [35] Pedro M Enriquez-Navas, Yoonseok Kam, Tuhin Das, Sabrina Hassan, Ariosto Silva, Parastou Foroutan, Epifanio Ruiz, Gary Martinez, Susan Minton, Robert J Gillies, et al. Exploiting evolutionary principles to prolong tumor control in preclinical models of breast cancer. *Science translational medicine*, 8(327):327ra24–327ra24, 2016.
- [36] CJ Galbán, BA Hoff, TL Chenevert, and BD Ross. Diffusion mri in early cancer therapeutic response assessment. *NMR in biomedicine*, 30(3):e3458, 2017.
- [37] Robert Gatenby and Joel Brown. The evolution and ecology of resistance in cancer therapy. *Cold Spring Harbor perspectives in medicine*, 8(3):a033415, 2018.
- [38] Robert A Gatenby, Olya Grove, and Robert J Gillies. Quantitative imaging in cancer evolution and ecology. *Radiology*, 269(1):8, 2013.
- [39] Yaorong Ge and Q Jackie Wu. Knowledge-based planning for intensity-modulated radiation therapy: a review of data-driven approaches. *Medical physics*, 46(6):2760–2775, 2019.
- [40] Gary H Glover. Multipoint dixon technique for water and fat proton and susceptibility imaging. *Journal of Magnetic Resonance Imaging*, 1(5):521–530, 1991.
- [41] Gary H Glover and Erika Schneider. Three-point dixon technique for true water/fat decomposition with b0 inhomogeneity correction. *Magnetic resonance in medicine*, 18(2):371–383, 1991.

- [42] JK Gohagan, EL Spitznagel, WA Murphy, MW Vannier, WT Dixon, DJ Gersell, SL Rossnick, WG Totty, JM Destouet, and DLetal Rickman. Multispectral analysis of mr images of the breast. *Radiology*, 163(3):703–707, 1987.
- [43] Ian Goodfellow, Jean Pouget-Abadie, Mehdi Mirza, Bing Xu, David Warde-Farley, Sherjil Ozair, Aaron Courville, and Yoshua Bengio. Generative adversarial nets. *Advances in neural information processing systems*, 27, 2014.
- [44] Mark A Griswold, Peter M Jakob, Robin M Heidemann, Mathias Nittka, Vladimir Jellus, Jianmin Wang, Berthold Kiefer, and Axel Haase. Generalized autocalibrating partially parallel acquisitions (grappa). *Magnetic Resonance in Medicine: An Official Journal of the International Society for Magnetic Resonance in Medicine*, 47(6):1202–1210, 2002.
- [45] Igor Griva, Stephen G Nash, and Ariela Sofer. *Linear and nonlinear optimization*, volume 108. Siam, 2009.
- [46] S Hawkins, Olya Stringfield, N Rognin, J Arrington, M Yu, H Enderling, S Sahebjam, and Natarjan Raghunand. Mri predictors of response to anti-pd1 immune checkpoint inhibition, bevacizumab and hypofractionated stereotactic irradiation in patients with recurrent high grade gliomas. 2018.
- [47] Charisma Hehakaya, Jochem R Van der Voort van Zyp, Jan JW Lagendijk, Diederick E Grobbee, Helena M Verkooijen, and Ellen HM Moors. Problems and promises of introducing the magnetic resonance imaging linear accelerator into routine care: The case of prostate cancer. *Frontiers in oncology*, 10:1741, 2020.

- [48] Eline D Hessen, Laurens D van Buuren, Jasper A Nijkamp, Kim C de Vries, Wai Kong Mok, Luc Dewit, Anke M van Mourik, Alejandro Berlin, Uulke A van der Heide, and Gerben R Borst. Significant tumor shift in patients treated with stereotactic radiosurgery for brain metastasis. *Clinical and translational radiation oncology*, 2:23–28, 2017.
- [49] Geoffrey Hinton. Why equivariance is better than premature invariance, 2021.
- [50] Chuan Huang, Christian G Graff, Eric W Clarkson, Ali Bilgin, and Maria I Altbach. T2 mapping from highly undersampled data by reconstruction of principal component coefficient maps using compressed sensing. *Magnetic resonance in medicine*, 67(5):1355–1366, 2012.
- [51] Junzhou Huang, Chen Chen, and Leon Axel. Fast multi-contrast mri reconstruction. In *International Conference on Medical Image Computing and Computer-Assisted Intervention*, pages 281–288. Springer, 2012.
- [52] Junzhou Huang, Chen Chen, and Leon Axel. Fast multi-contrast mri reconstruction. *Magnetic resonance imaging*, 32(10):1344–1352, 2014.
- [53] Margerie Huet Dastarac. Dose prediction for protontherapy using neural networks, June 2019.
- [54] Phillip Isola, Jun-Yan Zhu, Tinghui Zhou, and Alexei A Efros. Image-to-image translation with conditional adversarial networks. In *Proceedings of the IEEE conference on computer vision and pattern recognition*, pages 1125–1134, 2017.
- [55] Bruna V Jardim-Perassi, Suning Huang, William Dominguez-Viqueira, Jan Poleszczuk, Mikalai M Budzevich, Mahmoud A Abdalah, Smitha R Pillai, Epifanio Ruiz, Marilyn M Bui, Debora APC Zuccari, et al. Multiparametric mri and coregistered histology identify tumor habitats in breast cancer mouse modelsimaging habitats using multiparametric mri. *Cancer research*, 79(15):3952–3964, 2019.

- [56] Rama Jayasundar, Laurance D Hall, and Norman M Bleehen. The effects of anesthesia and physical restraint on intra-and extracellular tumor ph, tumor temperature and bioenergetics in murine rif-1 tumors. *Magnetic resonance imaging*, 15(7):847–855, 1997.
- [57] Bodo Kaiser and Shadi Albarqouni. Mri to ct translation with gans. *arXiv preprint arXiv:1901.05259*, 2019.
- [58] Robin Kates, Dennis Atkinson, and Michael Brant-Zawadzki. Fluid-attenuated inversion recovery (flair): clinical prospectus of current and future applications. *Topics in magnetic resonance imaging: TMRI*, 8(6):389–396, 1996.
- [59] Paul J Keall, Caterina Brighi, Carri Glide-Hurst, Gary Liney, Paul ZY Liu, Suzanne Lydiard, Chiara Paganelli, Trang Pham, Shanshan Shan, Alison C Tree, et al. Integrated mri-guided radiotherapy—opportunities and challenges. *Nature Reviews Clinical Oncology*, pages 1–13, 2022.
- [60] Ki Hwan Kim, Won-Joon Do, and Sung-Hong Park. Improving resolution of mr images with an adversarial network incorporating images with different contrast. *Medical physics*, 45(7):3120–3131, 2018.
- [61] Diederik P Kingma and Jimmy Ba. Adam: A method for stochastic optimization. *arXiv preprint arXiv:1412.6980*, 2014.
- [62] Florian Knoll, Kristian Bredies, Thomas Pock, and Rudolf Stollberger. Second order total generalized variation (tgv) for mri. *Magnetic resonance in medicine*, 65(2):480–491, 2011.
- [63] Ernst S Kooreman, Petra J van Houdt, Rick Keesman, Floris J Pos, Vivian WJ van Pelt, Marlies E Nowee, Andreas Wetscherek, Rob HN Tijssen, Marielle EP Philippens, Daniela Thorwarth, et al. Adc measurements on the unity mr-linac—a recommendation on behalf of the elekta unity mr-linac consortium. *Radiotherapy and Oncology*, 153:106–113, 2020.

- [64] Ernst S Kooreman, Petra J van Houdt, Marlies E Nowee, Vivian WJ van Pelt, Rob HN Tijssen, Eric S Paulson, Oliver J Gurney-Champion, Jihong Wang, Folkert Koetsveld, Laurens D van Buuren, et al. Feasibility and accuracy of quantitative imaging on a 1.5 t mr-linear accelerator. *Radiotherapy and Oncology*, 133:156–162, 2019.
- [65] Patrick Kupelian and Jan-Jakob Sonke. Magnetic resonance-guided adaptive radiotherapy: a solution to the future. In *Seminars in radiation oncology*, volume 24, pages 227–232. Elsevier, 2014.
- [66] T Kutuk, S Pandey, MN Mills, M Abdalah, O Stringfield, K Latifi, TJ Robinson, KA Ahmed, and N Raghunand. Utilizing radiation dose maps to predict local failure following stereotactic radiation of brain metastases. *International Journal of Radiation Oncology, Biology, Physics*, 111(3):e570–e571, 2021.
- [67] Tugce Kutuk, Shraddha Pandey, MN Mills, Mahmoud Abdalah, Olya Stringfield, K Latifi, TJ Robinson, Kamran Ahmed, and Natarjan Raghunand. Utilizing radiation dose maps to predict local failure following stereotactic radiation of brain metastases. 2021.
- [68] Chandana Lall, Vlad Bura, Thomas K Lee, Priya Bhosale, Silvana C Faria, Joon-II Choi, and Zhen Jane Wang. Diffusion-weighted imaging in hemorrhagic abdominal and pelvic lesions: restricted diffusion can mimic malignancy. *Abdominal Radiology*, 43(7):1772–1784, 2018.
- [69] Germana Landi, Elena Loli Piccolomini, and Fabiana Zama. A total variation-based reconstruction method for dynamic mri. *Computational and Mathematical Methods in Medicine*, 9(1):69–80, 2008.

- [70] Terry H Landowski, Gerald P Guntle, Dezheng Zhao, Bhumasamudram Jagadish, Eugene A Mash, Robert T Dorr, and Natarajan Raghunand. Magnetic resonance imaging identifies differential response to pro-oxidant chemotherapy in a xenograft model. *Translational Oncology*, 9(3):228–235, 2016.
- [71] E Le Rhun, F Dhermain, G Vogin, N Reyns, and P Metellus. Radionecrosis after stereotactic radiotherapy for brain metastases. *Expert review of neurotherapeutics*, 16(8):903–914, 2016.
- [72] Hoyeon Lee, Hojin Kim, Jungwon Kwak, Young Seok Kim, Sang Wook Lee, Seungryong Cho, and Byungchul Cho. Fluence-map generation for prostate intensity-modulated radiotherapy planning using a deep-neural-network. *Scientific reports*, 9(1):1–11, 2019.
- [73] B Lemasson, N Pannetier, N Coquery, Ligia SB Boisserand, Nora Collomb, N Schuff, M Moseley, G Zaharchuk, EL Barbier, and T Christen. Mr vascular fingerprinting in stroke and brain tumors models. *Scientific reports*, 6(1):1–11, 2016.
- [74] Michael L Lipton. *Totally accessible MRI: a user’s guide to principles, technology, and applications*. Springer Science & Business Media, 2010.
- [75] Shujun Liu, Jianxin Cao, Hongqing Liu, Xiaodong Shen, Kui Zhang, and Pin Wang. Mri reconstruction using a joint constraint in patch-based total variational framework. *Journal of Visual Communication and Image Representation*, 46:150–164, 2017.
- [76] Zhiqiang Liu, Jiawei Fan, Minghui Li, Hui Yan, Zhihui Hu, Peng Huang, Yuan Tian, Junjie Miao, and Jianrong Dai. A deep learning method for prediction of three-dimensional dose distribution of helical tomotherapy. *Medical physics*, 46(5):1972–1983, 2019.

- [77] Victoria M Lukasik and Robert J Gillies. Animal anaesthesia for in vivo magnetic resonance. *NMR in Biomedicine: An International Journal Devoted to the Development and Application of Magnetic Resonance In Vivo*, 16(8):459–467, 2003.
- [78] Michael Lustig, David Donoho, and John M Pauly. Sparse mri: The application of compressed sensing for rapid mr imaging. *Magnetic Resonance in Medicine: An Official Journal of the International Society for Magnetic Resonance in Medicine*, 58(6):1182–1195, 2007.
- [79] Ming Ma, Nataliya Kovalchuk, Mark K Buyyounouski, Lei Xing, and Yong Yang. Incorporating dosimetric features into the prediction of 3d vmat dose distributions using deep convolutional neural network. *Physics in Medicine & Biology*, 64(12):125017, 2019.
- [80] Bruno Madore. Using unfold to remove artifacts in parallel imaging and in partial-fourier imaging. *Magnetic Resonance in Medicine: An Official Journal of the International Society for Magnetic Resonance in Medicine*, 48(3):493–501, 2002.
- [81] Sagar Mandava, Mahesh B Keerthivasan, Zhitao Li, Diego R Martin, Maria I Altbach, and Ali Bilgin. Accelerated mr parameter mapping with a union of local subspaces constraint. *Magnetic Resonance in Medicine*, 80(6):2744–2758, 2018.
- [82] David A Mankoff, Michael D Farwell, Amy S Clark, and Daniel A Pryma. Making molecular imaging a clinical tool for precision oncology: a review. *JAMA oncology*, 3(5):695–701, 2017.
- [83] Paul MJ McSheehy, Claudia Weidensteiner, Catherine Cannet, Stephane Ferretti, Didier Laurent, Stephan Ruetz, Michael Stumm, and Peter R Allegrini. Quantified tumor t1 is a generic early-response imaging biomarker for chemotherapy reflecting cell viability. *Clinical Cancer Research*, 16(1):212–225, 2010.

- [84] Thierry Meerbothe. A physics guided neural network approach for dose prediction in automated radiation therapy treatment planning. 2021.
- [85] Matthew N Mills, Chetna Thawani, Nicholas B Figura, Daniel E Oliver, Aixa E Soyano, Arnold Etame, Timothy J Robinson, James K Liu, Michael A Vogelbaum, Peter A Forsyth, et al. Breast cancer subtype predicts clinical outcomes after stereotactic radiation for brain metastases. *Journal of Neuro-Oncology*, 152(3):591–601, 2021.
- [86] Mehdi Mirza and Simon Osindero. Conditional generative adversarial nets. *arXiv preprint arXiv:1411.1784*, 2014.
- [87] Monireh Mohebbi Moghadam, Bahar Boroomand, Mohammad Jalali, Arman Zareian, Alireza DaeiJavad, and Mohammad Hossein Manshaei. Game of gans: Game theoretical models for generative adversarial networks. *arXiv preprint arXiv:2106.06976*, 2021.
- [88] Shadab Momin, Yabo Fu, Yang Lei, Justin Roper, Jeffrey D Bradley, Walter J Curran, Tian Liu, and Xiaofeng Yang. Knowledge-based radiation treatment planning: A data-driven method survey. *Journal of Applied Clinical Medical Physics*, 22(8):16–44, 2021.
- [89] Mikael Montelius, Oscar Jalnefjord, Johan Spetz, Ola Nilsson, Eva Forssell-Aronsson, and Maria Ljungberg. Multiparametric mr for non-invasive evaluation of tumour tissue histological characteristics after radionuclide therapy. *NMR in Biomedicine*, 32(3):e4060, 2019.
- [90] Dan Nguyen, Xun Jia, David Sher, Mu-Han Lin, Zohaib Iqbal, Hui Liu, and Steve Jiang. 3d radiotherapy dose prediction on head and neck cancer patients with a hierarchically densely connected u-net deep learning architecture. *Physics in medicine & Biology*, 64(6):065020, 2019.

- [91] Dan Nguyen, Troy Long, Xun Jia, Weiguo Lu, Xuejun Gu, Zohaib Iqbal, and Steve Jiang. A feasibility study for predicting optimal radiation therapy dose distributions of prostate cancer patients from patient anatomy using deep learning. *Scientific reports*, 9(1):1–10, 2019.
- [92] Camille E Noel, Parag J Parikh, Christopher R Spencer, Olga L Green, Yanle Hu, Sasa Mucic, and Jeffrey R Olsen. Comparison of onboard low-field magnetic resonance imaging versus onboard computed tomography for anatomy visualization in radiotherapy. *Acta oncologica*, 54(9):1474–1482, 2015.
- [93] Shraddha Pandey, Tugce Kutuk, MN Mills, Mahmoud Abdalah, Olya Stringfield, K Latifi, TJ Robinson, Moreno Wilfrido, Kamran Ahmed, and Natarjan Raghunand. Predicting post-stereotactic radiotherapy magnetic resonance image outcomes of breast cancer metastases to the brain. 2022.
- [94] Shraddha Pandey, Tugce Kutuk, MN Mills, Mahmoud Abdalah, Olya Stringfield, K Latifi, TJ Robinson, Moreno Wilfrido, Kamran Ahmed, and Natarjan Raghunand. Predicting stereotactic radiosurgery dose maps from pre-therapy mr images using a deep neural network. 2022.
- [95] Shraddha Pandey, A David Snider, Wilfrido A Moreno, Harshan Ravi, Ali Bilgin, and Natarajan Raghunand. Joint total variation-based reconstruction of multiparametric magnetic resonance images for mapping tissue types. *NMR in Biomedicine*, 34(12):e4597, 2021.
- [96] Xi Peng, Xin Liu, Hairong Zheng, and Dong Liang. Exploiting parameter sparsity in model-based reconstruction to accelerate proton density and t2 mapping. *Medical Engineering & Physics*, 36(11):1428–1435, 2014.

- [97] Klaas P Pruessmann, Markus Weiger, Markus B Scheidegger, and Peter Boesiger. Sense: sensitivity encoding for fast mri. *Magnetic Resonance in Medicine: An Official Journal of the International Society for Magnetic Resonance in Medicine*, 42(5):952–962, 1999.
- [98] Natarajan Raghunand and Robert A Gatenby. Bridging spatial scales from radiographic images to cellular and molecular properties in cancers. In *Molecular Imaging*, pages 1675–1690. Elsevier, 2021.
- [99] Scott B Reeder, Zhifei Wen, Huanzhou Yu, Angel R Pineda, Garry E Gold, Michael Markl, and Norbert J Pelc. Multicoil dixon chemical species separation with an iterative least-squares estimation method. *Magnetic Resonance in Medicine: An Official Journal of the International Society for Magnetic Resonance in Medicine*, 51(1):35–45, 2004.
- [100] Olaf Ronneberger, Philipp Fischer, and Thomas Brox. U-net: Convolutional networks for biomedical image segmentation. In *International Conference on Medical image computing and computer-assisted intervention*, pages 234–241. Springer, 2015.
- [101] Leonid I Rudin, Stanley Osher, and Emad Fatemi. Nonlinear total variation based noise removal algorithms. *Physica D: nonlinear phenomena*, 60(1-4):259–268, 1992.
- [102] Anmol Sharma and Ghassan Hamarneh. Missing mri pulse sequence synthesis using multi-modal generative adversarial network. *IEEE transactions on medical imaging*, 39(4):1170–1183, 2019.
- [103] Nathan C Sheets, Gregg H Goldin, Anne-Marie Meyer, Yang Wu, YunKyung Chang, Til Stürmer, Jordan A Holmes, Bryce B Reeve, Paul A Godley, William R Carpenter, et al. Intensity-modulated radiation therapy, proton therapy, or conformal radiation therapy and morbidity and disease control in localized prostate cancer. *Jama*, 307(15):1611–1620, 2012.

- [104] Jonathan Richard Shewchuk et al. An introduction to the conjugate gradient method without the agonizing pain, 1994.
- [105] Satomi Shiraishi and Kevin L Moore. Knowledge-based prediction of three-dimensional dose distributions for external beam radiotherapy. *Medical physics*, 43(1):378–387, 2016.
- [106] Preethi Srinivasan, Prabhjot Kaur, Aditya Nigam, and Arnav Bhavsar. Semantic features aided multi-scale reconstruction of inter-modality magnetic resonance images. In *2020 IEEE 33rd International Symposium on Computer-Based Medical Systems (CBMS)*, pages 110–113. IEEE, 2020.
- [107] Luisa S Stark, Nicolaus Andratschke, Michael Baumgartl, Marta Bogowicz, Madalyne Chamberlain, Riccardo Dal Bello, Stefanie Ehrbar, Zaira Girbau Garcia, Matthias Guckenberger, Jérôme Krayenbühl, et al. Dosimetric and geometric end-to-end accuracy of a magnetic resonance guided linear accelerator. *Physics and imaging in radiation oncology*, 16:109–112, 2020.
- [108] Olya Stringfield, John A Arrington, Sandra K Johnston, Nicolas G Rognin, Noah C Peeri, Yoganand Balagurunathan, Pamela R Jackson, Kamala R Clark-Swanson, Kristin R Swanson, Kathleen M Egan, et al. Multiparameter mri predictors of long-term survival in glioblastoma multiforme. *Tomography*, 5(1):135–144, 2019.
- [109] Kristin R Swanson, Russell C Rockne, Jonathan Claridge, Mark A Chaplain, Ellsworth C Alvord, and Alexander RA Anderson. Quantifying the role of angiogenesis in malignant progression of gliomas: In silico modeling integrates imaging and histology malignant progression and kinetics of gliomas. *Cancer research*, 71(24):7366–7375, 2011.

- [110] Torfinn Taxt, Arvid Lundervold, Bjørn Fuglaas, Hans Lien, and Vera Abeler. Multi-spectral analysis of uterine corpus tumors in magnetic resonance imaging. *Magnetic resonance in medicine*, 23(1):55–76, 1992.
- [111] Daniela Thorwarth and Daniel A Low. Technical challenges of real-time adaptive mr-guided radiotherapy. *Frontiers in Oncology*, 11:634507, 2021.
- [112] Michal R Tomaszewski, William Dominguez-Viqueira, Antonio Ortiz, Yu Shi, James R Costello, Heiko Enderling, Stephen A Rosenberg, and Robert J Gillies. Heterogeneity analysis of mri t2 maps for measurement of early tumor response to radiotherapy. *NMR in Biomedicine*, 34(3):e4454, 2021.
- [113] Jeffrey Tsao, Peter Boesiger, and Klaas P Pruessmann. k-t blast and k-t sense: dynamic mri with high frame rate exploiting spatiotemporal correlations. *Magnetic Resonance in Medicine: An Official Journal of the International Society for Magnetic Resonance in Medicine*, 50(5):1031–1042, 2003.
- [114] Alyssa Vanginderdeuren, John Aldo Lee, and Ana Maria Barragan Montero. Deep learning to predict optimized dose and its uncertainty for radiation oncology treatment planning.
- [115] Michael W Vannier, Robert L Butterfield, Douglas Jordan, William A Murphy, Robert G Levitt, and Mokhtar Gado. Multispectral analysis of magnetic resonance images. *Radiology*, 154(1):221–224, 1985.
- [116] Michael W Vannier, Robert L Butterfield, Douglas L Rickman, Douglas M Jordan, William A Murphy, and Pietro R Biondetti. Multispectral magnetic resonance image analysis. *Critical reviews in biomedical engineering*, 15(2):117–144, 1987.

- [117] Amy Walker, Gary Liney, Lois Holloway, Jason Dowling, David Rivest-Henault, and Peter Metcalfe. Continuous table acquisition mri for radiotherapy treatment planning: distortion assessment with a new extended 3d volumetric phantom. *Medical physics*, 42(4):1982–1991, 2015.
- [118] Wentao Wang, Yang Sheng, Chunhao Wang, Jiahao Zhang, Xinyi Li, Manisha Palta, Brian Czito, Christopher G Willett, Qiuwen Wu, Yaorong Ge, et al. Fluence map prediction using deep learning models—direct plan generation for pancreas stereotactic body radiation therapy. *Frontiers in artificial intelligence*, 3:68, 2020.
- [119] Yang Wang. A mathematical introduction to generative adversarial nets (gan). *arXiv preprint arXiv:2009.00169*, 2020.
- [120] Claudia Weidensteiner, Peter R Allegrini, Melanie Sticker-Jantscheff, Vincent Romanet, Stephane Ferretti, Paul MJ McSheehy, et al. Tumour t {sub 1} changes in vivo are highly predictive of response to chemotherapy and reflect the number of viable tumour cells—a preclinical mr study in mice. *BMC cancer (Online)*, 14, 2014.
- [121] Lior Weizman, JF De Castro Mota, Pingfan Song, Yonina C Eldar, and Miguel RD Rodrigues. Joint multicontrast mri reconstruction. *Signal Processing with Adaptive Sparse Structured Representations (SPARS ...)*, 2017.
- [122] Lei Xiang, Yong Chen, Weitang Chang, Yiqiang Zhan, Weili Lin, Qian Wang, and Dinggang Shen. Deep-learning-based multi-modal fusion for fast mr reconstruction. *IEEE Transactions on Biomedical Engineering*, 66(7):2105–2114, 2018.
- [123] Yunhai Xiao and Junfeng Yang. A fast algorithm for total variation image reconstruction from random projections. *arXiv preprint arXiv:1001.1774*, 2010.


- [124] Zheng Xu, Yeqing Li, Leon Axel, and Junzhou Huang. Efficient preconditioning in joint total variation regularized parallel mri reconstruction. In *International Conference on Medical Image Computing and Computer-Assisted Intervention*, pages 563–570. Springer, 2015.
- [125] Alice Chieh-Yu Yang, Madison Kretzler, Sonja Sudarski, Vikas Gulani, and Nicole Seiberlich. Sparse reconstruction techniques in mri: methods, applications, and challenges to clinical adoption. *Investigative radiology*, 51(6):349, 2016.
- [126] Thomas E Yankeelov, Kenneth J Niermann, Jessica Huamani, Dong W Kim, Christopher C Quarles, Arthur C Fleischer, Dennis E Hallahan, Ronald R Price, and John C Gore. Correlation between estimates of tumor perfusion from microbubble contrast-enhanced sonography and dynamic contrast-enhanced magnetic resonance imaging. *Journal of Ultrasound in Medicine*, 25(4):487–497, 2006.
- [127] Jiawen Yao, Zheng Xu, Xiaolei Huang, and Junzhou Huang. An efficient algorithm for dynamic mri using low-rank and total variation regularizations. *Medical image analysis*, 44:14–27, 2018.
- [128] Huanzhou Yu, Charles A McKenzie, Ann Shimakawa, Anthony T Vu, Anja CS Brau, Philip J Beatty, Angel R Pineda, Jean H Brittain, and Scott B Reeder. Multiecho reconstruction for simultaneous water-fat decomposition and t_2^* estimation. *Journal of Magnetic Resonance Imaging: An Official Journal of the International Society for Magnetic Resonance in Medicine*, 26(4):1153–1161, 2007.
- [129] Jing Yuan, Darren MC Poon, Gladys Lo, Oi Lei Wong, Kin Yin Cheung, and Siu Ki Yu. A narrative review of mri acquisition for mr-guided-radiotherapy in prostate cancer. *Quantitative Imaging in Medicine and Surgery*, 12(2):1585, 2022.

- [130] Bo Zhan, Jianghong Xiao, Chongyang Cao, Xingchen Peng, Chen Zu, Jiliu Zhou, and Yan Wang. Multi-constraint generative adversarial network for dose prediction in radiotherapy. *Medical Image Analysis*, 77:102339, 2022.
- [131] Jingsong Zhang, Jessica J Cunningham, Joel S Brown, and Robert A Gatenby. Integrating evolutionary dynamics into treatment of metastatic castrate-resistant prostate cancer. *Nature communications*, 8(1):1–9, 2017.
- [132] Bo Zhao, Fan Lam, and Zhi-Pei Liang. Model-based mr parameter mapping with sparsity constraints: parameter estimation and performance bounds. *IEEE transactions on medical imaging*, 33(9):1832–1844, 2014.
- [133] Bo Zhao, Wenmiao Lu, T Kevin Hitchens, Fan Lam, Chien Ho, and Zhi-Pei Liang. Accelerated mr parameter mapping with low-rank and sparsity constraints. *Magnetic resonance in medicine*, 74(2):489–498, 2015.
- [134] Konstantinos Zormpas-Petridis, Evon Poon, Matthew Clarke, Neil P Jerome, Jessica KR Boulton, Matthew D Blackledge, Fernando Carceller, Alexander Koers, Giuseppe Barone, Andrew DJ Pearson, et al. Noninvasive mri native t1 mapping detects response to mycn-targeted therapies in the th-mycn model of neuroblastoma. *Cancer Research*, 80(16):3424–3435, 2020.

Appendix A: Copyright Permission to Use Published Content in Chapter 3

WILEY

THE WILEY NETWORK | INSTRUCTORS & STUDENTS | JOURNAL EDITORS | LIBRARIANS | PROFESSIONALS | **RESEARCHERS** | SOCIETY LEADERS

TOPICS ▾ CONTENT TYPE ▾ 

The rights holder could be the author or the publisher of the content. The rights holder will be specified in the copyright line of a publication. You can also find rights holder information by searching through the [Copyright Clearance Center](#).

Reusing Wiley content

If you're reusing Wiley content in your thesis or dissertation, rights will be granted at no cost to you if the content meets these requirements:

- **Your thesis or dissertation is not being used for commercial purposes.** This means that you're submitting it only for graduation requirements. You don't currently have a deal with a commercial publisher, and you won't otherwise be benefitting financially from the publication of your thesis.
- **Wiley is the rights holder of the content you are seeking to reuse.** Usually, Wiley holds the rights to our content, but occasionally the rights holder will be an author or sponsoring organization. In those cases, Wiley cannot guarantee free reuse.

While Wiley does grant free reuse of content in thesis and dissertation projects, we do still require a record of use so that we can issue you a license agreement.

If you publish your thesis or dissertation through a commercial publisher in the future, you will need to reapply for commercial reuse licenses. The legal rights granted for content reuse in non-commercial publications, such as a thesis or dissertation, are different from the rights required by commercial publishers to legally republish third-party content.

Do I need to request permission to use my own work as my dissertation?


If you are the author of a published Wiley article, you have the right to reuse the full text of your published article as part of your thesis or dissertation. In this situation, you do not need to request permission from Wiley for this use.

If your institution still requires a reuse license in this case, follow the steps below to request your license via RightsLink.

Appendix B: Copyright Permission to Use Published Content in Chapter 6

CCC RightsLink

Home ? Help Email Support Sign in Create Account

 Utilizing Radiation Dose Maps to Predict Local Failure Following Stereotactic Radiation of Brain Metastases

Author: T. Kutuk.S. Pandey,M.N. Mills,M. Abdalah,O. Stringfield,K. Latif,T.J. Robinson,K.A. Ahmed,N. Raghunand
Publication: International Journal of Radiation Oncology*Biolog*Physics
Publisher: Elsevier
Date: 1 November 2021
Copyright © 2021, Elsevier

Journal Author Rights

Please note that, as the author of this Elsevier article, you retain the right to include it in a thesis or dissertation, provided it is not published commercially. Permission is not required, but please ensure that you reference the journal as the original source. For more information on this and on your other retained rights, please visit: <https://www.elsevier.com/about/our-business/policies/copyright#Author-rights>

BACK CLOSE WINDOW

Appendix C: Copyright Permission to Use DWI Figure in Chapter 2

License Details

This Agreement between University of South Florida -- Shraddha Pandey ("You") and Springer Nature ("Springer Nature") consists of your license details and the terms and conditions provided by Springer Nature and Copyright Clearance Center.

[Print](#) [Copy](#)

License Number	5420870054244
License date	Nov 02, 2022
Licensed Content Publisher	Springer Nature
Licensed Content Publication	Abdominal Radiology
Licensed Content Title	Diffusion-weighted imaging in hemorrhagic abdominal and pelvic lesions: restricted diffusion can mimic malignancy
Licensed Content Author	Chandana Lall et al
Licensed Content Date	Nov 6, 2017
Type of Use	Thesis/Dissertation
Requestor type	academic/university or research institute
Format	electronic
Portion	figures/tables/illustrations
Number of figures/tables/illustrations	1
Will you be translating?	no
Circulation/distribution	1 - 29
Author of this Springer Nature content	no
Title	Diffusion-weighted imaging in hemorrhagic abdominal and pelvic lesions: restricted diffusion can mimic malignancy
Institution name	University of South Florida
Expected presentation date	Nov 2022
Portions	Figure 2
Requestor Location	University of South Florida 704 East River Drive Tampa TAMPA, FL 33617 United States Attn: University of South Florida
Total	0.00 USD

Appendix D: Copyright Permission to Use Fatwater Figure in Chapter 2

QUESTIONS AND ANSWERS IN MRI	QUESTIONS AND ANSWERS IN MRI
	Home
	Complete List of Questions
	...Magnets & Scanners
	...Safety and Screening
	...The NMR Phenomenon
	...Pulse Sequences
	...Making an Image
	...K-space & Rapid Imaging
	...Contrast Agents & Blood
	...Cardiovascular and MRA
	...MR Artifacts
	...Functional Imaging
	...MR Spectroscopy
	...New/Advanced Topics
	Copyright/Legal
Forums/Blogs/Links	
What's New	
Self-test Quizzes - NEW!	

Copyright Issues

During 30 years of radiology practice I have collected numerous cases, drawings, and illustrations relating to MR imaging and MR physics. Although most of these are of my own creation, a number of images, photographs, and graphic materials have come from colleagues in academics and industry. A number of these externally derived elements have been incorporated into this web site, and I have given full credit to these sources and/or obtained permission for their use when possible.

Unfortunately, the provenances surrounding some of these graphic elements collected over three decades have been lost or forgotten. It is not my intent to misuse anyone's copyrighted work, and I fully respect artist and content owner's rights. I pledge to fully comply with the [Digital Millenium Copyright Act of 1998](#), investigating any alleged infringement notices by the owner and removing any verified item or link promptly. To make such a notice, please [click here](#) and provide details. Alternatively, I would sincerely appreciate your allowing continued use of these materials on the site if you simply tell me how they should be credited.

In addition to graphic elements, this web site also contains links and pdfs to a number of scientific papers of which the original authors and publishers may retain copyrights. Many of these works are already widely available on the internet from the authors' own web sites or institutional repositories. A substantial number of papers and images are distributed under open access and Creative Commons licenses. Some very old works are now in the public domain. Others I have personally purchased or received as reprint gifts from authors over the years. As you read these papers on my web site, consider yourself as a student guest sitting in my private library that I maintain for teaching purposes. I would ask all readers of this site not to copy, repost, or distribute these works lest they be taken down and not available for the higher good of science education.

This web site has been created as a public service to the greater scientific community. I receive no compensation or external support for this endeavor and have personally assumed all costs of producing and maintaining this site. So, if an item is discovered that has unintentionally infringed on someone else's work, I ask understanding and forgiveness and promise to quickly make things right.

On the flip side, all other images and text on this website are my own creation, so any commercial use of this material without my express written consent is prohibited. However, **if you wish to use a small number of my images (in a non-commercial setting, such as for lectures, graduate theses, etc), feel free to do so, crediting them "Courtesy of Allen D. Elster, MRIquestions.com"**.

Allen Elster

Appendix E: IRB Approval



RESEARCH INTEGRITY & COMPLIANCE
Institutional Review Boards: FWA No. 00001668
12961 Bruce B. Downs Blvd, MDC13, Tampa, FL 33612-4785
(813) 974-5638 FAX (813) 974-7071

government-collected information obtained for nonresearch activities, if the research generates identifiable private information that is or will be maintained on information technology that is subject to and in compliance with section 208(b) of the E-Government Act of 2002, 44 U.S.C. 3501 note, if all of the identifiable private information collected, used, or generated as part of the activity will be maintained in systems of records subject to the Privacy Act of 1974, 5 U.S.C. 552a, and, if applicable, the information used in the research was collected subject to the Paperwork Reduction Act of 1995, 44 U.S.C. 3501 et seq.

8/1/2019

Roberto Diaz, M.D.
H Lee Moffitt Cancer Center
12902 USF Magnolia Drive, MCC-Rad Onc
H. Lee Moffitt Cancer Center & Research Institute
Tampa, FL 33612

RE: Expedited Study Determined Exempt at Continuing Review
IRB#: CR4_Pro0023399

Title: Treatment outcomes of breast cancer patients treated with all or one of the multimodality therapies at H. Lee Moffitt Cancer Center & Research Institute

Study Approval Period: 8/1/2019

Dear Dr. Diaz:

On 8/1/2019 3:16 PM, the Institutional Review Board (IRB) reviewed and **APPROVED** the above application and all documents contained within including those outlined below. Please note that this protocol is now approved under the 2018 Common Rule (45 CFR 46) and is now **exempt**. Thus, **Continuing Review is no longer required** and your application will be closed per USF HRPP policy.

The IRB determined that your study qualified for exempt review based on criteria for exemption in the federal regulations as outlined by 45 CFR 46.104(d):

(4) Secondary research for which consent is not required: Secondary research uses of identifiable private information or identifiable biospecimens, if at least one of the following criteria is met: (i) The identifiable private information or identifiable biospecimens are publicly available; (ii) Information, which may include information about biospecimens, is recorded by the investigator in such a manner that the identity of the human subjects cannot readily be ascertained directly or through identifiers linked to the subjects; the investigator does not contact the subjects, and the investigator will not re-identify subjects; (iii) The research involves only information collection and analysis involving the investigator's use of identifiable health information when that use is regulated under 45 CFR parts 160 and 164, subparts A and E, for the purposes of "health care operations" or "research" as those terms are defined at 45 CFR 164.501 or for "public health activities and purposes" as described under 45 CFR 164.512(b); or (iv) The research is conducted by, or on behalf of, a Federal department or agency using government-generated or


The previously issued waiver of HIPAA Authorization remains valid. Going forward, the date range in your waiver may be extended and the number of records reviewed may be increased without submitting a new IRB application, so long as your protocol is revised accordingly and complies with the minimum necessary requirement set forth in the Privacy Rule. Other minor changes, such as addition of a data variable, can also be made without resubmission. As per USF HRPP policy, changes to study design (e.g. changes in inclusion/exclusion criteria, change from retrospective to prospective data collection, changes in study sites, etc.) require a new IRB application. Please keep all protocol versions used throughout the life of the study.

As the principal investigator for this study, it is your responsibility to ensure that this research is conducted as outlined in your application and consistent with the ethical principles outlined in the Belmont Report and with USF HRPP policies and procedures.

Please note, as per USF HRPP policy, once the exempt determination is made, the application is closed in ARC. This does not limit your ability to conduct the research. Any proposed or anticipated change to the study design that was previously declared exempt from IRB oversight must be submitted to the IRB as a new study prior to initiation of the change. However, administrative changes, including changes in research personnel, do not warrant an Amendment or new application.

We appreciate your dedication to the ethical conduct of human subjects research at the University of South Florida and your continued commitment to human research protections. If you have any questions regarding this matter, please call 813-974-5638.

Sincerely,


E. Verena Jorgensen, M.D., Chairperson
USF Institutional Review Board

Appendix F: IACUC Approval



MEMORANDUM

TO: Natarajan Raghunand,
[Redacted]

FROM: Farah Moulvi, MSPH, IACUC Coordinator
Institutional Animal Care & Use Committee
Research Integrity & Compliance

DATE: 11/5/2015

PROJECT TITLE: Imaging Biomarkers of Oxidative Stress and Inflammation

FUNDING SOURCE: H. Lee Moffitt Cancer Center

IACUC PROTOCOL #: R IS00001613

PROTOCOL STATUS: APPROVED

review.

• All modifications to the IACUC-Approved Protocol must be approved by the IACUC prior to initiating the modification. Modifications can be submitted to the IACUC for review and approval as an Amendment or Procedural Change through the eIACUC system. These changes must be within the scope of the original research hypothesis, involve the original species and justified in writing. Any change in the IACUC-approved protocol that does not meet the latter definition is considered a major protocol change and requires the submission of a new application.

• All costs invoiced to a grant account must be allocable to the purpose of the grant. Costs allocable to one protocol may not be shifted to another in order to meet deficiencies caused by overruns, or for other reasons convenience. Rotation of charges among protocols by month without establishing that the rotation schedule credibly reflects the relative benefit to each protocol is unacceptable.

RESEARCH & INNOVATION • RESEARCH INTEGRITY AND COMPLIANCE
INSTITUTIONAL ANIMAL CARE AND USE COMMITTEE
PHS No. A4102-01; AAALAC No. 000434; USDA No. 158-ROD15
University of South Florida • 12901 Bruce B. Downs Blvd., MDC35 • Tampa, FL 33612-4799
(813) 974-7106 • FAX (813) 974-7091

The Institutional Animal Care and Use Committee (IACUC) reviewed your application requesting the use of animals in research for the above-entitled study. The IACUC APPROVED your request to use the following animals in your protocol for a one-year period beginning 11/5/2015:

Mouse: C57BL/6J (6-8wks/15-20gms/M-F)	630
Mouse: 129S4/SvJaeJ (6-8wks/15-20gm/M-F)	400
Mouse: SCID or nude (6-8wks/15-20gms/M-F)	760
Mouse: TRAMP (6-8wks/15-20gm/M)	170
Mouse: Kras ^L SL G12D/+; p53 ^{R172H} +/+; Pdx ^{Cre} tg/+ (KPS) (6-8wks/15-20gms/M-F)	170

Please take note of the following:

• IACUC approval is granted for a one-year period at the end of which, an annual renewal form must be submitted for years two (2) and three (3) of the protocol through the eIACUC system. After three years all continuing studies must be completely re-described in a new electronic application and submitted to IACUC for

Appendix G: Generator Model

Model: "Generator Model"

Layer (type)	Output Shape	Param #	Connected to
input_3 (InputLayer)	[(None, 256, 256, 6)]	0	[]
conv2d_6 (Conv2D)	(None, 128, 128, 64)	6208	['input_3[0][0]']
leaky_re_lu_5 (LeakyReLU)	(None, 128, 128, 64)	0	['conv2d_6[0][0]']
conv2d_7 (Conv2D)	(None, 64, 64, 128)	131200	['leaky_re_lu_5[0][0]']
batch_normalization_4 (Batch Normalization)	(None, 64, 64, 128)	512	['conv2d_7[0][0]']
leaky_re_lu_6 (LeakyReLU)	(None, 64, 64, 128)	0	['batch_normalization_4[0][0]']
conv2d_8 (Conv2D)	(None, 32, 32, 256)	524544	['leaky_re_lu_6[0][0]']
batch_normalization_5 (Batch Normalization)	(None, 32, 32, 256)	1024	['conv2d_8[0][0]']
leaky_re_lu_7 (LeakyReLU)	(None, 32, 32, 256)	0	['batch_normalization_5[0][0]']
conv2d_9 (Conv2D)	(None, 16, 16, 512)	2097664	['leaky_re_lu_7[0][0]']
batch_normalization_6 (Batch Normalization)	(None, 16, 16, 512)	2048	['conv2d_9[0][0]']
leaky_re_lu_8 (LeakyReLU)	(None, 16, 16, 512)	0	['batch_normalization_6[0][0]']
conv2d_10 (Conv2D)	(None, 8, 8, 512)	4194816	['leaky_re_lu_8[0][0]']
batch_normalization_7 (Batch Normalization)	(None, 8, 8, 512)	2048	['conv2d_10[0][0]']
leaky_re_lu_9 (LeakyReLU)	(None, 8, 8, 512)	0	['batch_normalization_7[0][0]']
conv2d_11 (Conv2D)	(None, 4, 4, 512)	4194816	['leaky_re_lu_9[0][0]']
batch_normalization_8 (Batch Normalization)	(None, 4, 4, 512)	2048	['conv2d_11[0][0]']
leaky_re_lu_10 (LeakyReLU)	(None, 4, 4, 512)	0	['batch_normalization_8[0][0]']
conv2d_12 (Conv2D)	(None, 2, 2, 512)	4194816	['leaky_re_lu_10[0][0]']
batch_normalization_9 (Batch Normalization)	(None, 2, 2, 512)	2048	['conv2d_12[0][0]']

leaky_re_lu_11 (LeakyReLU)	(None, 2, 2, 512)	0	['batch_normalization_9[0][0]']
conv2d_13 (Conv2D)	(None, 1, 1, 512)	4194816	['leaky_re_lu_11[0][0]']
activation_1 (Activation)	(None, 1, 1, 512)	0	['conv2d_13[0][0]']
conv2d_transpose (Conv2DTranspose)	(None, 2, 2, 512)	4194816	['activation_1[0][0]']
batch_normalization_10 (Batch Normalization)	(None, 2, 2, 512)	2048	['conv2d_transpose[0][0]']
dropout (Dropout)	(None, 2, 2, 512)	0	['batch_normalization_10[0][0]']
concatenate_1 (Concatenate)	(None, 2, 2, 1024)	0	['dropout[0][0]', 'leaky_re_lu_11[0][0]']
activation_2 (Activation)	(None, 2, 2, 1024)	0	['concatenate_1[0][0]']
conv2d_transpose_1 (Conv2DTranspose)	(None, 4, 4, 512)	8389120	['activation_2[0][0]']
batch_normalization_11 (Batch Normalization)	(None, 4, 4, 512)	2048	['conv2d_transpose_1[0][0]']
dropout_1 (Dropout)	(None, 4, 4, 512)	0	['batch_normalization_11[0][0]']
concatenate_2 (Concatenate)	(None, 4, 4, 1024)	0	['dropout_1[0][0]', 'leaky_re_lu_10[0][0]']
activation_3 (Activation)	(None, 4, 4, 1024)	0	['concatenate_2[0][0]']
conv2d_transpose_2 (Conv2DTranspose)	(None, 8, 8, 512)	8389120	['activation_3[0][0]']
batch_normalization_12 (Batch Normalization)	(None, 8, 8, 512)	2048	['conv2d_transpose_2[0][0]']
dropout_2 (Dropout)	(None, 8, 8, 512)	0	['batch_normalization_12[0][0]']
concatenate_3 (Concatenate)	(None, 8, 8, 1024)	0	['dropout_2[0][0]', 'leaky_re_lu_9[0][0]']
activation_4 (Activation)	(None, 8, 8, 1024)	0	['concatenate_3[0][0]']
conv2d_transpose_3 (Conv2DTranspose)	(None, 16, 16, 512)	8389120	['activation_4[0][0]']
batch_normalization_13 (Batch Normalization)	(None, 16, 16, 512)	2048	['conv2d_transpose_3[0][0]']

concatenate_4 (Concatenate)	(None, 16, 16, 1024 0)	0	['batch_normalization_13[0][0]', 'leaky_re_lu_8[0][0]']
activation_5 (Activation)	(None, 16, 16, 1024 0)	0	['concatenate_4[0][0]']
conv2d_transpose_4 (Conv2DTranspose)	(None, 32, 32, 256)	4194560	['activation_5[0][0]']
batch_normalization_14 (Batch Normalization)	(None, 32, 32, 256)	1024	['conv2d_transpose_4[0][0]']
concatenate_5 (Concatenate)	(None, 32, 32, 512)	0	['batch_normalization_14[0][0]', 'leaky_re_lu_7[0][0]']
activation_6 (Activation)	(None, 32, 32, 512)	0	['concatenate_5[0][0]']
conv2d_transpose_5 (Conv2DTranspose)	(None, 64, 64, 128)	1048704	['activation_6[0][0]']
batch_normalization_15 (Batch Normalization)	(None, 64, 64, 128)	512	['conv2d_transpose_5[0][0]']
concatenate_6 (Concatenate)	(None, 64, 64, 256)	0	['batch_normalization_15[0][0]', 'leaky_re_lu_6[0][0]']
activation_7 (Activation)	(None, 64, 64, 256)	0	['concatenate_6[0][0]']
conv2d_transpose_6 (Conv2DTranspose)	(None, 128, 128, 64)	262208	['activation_7[0][0]']
batch_normalization_16 (Batch Normalization)	(None, 128, 128, 64)	256	['conv2d_transpose_6[0][0]']
concatenate_7 (Concatenate)	(None, 128, 128, 128)	0	['batch_normalization_16[0][0]', 'leaky_re_lu_5[0][0]']
activation_8 (Activation)	(None, 128, 128, 128)	0	['concatenate_7[0][0]']
conv2d_transpose_7 (Conv2DTranspose)	(None, 256, 256, 1)	2049	['activation_8[0][0]']
activation_9 (Activation)	(None, 256, 256, 1)	0	['conv2d_transpose_7[0][0]']

=====
Total params: 54,428,289
Trainable params: 54,418,433
Non-trainable params: 9,856

Appendix H: Discriminator Model

Model: "Discriminator Model"

Layer (type)	Output Shape	Param #	Connected to
input_1 (InputLayer)	[(None, 256, 256, 6)]	0	[]
input_2 (InputLayer)	[(None, 256, 256, 1)]	0	[]
concatenate (Concatenate)	(None, 256, 256, 7)	0	['input_1[0][0]', 'input_2[0][0]']
conv2d (Conv2D)	(None, 128, 128, 64)	7232	['concatenate[0][0]']
leaky_re_lu (LeakyReLU)	(None, 128, 128, 64)	0	['conv2d[0][0]']
conv2d_1 (Conv2D)	(None, 64, 64, 128)	131200	['leaky_re_lu[0][0]']
batch_normalization (BatchNormalization)	(None, 64, 64, 128)	512	['conv2d_1[0][0]']
leaky_re_lu_1 (LeakyReLU)	(None, 64, 64, 128)	0	['batch_normalization[0][0]']
conv2d_2 (Conv2D)	(None, 32, 32, 256)	524544	['leaky_re_lu_1[0][0]']
batch_normalization_1 (BatchNormalization)	(None, 32, 32, 256)	1024	['conv2d_2[0][0]']
leaky_re_lu_2 (LeakyReLU)	(None, 32, 32, 256)	0	['batch_normalization_1[0][0]']
conv2d_3 (Conv2D)	(None, 16, 16, 512)	2097664	['leaky_re_lu_2[0][0]']
batch_normalization_2 (BatchNormalization)	(None, 16, 16, 512)	2048	['conv2d_3[0][0]']
leaky_re_lu_3 (LeakyReLU)	(None, 16, 16, 512)	0	['batch_normalization_2[0][0]']
conv2d_4 (Conv2D)	(None, 16, 16, 512)	4194816	['leaky_re_lu_3[0][0]']
batch_normalization_3 (BatchNormalization)	(None, 16, 16, 512)	2048	['conv2d_4[0][0]']
leaky_re_lu_4 (LeakyReLU)	(None, 16, 16, 512)	0	['batch_normalization_3[0][0]']
conv2d_5 (Conv2D)	(None, 16, 16, 1)	8193	['leaky_re_lu_4[0][0]']
activation (Activation)	(None, 16, 16, 1)	0	['conv2d_5[0][0]']

Total params: 6,969,281
Trainable params: 6,966,465
Non-trainable params: 2,816

|

About the Author

Shraddha Pandey received her Bachelors in Electrical Engineering degree from the South Gujarat University, Surat, India in 2006; her Masters of Technology in Electrical Engineering from the College of Engineering, Pune, India in 2009. She also worked in the domain of instrumentation, embedded system from 2009-2015. She became a Ph.D. student in the Electrical Engineering Department at the University of South Florida in 2016. Her doctoral research focused on developing algorithms to accelerate the reconstruction of multiparametric MRI. She has also carried out image analysis and have used deep neural network to predict MRI images. She also contributed to other areas of biomedical research by collaborating with multiple cross-functional teams and by mentoring students. Her research interests include MRI analysis, MRI prediction, biomedical signal processing and modelling, artificial intelligence, embedded systems, and innovation in engineering education.